Top Curr Chem (2014)
DOI: 10.1007/128_2014_618

Nonlinear Spectroscopy of Core and Valence Excitations Using Short X-Ray Pulses: Simulation Challenges

Yu Zhang, Weijie Hua, Kochise Bennett, and Shaul Mukamel

Abstract Measuring the nonlinear response of electrons and nuclei to attosecond broadband X-ray radiation has become possible by newly developed free electron lasers and high harmonic generation light sources. The design and interpretation of these novel experiments poses considerable computational challenges. In this chapter we survey the basic description of nonlinear X-ray spectroscopy signals and the electronic structure protocols which may be used for their simulation.

Keywords Core excitation · DFT · Double excitation · Double-quantum-coherence · MCSCF · Nonlinear spectroscopy · Real-time TDDFT · Stimulated X-ray Raman spectroscopy · TDDFT · X-ray

Contents

Y. Zhang, W. Hua, K. Bennett, and S. Mukamel (✉)
Department of Chemistry, University of California, Irvine, CA 92697, USA
e-mail: smukamel@uci.edu

Abbreviations

ADC	Algebraic diagrammatic construction
AES	Auger electron spectroscopy
AIMD	*ab initio* molecular dynamics
ASRS	Attosecond stimulated Raman spectroscopy
BO	Bohn–Oppenheimer
CAP	Complex absorption potential
CASPT2	Complete active space second-order perturbation theory
CASSCF	Complete active space self-consistent field
CASSI	Complete active space state interaction
CC	Coupled cluster
CCSD	Coupled cluster singles and doubles
CEO	Collective electronic oscillator
CFM	Crystal field multiplet
CI	Configuration interaction
CIS	Configuration interaction singles
CoIn	Conical intersection
CPP	Complex polarization propagator
CSF	Configuration state function
CV	Core-valence
CV-DFT	Constricted variational density functional theory
DCH	Double core hole
DFT	Density functional theory
DMRG	Density matrix renormalization group
DQC	Double-quantum-coherence
ECH	Equivalent core hole
EET	Excitation energy transfer
EOM	Equation of motion
ET	Electron transfer
EXAFS	Extended X-ray absorption fine structure
FC	Frank–Condon
FCH	Full core hole
FORS	Full optimization reaction space
GGA	Generalized gradient approximation
GSB	Ground state bleaching

HCH	Half core hole
HHG	High harmonic generation
IR	Infrared
LCM	Linear coupling model
LFT	Ligand field theory
MCSCF	Multiconfigurational self-consistent field
MLFT	Multiplet ligand field theory
MMUT	Modified midpoint unitary transform
MO	Molecular orbital
MOM	Maximum overlap method
MRCC	Multireference coupled cluster
MRCI	Multireference configuration interaction
MRPT	Multireference perturbation theory
NEO	Norm-extended optimization
NMA	*N*-methylacetamide
NR	Newton–Raphson
NTO	Natural transition orbital
OEP	Optimal effective potential
PAD	Photoelectron angular distribution
PES	Potential energy surface
RAS	Restricted active space
RASPT2	Restricted active space second-order perturbation theory
RASSCF	Restricted active space self-consistent field
RASSI	Restricted active space state interaction
REW	Restricted excitation window
RIXS	Resonant inelastic X-ray scattering
ROCIS	Restricted open-shell configuration interaction singles
ROHF	Restricted open-shell Hartree–Fock
RT	Real-time
SA	State-averaged
SAC-CI	Symmetry-adapted cluster configuration interaction
SCF	Self-consistent field
SF	Spin-flip
SIC	Self-interaction correction
SLE	Stochastic Liouville equation
SO	Spin-orbit
SOS	Sum over state
SS-MRCC	State-specific multireference coupled cluster
STEX	Static exchange
SXRS	Stimulated X-ray Raman spectroscopy
TDA	Tamm–Dancoff approximation
TDDFT	Time-dependent density functional theory
TDHF	Time-dependent Hartree–Fock
TDM	Transition dipole moments
TP	Transition potential
TRPES	Time-resolved photoelectron spectroscopy

TS	Transition state
TSH	Trajectory surface hopping
TXAS	Transient X-ray absorption spectroscopy
XANES	X-Ray absorption nearedge structure
XCH	Excited core hole
XDQC	X-Ray double-quantum-coherence
XES	X-Ray emission spectroscopy
XFEL	X-Ray free electron laser
XPS	X-Ray photoelectron spectroscopy

1 Introduction

In linear spectroscopy experiments, the incident light field interacts with the studied system only once and is relatively weak compared to the intrinsic interaction potential of the system. The signal can be considered as the linear response of the system to the perturbation of the light field. Linear spectroscopy provides useful information about the atomic and electronic structure of the system. Nonlinear spectroscopy techniques provide more detailed information. Nonlinear spectroscopy [1] employs multiple light fields to probe the correlations between different spectral features. Many controlling factors, such as the frequencies, wavevectors, and polarizations of the light fields and the time delays between them, can be varied so that detection of the correlation between certain spectroscopy features and their dynamics is possible.

Nonlinear optical spectroscopy became feasible soon after the invention of the laser in the 1960s. With the development of laser technology, pulse durations were reduced from picoseconds (1970s) to femtoseconds (1980s) [2], and now to attoseconds [3]. Nonlinear infrared and optical spectroscopy techniques have proved to be very successful for studying various excited state couplings and dynamics in molecules and materials [4, 5]. Nonlinear spectroscopy techniques in the X-ray regime made possible by new X-ray free electron lasers (XFEL) and high harmonic generation (HHG) sources provide a unique window into the motions of electrons, holes, and excitons in molecules and materials. Because of their broad bandwidth (about 10 eV for a 100-attosecond pulse), X-ray pulses can create coherent superpositions of many excited states localized at the target atoms. In analogy to how optical pulses manipulate molecular vibrations, attosecond X-ray pulses triggering and probing valence excited state dynamics have been considered recently [6] and explored experimentally [7–10]. Sequences of coherent broadband X-ray pulses can reveal the dynamics of nuclei and electrons in molecules with attosecond temporal, and nanometer spatial resolution.

X-Ray pulses can be used in various ways:

- Off-resonant diffraction detects the charge density. This technique can be extended to multiple dimensions to provide multipoint correlations of the charge density [11, 12].

- Core resonant spectroscopy offers a fast and versatile way to trigger valence excitations at selected positions and times via a stimulated Raman process [6] and to study their dynamics.
- Multiple cores can be excited at various delays, allowing the study of nonlinear response of valence electrons.

The complex nature of excited state correlations and dynamics leads to characteristic patterns in nonlinear spectroscopy signals, whose interpretation calls for state-of-the-art theoretical simulation methods. The simulation of time-domain nonlinear X-ray spectroscopy signals poses numerous challenges to quantum chemists. First, resonant X-ray spectroscopy involves core excited state. Most computational molecular electronic structure activity had focused on the ground state and valence excitations. Core excitations received much less attention because they do not participate in typical chemical processes. Core excited states lie well above many valence excited states, and calculating them directly with bottom-up algorithms is not practical. Core electrons also have special asymptotic behavior (cusp condition) close to the nuclei and large relativistic effects. Second, signals obtained by broadband X-ray pulses require many excited states. A state-by-state calculation scheme is tedious and it is better to obtain all excited states with an energy range in one shot. Third, resonant X-ray signals require not only the energies of excited states but also the transition dipoles between them. It is usually necessary to calculate high order excited state energy gradients to determine these quantities, which complicates the simulation. Furthermore, multiple X-ray pulses can easily create excited states with multiple core holes, which are not well described by single-reference-based excited state quantum chemistry methods such as adiabatic time-dependent density functional theory (TDDFT). Most of the discussions in this chapter are based on adiabatic TDDFT. Non-adiabatic frequency-dependent kernels are discussed in Sect. 4.3. Finally, many electrons may respond to the core hole created by the X-ray pulses (e.g., shake-up and shake-off processes) [13], so that many-body effects are very important in these signals. The single-particle picture may break down and high level methods such as multireference configuration interaction (MRCI) or multireference perturbation theory (MRPT) are often necessary to account for electron correlation. These challenges are addressed in the following sections. We focus on the theoretical methods (mainly DFT/TDDFT) which have been extensively used in X-ray spectroscopy simulation. There are excellent reviews on using TDDFT to simulate linear X-ray spectroscopy signals [13–15]. Here we emphasize the specific issues associated with nonlinear X-ray spectroscopy simulations and mainly discuss the methods applied to molecules.

This chapter is organized as follows. We first briefly describe the calculation of various nonlinear X-ray spectroscopy signals, and then review existing quantum chemistry simulation methods. We then discuss several key issues in nonlinear X-ray spectroscopy simulation. Finally, conclusions and future directions are outlined.

2 Nonlinear X-Ray Spectroscopies

A system of interacting electrons is described by the Hamiltonian

$$\hat{H} = \sum_i \frac{\hat{p}_i^2}{2m_i} + \frac{1}{2}\sum_{ij} \hat{\mathcal{V}}\left(\left|\mathbf{r}_i - \mathbf{r}_j\right|\right), \tag{1}$$

where $\hat{p}_i$ is the momentum of the ith electron and $\hat{\mathcal{V}}$ is the Coulomb potential. In the minimal-coupling Hamiltonian, the effects of an external electromagnetic field are included by the substitution $\hat{p}_i \to \hat{p}_i - \frac{q_i}{c}\hat{\mathbf{A}}$ where q_i is the charge and $\hat{\mathbf{A}}$ is the electronic magnetic vector potential [1, 16]. The minimal coupling is well-suited to discuss X-ray diffraction, which arises from the $\mathbf{A}^2$ term, but it is often more convenient to work with the electric and magnetic fields (which are gauge invariant) rather than the vector potential. This is accomplished by the Power–Zienau canonical transformation [1, 16]. The Hamiltonian of the system then becomes

$$\hat{H}_S(t) = \hat{H} + \hat{H}_{\text{int}}(t), \tag{2}$$

where H is the material Hamiltonian and, in the dipole approximation, the interaction Hamiltonian is

$$\hat{H}_{\text{int}}(t) = -\int d\mathbf{r}\left(\hat{\mathcal{E}}(\mathbf{r},t) + \hat{\mathcal{E}}^{\dagger}(\mathbf{r},t)\right)\cdot\hat{\mu}, \tag{3}$$

with $\hat{\mu}$ the dipole operator and $\left(\hat{\mathcal{E}} + \hat{\mathcal{E}}^{\dagger}\right) \equiv \hat{\mathbf{E}}$ is the electric field which is separated into positive and negative Fourier components. Within the rotating wave approximation, the dipole moment is also separated into positive and negative Fourier components $\hat{\mu} = \hat{V} + \hat{V}^{\dagger}$ and only the terms $\hat{\mathcal{E}}\hat{V}^{\dagger} + \hat{\mathcal{E}}^{\dagger}\hat{V}$ are retained [1]. Throughout, we work in the interaction picture with respect to this Hamiltonian and in the Hartree units, which simplifies the coefficients in the resulting expressions. The detected quantity in the signals coincided here is the integrated photon number

$$S(\Lambda) = \int dt\left\langle \dot{\hat{N}}(t)\right\rangle = \int dtd\mathbf{r}\,\Im\left[\hat{\mathcal{E}}^{\dagger}(\mathbf{r},t)\cdot\langle\hat{\mu}(t)\rangle\right], \tag{4}$$

where the last equality follows from the Heisenberg equation of motion for the photon number operator and the signal is a function of the parameters defining the pulse envelope (collectively denoted Λ). In the following, we take the field to be polarized along the dipole and avoid the tensor notation (this restriction is easily relaxed). Note that this form for the signal does not include any frequency- or time-resolved detection. This could be done by adding gating functions [11, 17, 18] in nonlinear spectroscopic applications; the electric field is a superposition of more than one externally applied pulses or continuous wave (CW) laser field. To simulate such experiments, we calculate the propagated wavefunction of the driven system

$$|\psi(t)\rangle = \hat{U}(t)|\psi_0\rangle, \tag{5}$$

where the time-evolution operator $\hat{U}(t)$ follows from the Schrödinger equation

$$\mathrm{i}\frac{\partial}{\partial t}|\psi(t)\rangle = \hat{H}_{\text{int}}|\psi(t)\rangle \rightarrow \hat{U}(t) = \exp_{+}\left(-\mathrm{i}\int_{0}^{t} d\tau \hat{H}_{\text{int}}(\tau)\right), \tag{6}$$

where e_{+} stands for the positive time-ordered exponential. As a reminder, we work in the interaction picture where the states carry the interaction propagation and the operators carry the field-free propagators so that the time-dependent dipole moment is

$$\hat{\mu}(t) = e^{\mathrm{i}\hat{H}t}\hat{\mu}\, e^{-\mathrm{i}\hat{H}t}, \tag{7}$$

and its expectation value is then written

$$\langle\hat{\mu}(t)\rangle = \langle\psi(t)|\hat{\mu}(t)|\psi(t)\rangle = \left\langle\psi_0\middle|\hat{U}^{\dagger}(t)\hat{\mu}(t)\hat{U}(t)\middle|\psi_0\right\rangle. \tag{8}$$

To analyze particular experiments, we expand the interaction propagator (time-ordered exponential) perturbatively in powers of the electric field. Together with an explicit form for the material Hamiltonian H, the previous equations form the basis for the perturbative description of the nonlinear signals considered below.

2.1 Time-Resolved Four-Wave Mixing

Linear signals are determined by the first order $\hat{H}_{\text{int}}$. In the X-ray regime, such signals include X-ray absorption near edge structure (XANES) and extended X-ray absorption fine structure (EXAFS) [19–21]. The third order techniques (four-wave mixing) provide more detailed information [6, 22]. In this section, we describe a class of techniques that utilize four pulses well-separated in time. The pulses interact with the molecule sequentially and the signal is defined as the change in transmission of the final pulse. In the limit of ultrashort pulses, the signal is parameterized by the time delays between successive pulses. In the semiclassical approximation (where the electric field is treated classically and the molecule is quantum), we have

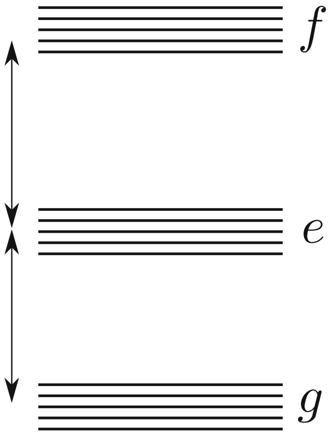

Fig. 1 Schematic depiction of the energy levels under consideration. The g, e, and f are ground state, single core excitation, and double core excitation manifolds. The fine structures of the manifolds are given by valence excitations on *top* of the core excited states whereas in the optical regime they represent vibrational excitations on *top* of the valence excited states

$$E(t) = \sum_{p=1,2,3,4} \tilde{\mathcal{E}}\left(t - \bar{\tau}_p\right) e^{i\mathbf{k}_p \cdot \mathbf{r} - i\omega_p\left(t - \bar{\tau}_p\right) + i\phi_p} + \text{c.c.} \tag{9}$$

where ϕ_p is the phase of the pth pulse, $\bar{\tau}_p$, ω_p the central times and frequencies of the temporal and spectral pulse envelopes and $\tilde{\mathcal{E}}_p(t)$ the temporal pulse envelopes centered at $t = 0$. The system interacts once with each pulse and the signal can then be plotted as a function of the pulse parameters. The terms in the perturbative expansions are conveniently depicted diagrammatically. Besides facilitating enumeration of all terms, this procedure allows one to write quickly the signal corresponding to a particular diagram and to discern in which time periods particular coherences appear. For macroscopic samples longer than the relevant radiation wavelength a delta function $\delta(-\mathbf{k}_4 \pm \mathbf{k}_3 \pm \mathbf{k}_2 \pm \mathbf{k}_1)$ results. This is known as phase matching for our level and dipole scheme. The ground state, singly excited state and doubly excited state manifolds involved in these four-wave mixing experiment are shown in Fig. 1. The three possible signals are denoted $\mathbf{k}_{\text{I}} \equiv -\mathbf{k}_1 + \mathbf{k}_2 + \mathbf{k}_3$, $\mathbf{k}_{\text{II}} \equiv \mathbf{k}_1 - \mathbf{k}_2 + \mathbf{k}_3$, and $\mathbf{k}_{\text{III}} \equiv \mathbf{k}_1 + \mathbf{k}_2 - \mathbf{k}_3$. Below we focus on two techniques: the double quantum coherence four wave mixing, and the stimulated Raman simulations, and analysis of these signals are given later. The diagrams of other two four-wave mixing techniques are also provided in Fig. 2 for reference.

2.2 *Double-Quantum-Coherence Signal*

We focus on the DQC $\mathbf{k}_{\text{III}}$ signal, which is particularly sensitive to electron correlations. The pulse order and the diagrams corresponding to the DQC signal are depicted in Figs. 3 and 4, respectively. During the time period $t_2 \equiv \tau_2 - \tau_1$, the system is in a coherence between the doubly-excited states and the ground state.

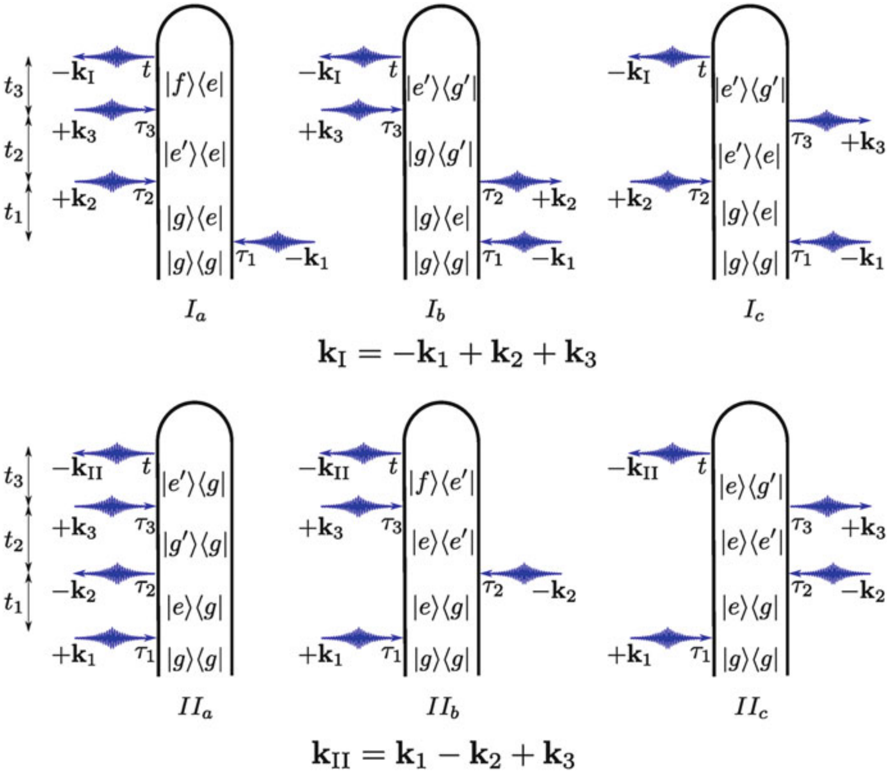

Fig. 2 Loop diagrams for the $\mathbf{k}_\mathrm{I}$ (*top row*) and $\mathbf{k}_\mathrm{II}$ (*bottom row*) signals. The system begins in the ground state (or more generally, a distribution of states as in (30)) and then interacts once with each of the four sequentially applied pulses. For diagram rules see [23]

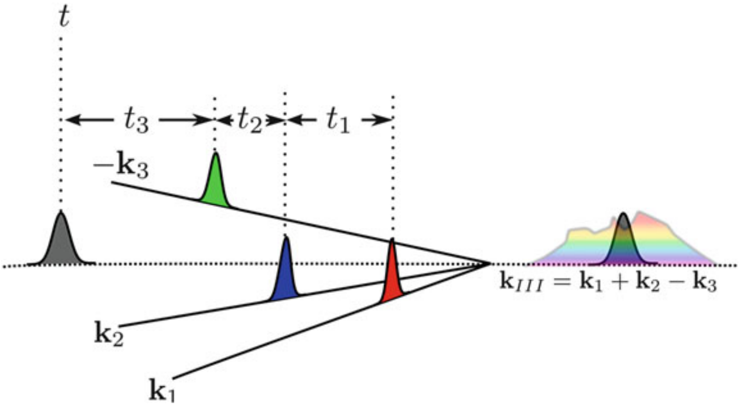

Fig. 3 Schematic depiction of the double quantum coherence technique. Four time-ordered pulses are shown impinging on the sample from different directions. The transmission of the final pulse is recorded as a function of the delay times or their conjugate frequencies. Figure taken from [24]

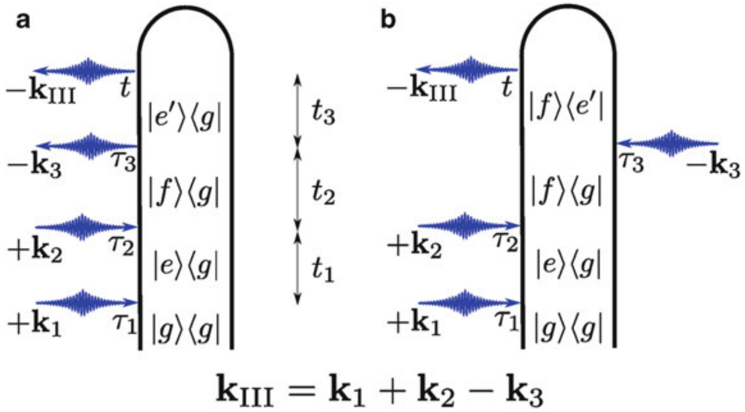

Fig. 4 The two loop diagrams contributing to the $\mathbf{k}_{\text{III}}$ (DQC) signal. The system begins in the ground state (or more generally, a distribution of states as in (30)) and then interacts once with each of the four sequentially applied pulses. Note that the phase choice for this signal ($\mathbf{k}_{\text{III}} = + \ \mathbf{k}_1 + \mathbf{k}_2 - \mathbf{k}_3$) guarantees that the second excitation manifold is reached and provides resonances between the ground state and this manifold

From the diagrams in Fig. 4, one can immediately obtain the time-domain signals:

$$\begin{aligned} S_{\mathbf{k}_{\text{III}}}(\Lambda) = \ & \Im \int dt \int_0^\infty dt_3 dt_2 dt_1 \tilde{\mathcal{E}}_4(t - \bar{\tau}_4) e^{\mathrm{i}\omega_4 (t-\bar{\tau}_4)} \tilde{\mathcal{E}}_3(t - t_3 - \bar{\tau}_3) e^{\mathrm{i}\omega_3 (t-t_3-\bar{\tau}_3)} \\ & \times \tilde{\mathcal{E}}_2(t - t_3 - t_2 - \bar{\tau}_2) e^{\mathrm{i}\omega_2 (t-t_3-t_2-\bar{\tau}_2)} \tilde{\mathcal{E}}_1(t - t_3 - t_2 - t_1 - \bar{\tau}_1) \\ & \times e^{-\mathrm{i}\omega_1 (t-t_3-t_2-t_1-\bar{\tau}_1)} \big[\big\langle \psi_0 \big| \hat{U}^\dagger (t_1 + t_2 + t_3) \hat{V} \, \hat{U}(t_3) \hat{V} \, \hat{U}(t_2) \hat{V}^\dagger \hat{U}(t_1) \hat{V}^\dagger \big| \psi_0 \big\rangle \\ & - \big\langle \psi_0 \big| \hat{U}^\dagger (t_1 + t_2) \hat{V} \, \hat{U}^\dagger (t_3) \hat{V} \, \hat{U}(t_2 + t_3) \hat{V}^\dagger \hat{U}(t_1) \hat{V}^\dagger \big| \psi_0 \big\rangle \big] e^{\mathrm{i}(\phi_1 + \phi_2 - \phi_3 - \phi_4)} \end{aligned} . \tag{10}$$

It is important to note that this signal carries a phase $\phi_1 + \phi_2 - \phi_3 - \phi_4$ which, when randomly averaged, causes the signal to vanish. Observing this signal therefore requires phase control of the pulses. For pulses of finite duration, the distinction between the actual interaction times and delays between successive interaction times (the τ_p and t_p, respectively) and the central times of the pulse envelopes and delays between successive central times (the $\bar{\tau}_p$ and $\bar{t}_p$, respectively) must be made. The former are dummy variables of integration whereas the latter are control parameters which determine the signal. It is common to perform such experiments with very short, well-separated pulses. The resulting impulsive signal is then well parameterized by the interpulse delay times ($\bar{t}_1$, $\bar{t}_2$, and $\bar{t}_3$).

To understand the impulsive signal better, we may replace all τ_p by $\bar{\tau}_p$ and t_p by $\bar{t}_p$ in Fig. 4. The signal may be Fourier transformed with respect to any or all of these delays. From the diagrams, we can see that transforming with respect to $\bar{t}_2$ $(\bar{t}_1)$ reveals resonances at double (single) excitations from the ground state whereas the t_3 resonances contain single excitations from the ground state or double excitations from the single-excitation manifold depending on the diagram. We can therefore fix one of $\bar{t}_1$ or $\bar{t}_3$ and transform with respect to the other two time arguments to obtain a two-dimensional frequency plot which reveals correlations between the double excitations and single excitations (either from the ground state or the single-excitation manifold). We denote this impulsive signal by a 0 superscript:

$$\begin{aligned} S^0_{\mathbf{k}_{\mathrm{III}}}(\bar{t}_3,\bar{t}_2,\bar{t}_1) = {} & \mathcal{E}_4\mathcal{E}_3\mathcal{E}_2\mathcal{E}_1 e^{-\mathrm{i}\omega_1\bar{t}_1-\mathrm{i}(\omega_1+\omega_2)\bar{t}_2-\mathrm{i}(\omega_1+\omega_2+\omega_3)\bar{t}_3}\delta(\omega_1+\omega_2-\omega_3-\omega_4) \\ & \times \left[\left\langle\psi_0\middle|\hat{U}^\dagger(\bar{t}_1+\bar{t}_2+\bar{t}_3)\hat{V}\,\hat{U}(\bar{t}_3)\hat{V}\,\hat{U}(\bar{t}_2)\hat{V}^\dagger\hat{U}(\bar{t}_1)\hat{V}^\dagger\middle|\psi_0\right\rangle\right. \\ & \left. - \left\langle\psi_0\middle|\hat{U}^\dagger(\bar{t}_1+\bar{t}_2)\hat{V}\,\hat{U}^\dagger(\bar{t}_3)\hat{V}\,\hat{U}(\bar{t}_2+\bar{t}_3)\hat{V}^\dagger\hat{U}(\bar{t}_1)\hat{V}^\dagger\middle|\psi_0\right\rangle\right]. \end{aligned} \tag{11}$$

The signal is then Fourier transformed:

$$S_{\mathbf{k}_{\mathrm{III}}}(\Omega_3,\Omega_2,\Omega_1) = \int d\bar{t}_3 d\bar{t}_2 d\bar{t}_1 S_{\mathbf{k}_{\mathrm{III}}}(\bar{t}_3,\bar{t}_2,\bar{t}_1)e^{\mathrm{i}(\Omega_3\bar{t}_3+\Omega_2\bar{t}_2+\Omega_1\bar{t}_1)}, \tag{12}$$

in order to reveal resonances better. Finite pulse envelopes may now be incorporated and, when the correlation functions are expanded in material eigenstates, we obtain

$$\begin{aligned} S_{\mathbf{k}_{\mathrm{III}},\mathrm{a}}(\Omega_3,\Omega_2,\Omega_1) = {} & \sum_{fe'e}\frac{\widetilde{\mathcal{E}}^*_4\left(\omega_4-\omega_{e'g}\right)V_{ge'}\widetilde{\mathcal{E}}^*_3\left(\omega_3-\omega_{fe'}\right)V_{e'f}\widetilde{\mathcal{E}}_2\left(\omega_3-\omega_{fe}\right)V_{fe}}{\left(\Omega_3-\omega_{e'g}+\mathrm{i}\gamma_{e'g}\right)\left(\Omega_2-\omega_{fg}-\mathrm{i}\gamma_{fg}\right)} \\ & \times\frac{\widetilde{\mathcal{E}}_1\left(\omega_1-\omega_{eg}\right)V_{eg}}{\left(\Omega_1-\omega_{eg}-\mathrm{i}\gamma_{eg}\right)}, \end{aligned} \tag{13}$$

$$\begin{aligned} S_{\mathbf{k}_{\mathrm{III}},\mathrm{b}}(\Omega_3,\Omega_2,\Omega_1) = {} & \sum_{fe'e}\frac{\widetilde{\mathcal{E}}^*_4\left(\omega_4-\omega_{fe'}\right)V_{e'f}\widetilde{\mathcal{E}}^*_3\left(\omega_3-\omega_{e'g}\right)V_{ge'}\widetilde{\mathcal{E}}_2\left(\omega_3-\omega_{fe}\right)V^*_{fe}}{\left(\Omega_3-\omega_{fe'}+\mathrm{i}\gamma_{fe'}\right)\left(\Omega_2-\omega_{fg}-\mathrm{i}\gamma_{fg}\right)} \\ & \times\frac{\widetilde{\mathcal{E}}_1\left(\omega_1-\omega_{eg}\right)V^*_{eg}}{\left(\Omega_1-\omega_{eg}-\mathrm{i}\gamma_{eg}\right)}, \end{aligned} \tag{14}$$

where $\omega_{ij} \equiv \varepsilon_i - \varepsilon_j$ and γ_{ij} are the frequency and the dephasing rate of the $i \rightarrow j$ transition, respectively. The contributions from diagrams *a* and *b* may be read directly from Fig. 4. The numerator contains all transition dipoles as well as the field-envelope factors which determine the material transitions permitted by the bandwidths. The denominators contain the resonance factors for these material transitions.

At the level of Hartree theory, which assumes *independent electrons,* the DQC signal vanishes because of interference. TDHF (or TDDFT) goes one step further and provides a picture of *independent transitions* (quasiparticles). Here the signal no longer vanishes, but shows a limited number of peaks. When correlation effects are fully incorporated, the many-electron wavefunctions become superpositions of states with different numbers and types of e-h pairs. The Ω_2 and Ω_3 axes then contain many more peaks corresponding to all many-body states (in the frequency range spanned by the pulse bandwidths), which project into the doubly-excited states. Thus, along Ω_2 the peaks are shifted, reflecting the level of theory used to describe electron correlations. Along Ω_3, the effect is even more dramatic and new peaks show up corresponding to splittings between various levels. We show the X-ray DQC signals of formamide as an example in Sect. 4.3. This highly-resolved two-dimensional spectrum provides an invaluable direct dynamical probe of electron correlations (both energies and wavefunctions) [25, 26].

2.3 Stimulated X-Ray Raman Spectroscopy

Linear techniques contain the single-excitation spectrum whereas we have just seen that the DQC ($\mathbf{k}_{\mathrm{III}}$) signal gives access to the double-excitation spectrum. Both of these spectra thus characterize the intermanifold structure of the material (the transitions between manifolds). We may obtain a window into the intramanifold structure (transitions within the same manifold) by using the stimulated Raman signal (SXRS in the X-ray regime) [2, 27, 28]. As with the DQC signal, this technique is third-order (involving four interactions with the electromagnetic field). However, rather than four sequential pulses, 1D-SXRS employs only two pulses, each of which interacts twice with the material. This process is shown diagramatically in Fig. 5. Note that, because the pair of interactions with each pulse are of opposite Hermiticity, the overall absolute phase is $\phi_1 - \phi_1 + \phi_4 - \phi_4 = 0$ and this technique therefore does not require phase control to obtain a finite signal.

The first pulse in the SXRS process creates a superposition of excited states in the ground state manifold. After a controlled delay period, the sample interacts with the second pulse which returns the system to the original state.

For calculating this signal, we find it more convenient to work with the actual interaction times τ rather than the time delays t_j $(j = 1, 2, 3)$. It is straightforward to write down a time-domain expression for the 1D-SXRS signal directly from the diagrams in Fig. 5. Its form is similar to (10):

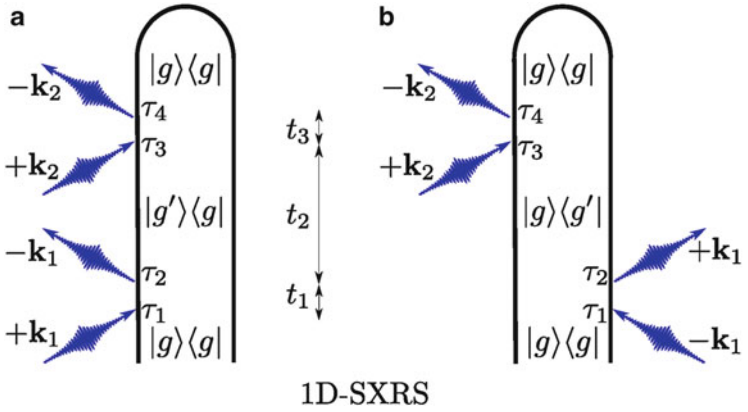

Fig. 5 Two contributing loop diagrams (labeled as a, b in the figure) for the 1D-SXRS technique. As before, the system begins in the ground state but this time interacts twice with each of the two sequentially applied pulses. Note that the phase for this signal ($\phi_1 - \phi_1 + \phi_2 - \phi_2$) automatically vanishes, making the signal incoherent. The first pulse prepares a wavepacket of valence excitations that evolves for the interpulse delay period before being probed with the second pulse

$$\begin{aligned} S_{\mathrm{SXRS}}(\Lambda) = \Im \int d\tau_4 \int_{-\infty}^{\tau_4} d\tau_3 \int_{-\infty}^{\tau_3} d\tau_2 \int_{-\infty}^{\tau_2} d\tau_1 (\mathrm{i})^3 \mathcal{E}_2^*(\tau_4)\mathcal{E}(\tau_3) \\ \times \Big[\mathcal{E}_1^*(\tau_2)\mathcal{E}_1(\tau_1)\big\langle\psi_0\big|\hat{V}(\tau_4)\hat{V}^\dagger(\tau_3)\hat{V}(\tau_2)\hat{V}^\dagger(\tau_1)\big|\psi_0\big\rangle \quad . \\ + \mathcal{E}_1(\tau_2)\mathcal{E}_1^*(\tau_1)\big\langle\psi_0\big|\hat{V}^\dagger(\tau_1)\hat{V}(\tau_2)\hat{V}(\tau_4)\hat{V}^\dagger(\tau_3)\big|\psi_0\big\rangle\Big] \end{aligned} \tag{15}$$

Because the interactions are paired within a given pulse and the pulses are temporally well-separated, we may extend the upper limit for the τ_2 integration to infinity. This permits us to define formally the polarizability $\hat{\alpha}_p$ induced by the pth pulse:

$$\hat{\alpha}_p(\Lambda_p) \equiv \mathrm{i}\int_{-\infty}^{\infty} d\tau \int_{-\infty}^{\tau} d\tau' \hat{V}(\tau)\hat{V}^\dagger(\tau')\mathcal{E}_p^*(\tau)\mathcal{E}_p(\tau'), \tag{16}$$

which is both a material operator and a function of Λ_p, the parameters of the pth pulse. In the limit of ultrashort pulses, the primary Λ_p parameter is the central pulse time $\bar{\tau}_p$ and the principal control variable for the 1D-SXRS signal is the interpulse delay $T = \bar{\tau}_2 - \tau_1$ and the signal is recast as

$$S(T) = \Re\big[\langle\hat{\alpha}_2(T)\hat{\alpha}_1(0)\rangle + \big\langle\hat{\alpha}_1^*(0)\hat{\alpha}_2(T)\big\rangle\big], \tag{17}$$

where we have set $\bar{\tau}_1 = 0$ as the origin of time. Taking matrix elements in the Hamiltonian eigenbasis gives the sum-over-states expression

$$\alpha_{p,g'g''} \equiv \mathrm{i}\sum_e V_{g'e}V_{eg''}\int_{-\infty}^{\infty} d\tau_2 \int_{-\infty}^{\tau_2} d\tau_1 \mathcal{E}_p^*(\tau_2)\mathcal{E}_p(\tau_1) e^{\mathrm{i}\left(\omega_p-\omega_{eg'}+\mathrm{i}\gamma_e\right)\tau_2-\mathrm{i}\left(\omega_p-\omega_{eg''}+\mathrm{i}\gamma_e\right)\tau_1}. \tag{18}$$

Here, ω_{ev} is the frequency for the $v \rightarrow e$ transition, and γ_e is the inverse of the excitation lifetime. In some applications, it may be more convenient to work in the frequency domain where the spectral (rather than temporal) field envelopes are used. This can be accomplished by explicitly writing the propagators in (16) and replacing the temporal field envelopes by their Fourier transforms yielding

$$\begin{gathered}\hat{\alpha}_p = \int \frac{d\omega d\omega_p d\omega'_p}{(2\pi)^3}\mathcal{E}_p^*\left(\omega'_p\right)\mathcal{E}_p(\omega_p) \\ \frac{1}{\omega+\omega_p-\omega'_p-\hat{H}_0+\mathrm{i}\eta}\hat{V}\frac{1}{\omega+\omega_p-\hat{H}_0+\mathrm{i}\eta}\hat{V}^{\dagger}\frac{1}{\omega-\hat{H}_0+\mathrm{i}\eta}.\end{gathered} \tag{19}$$

Expanding in eigenstates then gives the matrix elements

$$\alpha_{p,g',g''} = \sum_e \frac{V_{g'e}V_{eg''}}{2\pi}\int d\omega \frac{\mathcal{E}_p^*(\omega)\mathcal{E}_p\left(\omega+\omega_{g'g''}\right)}{\omega+\omega_p-\omega_{eg'}+\mathrm{i}\gamma_e}. \tag{20}$$

Starting from (20), we may now write the frequency-domain 1D-SXRS signal as

$$\begin{aligned}S_{\mathrm{SXRS}}(\Omega) = \quad & -\sum_{g'}\frac{\Re\left(\alpha_{2;gg'}\alpha_{1;g'g}\right)\left(\gamma_{g'}-\mathrm{i}\Omega\right)+\Im\left(\alpha_{2;gg'}\alpha_{1;g'g}\right)\omega_{g'g}}{\gamma_{g'}^2-2\mathrm{i}\gamma_{g'}\Omega-\Omega^2+\omega_{g'g}^2} \\ & +\frac{\Re\left(\alpha_{1;gg'}^*\alpha_{2;g'g}\right)\left(\gamma_{g'}-\mathrm{i}\Omega\right)+\Im\left(\alpha_{1;gg'}^*\alpha_{2;g'g}\right)\omega_{g'g}}{\gamma_{g'}^2-2\mathrm{i}\gamma_{g'}\Omega-\Omega^2+\omega_{g'g}^2},\end{aligned} \tag{21}$$

which is the Fourier transform of (15) with respect to the interpulse delay T. The first term in (17) and (21) can be viewed as a valence wavepacket $\alpha_1|\psi_0\rangle$, created by pulse 1, which propagates forward in time T and overlaps with a wavepacket $\langle\psi_0|\alpha_2$ created by pulse 2. The second term can be viewed as a wavepacket $\alpha_2|\psi_0\rangle$ created by pulse 2 propagating backward in time $-T$ to overlap with the wavepacket $\langle\psi_0|\alpha_1^{\dagger}$ created by pulse 1. The SXRS technique creates a wavepacket of valence excitations and, after a specified delay period T, probes this wavepacket so as to track its evolution. A 2D extension of this 1D-SXRS in which three successive pulses are employed is shown in Fig. 6. The resulting signal $S_{\mathrm{SXRS}}(\Omega_1, \Omega_2)$ requires expansion to fifth order in the field and carries information about correlations between dynamics during the two delay periods which would not be available in 1D-SXRS [29]. This technique can also be applied following a pump pulse which prepares the system by exciting a core hole. The subsequent SXRS process then

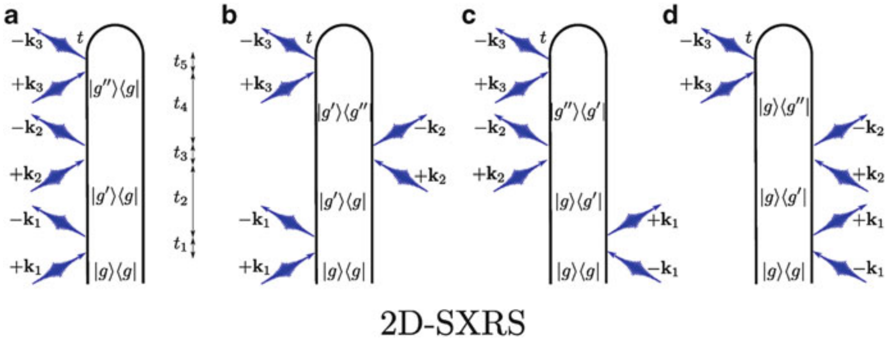

Fig. 6 Four contributing loop diagrams (labeled as a, b, c, d in the figure) for the 2D-SXRS technique. The system begins in the ground state then interacts twice with each of three sequentially applied pulses. As with 1D-SXRS, the phase vanishes and the signal is incoherent. The additional delay period allows information about couplings and correlations of valence excitations that are not available in 1D-SXRS to be extracted

creates a valence excitation and tracks its motion along the potential energy surface produced by the core hole [30].

2.4 *Correlation Function Expressions for SXRS Signals*

In the previous section, we defined $\hat{\alpha}_p$ by combining two time-dependent dipole interactions (excitation and de-excitation) as well as the pulse envelope (see (16)). All time-dependence is then encoded into the polarizability $\hat{\alpha}_p$ and the result (see (17)) is compact but too complicated. Although perfectly suited to an expansion in eigenstates, as shown in the previous section, this form of $\hat{\alpha}_p$ suffers from some drawbacks. Recalling the definition of operator time-dependence in the interaction picture (see (7)), we see that there are three time propagation periods. This definition for the polarizability therefore contains material propagation both for interpulse and intrapulse time periods. Because these occur on two different time-scales, a separation permits different treatments. In particular, it is then possible to treat the intrapulse propagation perturbatively while preserving the full form of the longer-time interpulse propagator.

That the two impinging fields are temporally well-separated guarantees that there exist $\tilde{\tau}_{1i}$ and $\tilde{\tau}_{1f}$ ($\tilde{\tau}_{2i}$ and $\tilde{\tau}_{2f}$), the initial and final times of the first (second) pulse. The $\tilde{\tau}_{pi}$ and $\tilde{\tau}_{pf}$ are used to bound the possible interaction times with the pth pulse. They are a formal tool used to separate the interpulse propagation from the intrapulse propagation and can be unambiguously defined as

$$\begin{array}{l}\tilde{\tau}_{pi} \equiv \sup\left\{t : E_p(t') = 0 \forall t' < t\right\} \\ \tilde{\tau}_{pf} \equiv \inf\left\{t : E_p(t') = 0 \forall t' > t\right\}\end{array}, \tag{22}$$

making the procedure unarbitrary. Explicitly writing the time propagators in an exponential form, we can recast the material correlation function pertaining to diagram a in Fig. 5 (diagram b in Fig. 5 follows similarly so we exclude it for the sake of brevity) as

$$\left\langle e^{\mathrm{i}\hat{H}_0\tau_4}\hat{V}e^{-\mathrm{i}\hat{\hat{H}}_0(\tau_4-\tau_3)}\hat{V}^{\dagger}e^{-\mathrm{i}\hat{H}_0\tau_3}e^{\mathrm{i}\hat{H}_0\tau_2}\hat{V}e^{-\mathrm{i}\hat{\hat{H}}_0(\tau_2-\tau_1)}\hat{V}^{\dagger}e^{-\mathrm{i}\hat{H}_0\tau_1}\right\rangle. \tag{23}$$

Inserting identities to separate the propagation at $\tilde{\tau}$ then gives

$$\begin{array}{l}\left\langle e^{i\hat{H}_0\tilde{\tau}_{2f}}e^{\mathrm{i}\hat{H}_0\left(\tau_4-\tilde{\tau}_{2f}\right)}\hat{V}\,e^{-\mathrm{i}\hat{\hat{H}}_0}(\tau_4-\tau_3)\hat{V}^{\dagger}e^{-\mathrm{i}\hat{H}_0(\tau_3-\tilde{\tau}_{2i})}e^{\mathrm{i}\hat{H}_0\left(\tilde{\tau}_{2i}-\tilde{\tau}_{1f}\right)}\right. \\ \left.\times e^{\mathrm{i}\hat{H}_0\left(\tau_2-\tilde{\tau}_{1f}\right)}\hat{V}\,e^{-\mathrm{i}\hat{\hat{H}}_0}(\tau_2-\tau_1)\hat{V}^{\dagger}e^{-\mathrm{i}\hat{H}_0(\tau_1-\tilde{\tau}_{1i})}e^{-\mathrm{i}\hat{H}_0\tilde{\tau}_{1i}}\right\rangle.\end{array} \tag{24}$$

We thus define the polarizability as

$$\hat{\alpha}_p\left(\tilde{\tau}_{pf},\tilde{\tau}_{pi}\right) \equiv \mathrm{i}\int_{-\infty}^{\infty}d\tau\int_{-\infty}^{\tau}d\tau' e^{\mathrm{i}\hat{H}_0\left(\tau-\tilde{\tau}_{pf}\right)}\hat{V}\,e^{-\mathrm{i}\hat{\hat{H}}_0(\tau-\tau')}\hat{V}^{\dagger}e^{-\mathrm{i}\hat{H}_0\left(\tau'-\tilde{\tau}_{pi}\right)}\mathcal{E}^{*}_{p}(\tau)\mathcal{E}_{p}(\tau'). \tag{25}$$

where the properties of the pulse and the choice of the $\tilde{\tau}$ guarantee the appropriate sign of the propagators. This is an operator in the valence excitation space. It may be recast in the frequency domain as before:

$$\begin{aligned}\hat{\alpha}_p\left(\tilde{\tau}_{pf},\tilde{\tau}_{pi}\right) \quad &= \int\frac{d\omega d\omega_p d\omega'_p}{(2\pi)^3}\mathcal{E}^{*}_{p}\left(\omega'_p\right)\mathcal{E}_p\left(\omega_p\right)e^{-\mathrm{i}\omega\left(\tilde{\tau}_{pf}-\tilde{\tau}_{pi}\right)}e^{-\mathrm{i}\left(\omega_p-\omega'_p\right)\tilde{\tau}_{pf}} \\ &\quad\times\frac{1}{\omega+\omega_p-\omega'_p-\hat{H}_0+\mathrm{i}\eta}\hat{V}\frac{1}{\omega+\omega_p-\hat{H}_0+\mathrm{i}\eta}\hat{V}^{\dagger}\frac{1}{\omega-\hat{H}_0+\mathrm{i}\eta}\end{aligned}, \tag{26}$$

and may differ from (19) in the appearance of $\tilde{\tau}_p$-dependent phase-factors. Note that, because the choice of the $\tilde{\tau}_p$ is set by the pulse shape, their appearance on the left hand side is not necessary and we merely include them for clarity. With this definition, the contribution to the signal from diagram a in Fig. 5 is

$$S_{\mathrm{a}} = \Re\left[\left\langle e^{\mathrm{i}\hat{H}_0\tilde{\tau}_{2f}}\hat{\alpha}_2\left(\tilde{\tau}_{2f},\tilde{\tau}_{2i}\right)e^{-\mathrm{i}\hat{H}_0\left(\tilde{\tau}_{2i}-\tilde{\tau}_{1f}\right)}\hat{\alpha}_1\left(\tilde{\tau}_{1f},\tilde{\tau}_{1i}\right)e^{-\mathrm{i}\hat{H}_0\tilde{\tau}_{1i}}\right\rangle\right]. \tag{27}$$

Defining the duration of the pth pulse $t_p \equiv \tilde{\tau}_{pf} - \tilde{\tau}_{pi}$ and the interpulse delay $T \equiv \tilde{\tau}_{2i} - \tilde{\tau}_{1f}$ we have, in the limit of well-separated pulses, $T >> t_p p \in \{1, 2\}$. Assuming that, having accounted for the finite pulse duration in the definition of α, we may take $t_p \to 0$ for the purposes of the free evolution in (27), the signal becomes

$$S_{\mathrm{a}}(T) = \Re\left[\left\langle e^{\mathrm{i}\hat{H}_0 T}\hat{\alpha}_2 e^{-\mathrm{i}\hat{H}_0 T}\hat{\alpha}_1\right\rangle\right] = \Re[\langle\hat{\alpha}_2(T)\hat{\alpha}_1(0)\rangle], \tag{28}$$

where we have set $\tilde{\tau}_{1i} = \tau_{1f}$ as the zero point of time and the last equality defines the interaction picture polarizability $\alpha_p(t)$. Note that this expression for $S_a(T)$ matches the first term in (17) (with the second term standing for $S_{\mathrm{b}}(T)$). Besides being necessary for certain applications, the separation of interpulse and intrapulse propagations prominently features the dependence on the key time parameter, the interpulse delay T. All other parameters defining the pulses are encoded in the definition of the $\hat{\alpha}_p$. We pause to recall that the only assumption necessary in reaching (28) (just as for (17)) is that the interpulse delay be much larger than the temporal pulse widths.

It is important to note that separating interpulse and intrapulse propagation periods yields a formally identical expression and may seem an unnecessary artifice, as indeed it is within an eigenstate representation. The utility then is manifest when the eigenstates are prohibitively expensive to calculate. For example, in the configuration interaction representation, states are expanded in a basis consisting of the many-body ground state (the orbitals being filled up to some maximum energy level) and excitations on this ground state obtained by successively higher orders of electron creation-annihilation operator pairs:

$$|\psi\rangle = |g\rangle + \sum_{ij} C_{ij}\hat{c}_i^{\dagger}\hat{c}_j|g\rangle + \dots \tag{29}$$

Because the material may generally be taken to begin an experiment in the many-body ground state, perturbative treatment of nonlinear spectroscopies naturally produces such states. At low order, there are many fewer states in this treatment than in the full eigenbasis and a significant numerical speedup can be achieved. In order to exploit this form requires a similar recasting of the $\hat{\alpha}_p$ and this is explored in Sect. 4.2. Corresponding expressions for the 2D signal $S_{\mathrm{SXRS}}(T_2, T_1)$ (Fig. 6) are given in [29, 31].

2.5 Discussion of Signals

In the above sections we provided two different types of expressions for the DQC and SXRS signals. The first ((10) and (15)) are given in terms of time correlation functions of the dipole operator. This form is convenient for direct *ab initio* dynamic simulations of electrons and nuclei [31, 32]. It can take into account, e.g., in nonadiabatic dynamics, conical intersections, etc. Real-time time-dependent density functional theory can then be applied to calculate the signal. Alternatively, the second procedure ((13), and (17)–(20)) expands the correlation functions in molecular eigenstates. This is convenient for simpler models when only a few electronic states participate and for relatively small systems where the many-body states can be computed. The sum-over-states expansions also facilitate interpretation of the resulting signal as the meaning of the various resonances is transparent in this form. Both the correlation function and sum-over-states forms may be displayed either in the time-domain (as a function of $\bar{t}_3, \bar{t}_2, \bar{t}_1$) or the frequency domain (as a function of the conjugate variables Ω_3, Ω_2, Ω_1). It is often useful to employ a mixed representation, e.g., $S(\Omega_1, t_2, \Omega_3)$, which is 2D in frequency and 1D in time so that correlations between resonances observed at the two frequencies can be observed and monitored as the time argument is allowed to vary. These techniques can therefore provide a high degree of selectivity and carry a rich abundance of information on the electronic and nuclear structure and dynamics.

Our correlation function expressions (10) and (15) are given by the expectation values with respect to $|\psi_0\rangle$. Alternatively, we may describe the system using the density matrix

$$\hat{\rho} = \sum_i P_i |\psi_i\rangle\langle\psi_i|, \tag{30}$$

whose dynamics is determined by the Liouville equation

$$\dot{\hat{\rho}} = -\mathrm{i}\left[\hat{H}, \hat{\rho}\right] - \mathrm{i}\left[\hat{H}_{\text{int}}, \hat{\rho}\right]. \tag{31}$$

Here P_i is the probability that the system is found in state $|\psi_i\rangle$. When all degrees of freedom are treated at the Hamiltonian level, it is more convenient to remain in Hilbert space rather than recasting in Liouville space (as is done in [1]). This facilitates computations because Hilbert space has far fewer dimensions than the associated Liouville space. In these cases, the above equations may still be utilized formally with appropriate choice of the P_i. In terms of the density matrix, the expectation value of the dipole is given by

$$\langle\hat{\mu}(t)\rangle \equiv \mathrm{Tr}[\hat{\mu}(t)\hat{\rho}(t)], \tag{32}$$

and we may expand $\rho(t)$ perturbatively to arbitrary order in the interaction Hamiltonian

$$\begin{aligned} \hat{\rho}^{(n)}(t) = (\mathrm{i})^n \int d\mathbf{r}_n \ldots d\mathbf{r}_1 \int_{t_0}^{t} d\tau_n \ldots \int_{t_0}^{\tau_2} d\tau_1 E(\mathbf{r}_n, \tau_n) \ldots E(\mathbf{r}_1, \tau_1) \\ \times [\hat{\mu}(\tau_n), [\ldots, [\hat{\mu}(\tau_1), \hat{\rho}]] \ldots]. \end{aligned} \tag{33}$$

One can then include the effects of coupling to a bath by introducing further terms to the equation of motion – see (30) – which represent the dissipation of system excitations into the bath. One numerically inexpensive strategy to implement this idea is the stochastic Liouville equation (SLE)

$$\dot{\hat{\rho}} = -\mathrm{i}\left[\hat{H},\hat{\rho}\right] + \hat{L}_b\hat{\rho}\,, \tag{34}$$

where $\hat{L}_b$ represents the stochastic Markovian dynamics of the bath. The SLE is an equation for the field-free evolution of the joint system-bath density matrix and can be used to write a reduced equation of motion for the system density matrix which incorporates (perturbatively) the effects of the bath. This can, for example, be done at the level of the Lindblad equation [33, 34]. The model for the bath and system-bath coupling determines the form of $\hat{L}_b$. Examples are the n-state jump and Brownian oscillator models [1, 35].

Equations (32) and (33) give one procedure for obtaining the nth order signal and generates 2^n terms when the commutators with the initial density matrix are fully expanded. Equations (8) and (7) offer an alternative procedure which, upon expanding the time-ordered exponentials in the $\hat{U}^{(\dagger)}(t)$, generates $n+1$ terms at nth order. The latter procedure obviously involves less terms and it is often numerically preferable to propagate the wavefunction rather than the density matrix. On the other hand, only a density matrix based procedure can properly account for system-bath interactions and the dephasing-effects these cause. Moreover, the real-time interpulse delays appear more naturally in a density-matrix formulation. Equations (32) and (33) are therefore more expensive to implement but provide a more intuitive picture and are necessary when a proper account of system-bath dynamics is crucial [1].

As previously mentioned, the nth-order expansion of the density matrix as per (33) generates 2^n terms. Interpreting the resulting signal requires expanding the interaction Hamiltonian into its constituent terms (which are, in the rotating wave, ($\hat{\mathcal{E}}^\dagger\hat{V}$ and $\hat{\mathcal{E}}\hat{V}^\dagger$)). There are thus a total of 4^n terms which may be depicted diagrammatically (in the case of temporally overlapping fields, this is further complicated and leads to an additional factor of up to $(n+1)!$ representing permutations of the temporal order of field interactions). These diagrams represent different excitation and evolution pathways for the system density matrix and we refer to them as Liouville space pathways. This proliferation of terms (64 at 3rd order) with a variety of different resonances during different time periods makes the general problem of interpreting a signal quite difficult. Fortunately, the diagrams that contribute to an experimental signal can be reduced by various techniques (additionally, some diagrams vanish when the material begins the process in the ground state). Principally, experimentalists can exploit the phase-sensitivity of nonlinear signals to control the pathways taken by the system. Conceptually, the simplest method to accomplish this selectivity is to use a non-collinear beam geometry as depicted for the DQC technique in Fig. 3. In the large sample (relative to the light wavelength) limit, the spatial integrations give a delta function $\delta(-\mathbf{k}_4 \pm \mathbf{k}_3 \pm \mathbf{k}_2 \pm \mathbf{k}_1)$. This phase matching sets the directions along which a nonlinear signal may be detected and naturally separates the diagrams that contribute in particular directions [36]. Each wavevector $\mathbf{k}_4$ of the detected beam then selects a subset of diagrams as shown in Figs. 2 and 4. Alternatively, the same degree of control can be achieved in a collinear beam geometry by controlling the phases of the various beams. A linear combination of measurements with different phases can then yield the desired signal with $\phi_4 = \pm\phi_3 \pm \phi_2 \pm \phi_1$ corresponding to the equivalent spatial-phase selection in the non-collinear arrangement [37, 38]. This technique is known as phase cycling [39] and is always employed in multidimensional NMR because the wavevectors are close to zero in radio frequencies [40]. In the infrared, visible, and X-ray regimes, both phase matching and phase cycling protocols for pathway selection are possible depending on experimental convenience.

So far, we have been concerned with processes in which the system is initially in the ground state. In the X-ray regime, techniques employed can then study resonances of core excitations in relation to this ground state as well as the evolution of valence excitations along the ground state potential surface. This procedure may be generalized to account for a more general initial density matrix as may be obtained from previous excitation or pumping of the system. A complete account of these more general techniques involves explicit incorporation of the pumping process and results in higher-order correlation functions [18, 30]. Although more complicated, these techniques open up the possibility of studying excited state resonances (as well their correlations) and tracking the motion of valence excitations in the presence of core holes.

The present formalism may be further utilized in electronic spectroscopies such as time-resolved photoelectron and Auger electron spectroscopy (TRPES and AES, respectively). These techniques provide an alternative toolbox that complements and supplements the optical techniques discussed here. In particular, TRPES has simplified selection rules compared to optical detection schemes (any orbital may be ionized and the transition dipole to the continuum states does not depend much on the precise continuum state and may be approximated as flat in certain regions). The probabilities for excitation to various continuum states still depend sensitively on the final molecular electronic state and one can therefore use knowledge of the continuum as a probe [41, 42]. On the other hand, AES has entirely different selection rules, being based on a Coulomb matrix element (rather than a transition dipole) and has been used to track the radiationless decay of photoexcited molecules [43]. Despite these differences, a very similar formalism can be applied, the only differences being in the operators in the correlation functions. This then allows the use of the array of simulation procedures discussed for electronic spectroscopies and, in particular, gives a straightforward way to incorporate bath dynamics and dissipation effects without explicitly including corresponding degrees of freedom at the Hamiltonian level [44].

3 Quantum Chemistry Methods

Signal expressions in Sect. 2 require the calculation of core excited states and transition dipole moments. Here we review the quantum chemistry methods that can be used in their simulation and present a few examples.

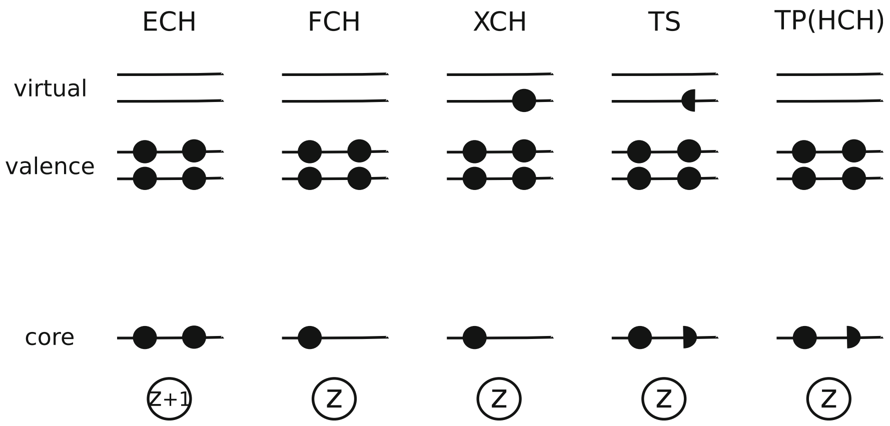

Fig. 7 Approximation schemes for core hole excitations. *ECH* equivalent core hole (Z+1) approximation, *FCH* full core hole approximation, *XCH* excited core hole approximation, *TS* transition state method, *TP*(*HCH*) transition potential method (half core hole approximation). *Full discs* represent electrons and *half discs* represent half electrons. *Numbers in circles* at the *bottom* represent nuclear charges, where Z is the number of electrons of the system

3.1 ΔSCF-Based Methods

3.1.1 Different Core Hole Approximations

An X-ray photon usually excites a core electron leaving a core hole in the system. Describing core holes properly is the primary task of resonant X-ray spectroscopy simulation. In Fig. 7 we show the most widely used approximation schemes for core holes [45]. The simplest is to represent a core hole as an additional nuclear charge.

This equivalent core hole (ECH) also known as (Z+1) approximation [46, 47] is adequate for deep core holes because for electrons in the exterior shells a deep core hole behaves as does a positive nuclear charge. It is simple to apply (no additional coding in standard quantum chemistry packages is necessary) and multiple core holes can also be easily represented by additional nuclear charges. However, it is a crude approximation which does not apply to shallow core holes. It further artificially changes the spin state of the system.

The ECH approximation was used in our early X-ray nonlinear spectroscopy simulations [48–52]. The photon echo signal $\mathbf{k}_{\mathrm{I}} = -\mathbf{k}_1 + \mathbf{k}_2 + \mathbf{k}_3$ of the para and ortho isomers of aminophenol was calculated in [48] (see Fig. 8). The second time delay t_2 is set to zero. The signals reveal the correlation between the O1s core excitations (Ω_1) and the N1s core excitations ($-\Omega_3$). The equivalent-core molecular orbitals corresponding to the three strong O1s XANES peaks (marked A, B, and C) are also shown. In a simple single orbital picture, orbital A is populated by the excited O1s electron in the lowest O1s excitation. The XANES signals are not sensitive to the corresponding core excited states, as can be seen from the top of Fig. 8. Although the orbitals corresponding to peak Bs of the two isomers look very

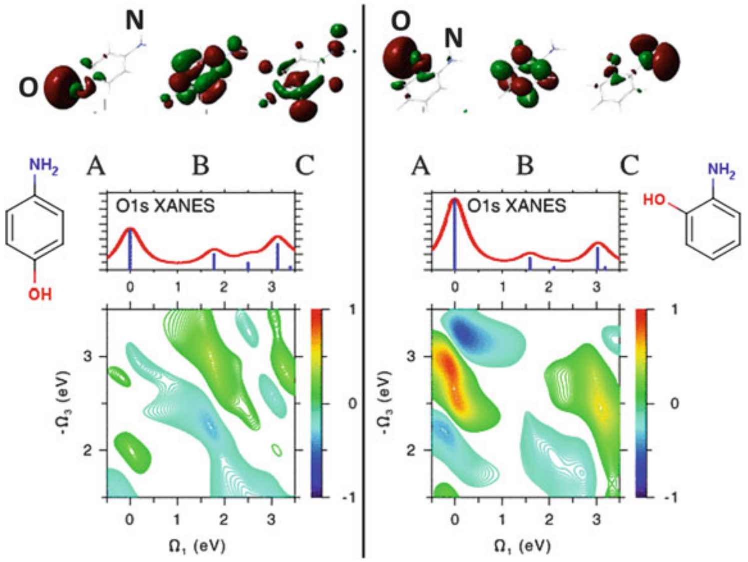

Fig. 8 Simulated O1s XANES and O1s/N1s photon echo crosspeak (at $t_2 = 0$) of para- (*left*) and ortho-aminophenol (*right*) with the ECH approximation. All single core excitation energies are shown as $\omega - \omega_j$, where ω_j is the lowest O1s or N1s excitation energy. Molecular orbitals populated by the promoted O1s electron for each of core-excited states contributing to the signal are show on the top. The positions of N and O atoms are labeled. Figure adapted from [48]

different, the two peak Bs are similar in energy and lineshape. This is because XANES only detects the local electronic structure of atoms. However, the photon echo signals show many differences. In the para isomer, the orbital corresponding to peak B is delocalized and extends from the O to N atom. So, the N1s and O1s core excitations corresponding to this orbital affect each other and generate a crosspeak (Fig. 8, left). However, in the ortho isomer, because the orbital corresponding to peak B vanishes in the surroundings of the N atom, the N1s and O1s core excitations corresponding to this orbital do not affect each other and thus we cannot see a crosspeak (Fig. 8, right). Although it is much stronger in O1s XANES of the para isomer, peak A contributes to a much weaker crosspeak than peak B. This is because the orbital corresponding to peak A in the para isomer is highly localized to the O atom and far away from the N atom. It is also understandable that peaks A and C produce much stronger crosspeaks of the ortho isomer than those of the para isomer because O and N atoms are closer in the ortho isomer. In all, photon echo signals carry detailed information about the wavefunctions of the core excited states involved in the experiment.

More than four decades ago Slater had proposed the transition state (TS) method for calculating core excitation energies. In this method the two orbitals involved in the transition are occupied by a half electron and solved self-consistently. The excitation energy is given by the difference between the two orbital energies [53, 54]. The excitation energy obtained in this way is accurate up to second order in the occupation number changes of the transition orbitals. The transition state method is convenient and sufficiently accurate in many cases, but it is not suitable for calculating many excited states because of the nonorthogonality and self-consistent field (SCF) collapse of the excited states. An alternative is the transition potential method (TP) [55, 56], in which the potential corresponding to the transition hole state (a half electron on the hole orbital; see Fig. 7) is used to produce a set of orthogonal excited states. The excitation energy is determined by the differences between transition potential orbital energies. TP is widely used in X-ray absorption spectroscopy simulation [57].

Similar core hole approximations have been proposed in solid state physics. The half core hole approximation (HCH; see Fig. 7) is similar to the transition potential method, and the full core hole approximation (FCH; see Fig. 7) is similar to the direct exchange method (STEX) [58–60] in quantum chemistry (this is explained in detail in the next subsection). In FCH, the impact of the excited electron on the core hole is neglected. If it is included, we obtain the excited core hole approximation (XCH) [61]. We have used XCH combined with TDDFT to simulate X-ray double-quantum-coherence spectroscopy [24].

3.1.2 Static Exchange Method (STEX)

In Hartree–Fock theory, occupied orbitals often provide an adequate description for the ground state but virtual orbitals give a less satisfactory description of the excited states. Hunt and Goddard proposed to use the Hartree–Fock virtual orbitals of an $(N-1)$-electron system to represent the excited state orbitals of the corresponding N-electron system. This is known as the improved virtual orbital or $N-1$ approximation [58]. In STEX, the occupied orbitals of an N-electron core-excited system are also represented by the occupied orbitals of the $(N-1)$-electron ionic system with the corresponding core hole. A core electron is removed and a restricted open-shell Hartree–Fock (ROHF) calculation is carried out to obtain the occupied orbitals of the ionic system. A major difficulty is that the electrons often collapse to fill the core hole during the SCF calculation. This can be remedied by the maximum overlap method (MOM) [62], which is explained in detail in the following sections. However, even with MOM, the SCF iteration may converge to a wrong electronic state or even may not converge at all. To guide the SCF iteration towards the designated ionic state, a careful choice of the other SCF convergence parameters such as the damping and level-shifting factors [63–65] and many trial-and-error calculations with different initial guesses are usually necessary. New convergence schemes are required to improve the SCF calculations of such ionic states.

Once the occupied orbitals of the ionic state are obtained, a single electron is placed in a virtual orbital and the resulting open-shell singlet reads

$$\left|\Psi_{j,l}^{N}\right\rangle = \frac{1}{\sqrt{2}}\left(\hat{a}_{l\alpha}^{\dagger}\left|\Psi_{j\alpha}^{N-1}\right\rangle + \hat{a}_{l\beta}^{\dagger}\left|\Psi_{j\beta}^{N-1}\right\rangle\right), \tag{35}$$

where $\left|\Psi_{j\sigma}^{N-1}\right\rangle \equiv \hat{a}_{j\sigma}\left|\Psi_{\text{ref}}^{N}\right\rangle$ and $\sigma = \alpha, \beta$ are spin states, j is the core orbital index, l is the virtual orbital index, $\left|\Psi_{\text{ref}}^{N}\right\rangle$ is the N-electron neutral reference state, and $\hat{a}$ and $\hat{a}^{\dagger}$ are annihilation and creation operators, respectively. The excited orbitals within the N$-$1 approximation satisfy the eigenvalue equations:

$$\hat{F}_{\text{STEX}}^{j}\psi_{l}^{j} = \varepsilon_{l}^{j}\psi_{l}^{j}, \tag{36}$$

where ψ_{l}^{j} is the exited orbital and ε_{l}^{j} is the corresponding orbital energy. The STEX Fock operator

$$\hat{F}_{\text{STEX}}^{j} = \hat{h} + \sum_{i \neq j}^{\text{occ}}\left(2\hat{J}_{i} - \hat{K}_{i}\right) + \hat{J}_{j} + \hat{K}_{j}, \tag{37}$$

is constructed using the orbitals of the (N$-$1)-electron ionic system. $\hat{h}$ is the single particle Hamiltonian (kinetic plus nuclear attraction part) and $\hat{J}_{j}$ and $\hat{K}_{j}$ are the Coulomb and exchange operators for the core orbital j, respectively:

$$\begin{aligned} \hat{J}_{j}(1) &= \int \mathrm{d}\mathbf{r}_{2}\psi_{j}^{*}(2)r_{12}^{-1}\psi_{j}(2), \\ \hat{K}_{j}(1)\psi_{l}(1) &= \left[\int \mathrm{d}\mathbf{r}_{2}\psi_{j}^{*}(2)r_{12}^{-1}\psi_{l}(2)\right]\psi_{j}(1). \end{aligned} \tag{38}$$

The eigenvectors of $\hat{F}_{\text{STEX}}^{j}$ are not orthogonal to the occupied orbitals of the (N$-$1)-electron ionic system, and an orthogonalization procedure is necessary. We can use the projection operator

$$\hat{P}^{j} = \sum_{k \neq j}^{\text{occ}}\left|\psi_{k}^{j}\right\rangle\left\langle\psi_{k}^{j}\right|, \tag{39}$$

to project out all occupied orbitals of the (N$-$1)-electron ionic system and solve the projected STEX equation

$$\left(\hat{1} - \hat{P}^{j}\right)\hat{F}_{\text{STEX}}^{j}\left(\hat{1} - \hat{P}^{j}\right)\psi_{l}^{j} = \varepsilon_{l}^{j}\psi_{l}^{j}. \tag{40}$$

The solutions of this equation should serve as a good approximation to the excited orbitals. The core excitation energy is finally given by

$$\omega_{j,l} = \mathrm{IP}_j + \varepsilon_{j,l}, \tag{41}$$

where IP_j is the ionization potential of the core electron j (determined from the energy differences of the (N−1)-electron ionic system and the N-electron neutral system).

STEX is a single excitation theory in which particle and hole are independent. Channel interaction can be included by diagonalizing the configuration interaction matrix in the space of linear combinations of different single excitation channels. This extension is known as the STEX-CIS (configuration interaction singles) method. Double excitations can also be treated with a STEX Hamiltonian based on the (N−2)-electron ionic system, but the SCF convergence problem is more serious and the spin coupling schemes are complicated [66].

State-to-state transition dipoles are necessary in order to simulate the nonlinear X-ray spectroscopy signals. Because the STEX orbitals are not orthogonal to the MOs of the N-electron system, Löwdin's rule [67] may be used for calculating the transition dipoles between two states with nonorthogonal single particle orbitals. The transition dipoles for single excitations are

$$\left\langle \Psi_{\mathrm{A}} \middle| \hat{d} \middle| \Psi_{\mathrm{B}} \right\rangle = \sum_{m,n}^{N_{\text{config.}}} a_m b_n \sum_{i,j} (-1)^{i+j} d_{ij}^{mn} \mathrm{Minor}(\mathbf{S}^{mn})_{ij}, \tag{42}$$

where $\Psi_{\mathrm{A,B}}$ are two excited states with nonorthogonal single particle orbitals, $\hat{d}$ is the transition dipole operator, and a_m and b_n are configuration interaction (CI) coefficients for different single excitation configurations (m and n) of state A and B, respectively.

$$d_{ij}^{mn} = \sum_{p,q} c_{ip,m,\mathrm{A}}^{*} c_{jq,n,\mathrm{B}} \int \phi_p^{*} \hat{d} \, \phi_q \mathrm{d}\tau, \tag{43}$$

is the transition dipole matrix between the single excitation configurations m and n, $c_{ip,m,\mathrm{A}}$ and $c_{j,q,n,\mathrm{B}}$ are MO coefficients for the configurations m and n of state A and B, respectively, and

$$S_{ij}^{mn} = \sum_{k,l} c_{ik,m,\mathrm{A}}^{*} c_{jl,n,\mathrm{B}} \int \phi_i^{*} \phi_j \mathrm{d}\tau, \tag{44}$$

is the overlap matrix between the MOs of the configurations m and n of state A and B, respectively. $\phi_{i,j}$ in (43) and (44) are basis functions and i, j, p, q, k, l are indices for these basis functions. Minor $(S^{mn})_{ij}$ denotes the (i, j) minor of the matrix $\mathbf{S}^{mn}$.

We next present 1D and 2D SXRS signals calculated using STEX [29, 68]. Figure 9 shows the 2D-SXRS spectrum of *N*-methylacetamide (NMA) with the OOO (O1s pump with two O1s probes) pulse sequence, together with 1D projections

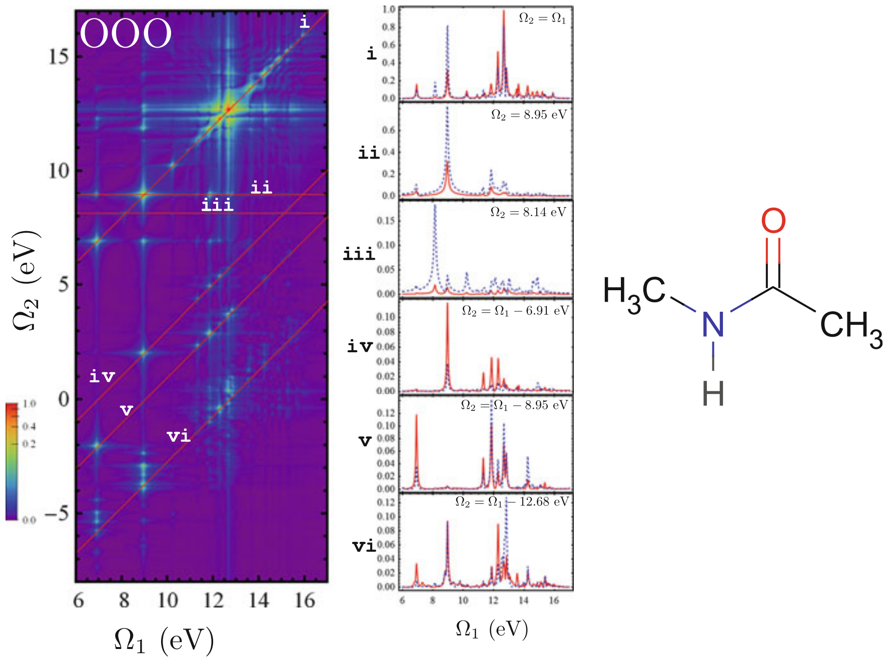

Fig. 9 The 2D-SXRS signal $S_{\mathrm{SXRS}}(\Omega_1, \Omega_2)$ and its 1D traces of NMA (*right*) from STEX calculations. *Left*: the OOO spectrum. All these pulses are resonant with the O K-edge. *Middle*: *horizontal* and *diagonal slices* of the 2D spectrum on the *left* (*in red*) plotted together with the corresponding traces from the corresponding OON (*dashed*, *blue*) to highlight the effect of changing the probe pulse in the three-pulse sequence. Figure adapted from [29]

along several horizontal and diagonal traces. We also show the corresponding traces from the OON 2D-SXRS signal in blue dashed lines for comparison. The only difference between the two types of 1D signals are the third pulse. Peaks along the diagonal line ($\Omega_2 = \Omega_1$, **i** in Fig. 9) resemble those from the 1D-SXRS spectrum of the same molecule [29]. Peaks along the horizontal lines drawn at the representative valence excitation energies ($\Omega_2 = 8.95$, 8.14 eV, **ii** and **iii** in Fig. 9) reveal the interference of the two Liouville space quantum pathways represented by diagrams a and d in Fig. 6, and peaks along the diagonal lines shifted with representative valence excitation energies ($\Omega_2 = \Omega_1 - 6.91$, 8.95, 12.68 eV, **vi**, **v**, and **vi** in Fig. 9) reveal the interference of the other two quantum pathways represented by diagrams b and c in Fig. 6. Figure 9 illustrates that multidimensional SXRS signals reveal couplings of different valence excitations, and interferences of quantum pathways.

Comparison of STEX with another method for calculating core excited states, the restricted excitation window time-dependent density functional theory (REW-TDDFT), was given in [69]. Core excitation energies from both methods must be shifted to match experiment. Because of the inclusion of core orbital relaxation, the shifts of STEX core excitation energies (<10 eV) are usually smaller than those of TDDFT (>10 eV). However, being an independent particle and hole theory, STEX cannot account for core hole mixing in X-ray spectroscopy, whereas REW-TDDFT can. The SCF calculation of a core ionized state is often tricky. Convergence is not guaranteed. In addition, because the STEX equation (40) is not solved self-consistently, the occupied and virtual STEX orbitals are not variational for the total energy. Evaluating core excited state properties, e.g., electron density, thus become complicated [70]. State-to-state transition dipole calculations are expensive.

3.1.3 ΔSCF-DFT Method

A straightforward extension of DFT to excited states (including core excitations) is achieved by employing non-Aufbau occupations of Kohn–Sham orbitals and running SCF calculations to obtain the target excited states as is done in ground state calculations [71–74]. This is known as the ΔSCF-DFT (or simply the ΔSCF) method. The biggest difficulty is the collapse to the lower energy states below the excited state during the SCF iterations. Special care must be taken to keep the electrons in the designated excited configuration. The maximum overlap method (MOM) [62] is widely used to avoid SCF collapse. Here, the new occupied orbitals in the current SCF cycle are chosen as the orbitals which have a maximum overlap with the occupied orbitals in the last cycle. The orbital overlap matrix is given by

$$\mathbf{O} = \left(\mathbf{C}^{n-1}\right)^{\dagger}\mathbf{S}\mathbf{C}^{n}, \tag{45}$$

where $\mathbf{C}^{n-1}$ and $\mathbf{C}^{n}$ are the molecular orbital coefficient matrices in the last and current SCF iteration, respectively, $\mathbf{S}$ is the overlap matrix of basis functions, and the matrix element O_{ij} represents the overlap between the ith old orbital and the jth new orbital. The projection of the jth new orbital onto the old occupied orbital space may be defined as

$$P_j = \sum_i^{\text{occ}} O_{ij} = \sum_l^{\text{occ}} \left[\sum_k^{\text{occ}} \left(\sum_i^{\text{occ}} C_{ik}^{n-1}\right) S_{kl}\right] C_{lj}^{n}. \tag{46}$$

The orbitals with the largest P_js are chosen as the new occupied orbitals. In some cases (46) is not robust when selecting new occupied orbitals. Alternative projections such as

$$P_j = \sum_i^{\text{occ}} \left|O_{ij}\right|, \tag{47}$$

and

$$P_j = \sum_{i}^{\text{occ}} |O_{ij}|^2, \tag{48}$$

have been implemented in the quantum chemistry packages Q-CHEM [75] and GAMESS [76]. The same projection scheme as in (48) was also proposed by other authors very recently [77]. When all O_{ij}s do not have the same sign, or a number of orbitals are nearly degenerate during the SCF iteration, (48) is believed to perform better than (47) [77].

Unlike STEX, a spin-unrestricted scheme is employed in ΔSCF-DFT. Thus for a system with a closed shell ground state, ΔSCF-DFT usually gives a broken-symmetry spin state which is a mixture of a singlet and a triplet state. The singlet excitation energy can be obtained through the spin-purification formula [72]

$$E_{\mathrm{S}} = 2E_{\mathrm{BS}} - E_{\mathrm{T}}, \tag{49}$$

where E_{S} is the energy of the open shell singlet, E_{BS} is the spin broken-symmetry state energy, and E_{T} is the triplet energy from a separated ΔSCF-DFT calculation. Spin-purification is necessary in valence excitation calculations [78, 79] but is less important in core excitations, where $E_{\mathrm{BS}} \approx E_{\mathrm{T}}$ so that $E_{\mathrm{S}} \approx E_{\mathrm{BS}}$.

ΔSCF-DFT can be easily extended to calculate various excited state properties other than the excitation energy [79]. It also includes orbital relaxation upon excitation, which is neglected in TDDFT. Note that the (N−1) approximation in STEX may not be necessary for ΔSCF-DFT because the DFT virtual orbitals experience the same potential as do the occupied orbitals. However, it has some drawbacks. First, ΔSCF-DFT is a state-specific approach; one should calculate the excited states one by one. This makes it unsuitable for broadband spectroscopy simulations, where many excited states are needed. Second, it only gives excited states which can be well described by a single determinant. Excited states with strong configuration interactions are missed. Third, excited states from separated ΔSCF-DFT calculations are not orthogonal, and there is no unique way to enforce the orthogonality requirement. Finally, it is an open question how to run variational DFT calculations of excited states because there is no Hohenberg–Kohn theorem for a generic excited state [80]. Despite its drawbacks, ΔSCF-DFT has been revived recently in charge-transfer excitation [81], Rydberg excitation [82], and excited state potential energy surface calculations [83], and looks very promising in the X-ray regime.

3.2 TDDFT Techniques

As explained in the introduction section, the discussions in this section are based on adiabatic TDDFT. Although similar formulation for time-dependent Hartree-Fock (TDHF) theory had existed for more than two decades [84], the time-domain extension of DFT was not possible until Runge and Gross established the one-to-one mapping of electron density and time-varying external potential [85]. There are two categories for applying TDDFT to calculate excited state properties: the response theory based on perturbation in the frequency domain and the direct real-time propagation methods in the time domain. The frequency-domain formalism of TDDFT, which is based on linear response theory, became popular after Casida proposed a density matrix response equation which is very similar to the renowned random phase approximation (RPA) equation [86]. The Casida equation can be derived by solving the equation of motion (EOM) of the single electron reduced density matrix to the first order of external perturbation in the frequency domain. Similar expressions have been obtained for TDHF in the collective electronic oscillator (CEO) method [87–89]. Nonlinear response functions of the system can be calculated in CEO by applying high order perturbation theory [89].

Another way to obtain excited state properties is to solve the EOM of single-electron reduced density matrix by direct propagation in the time domain. Time-dependent properties of the system induced by the time-dependent external perturbation can be calculated directly and Fourier transform can recover the excited state information in the frequency domain.

In this section, we start with the linear-response formalism of Casida, and then present a specific variant of linear-response TDDFT applied to core excited state (restricted excitation window time-dependent density functional theory, REW-TDDFT). Moreover, high order perturbation theory methods for nonlinear response properties of the system are introduced and finally the real-time propagation methods are discussed. It should be noted that the response and real-time propagation methods are very general and not restricted to DFT/TDDFT, but we focus on the DFT/TDDFT formalisms of these methods in this chapter.

3.2.1 Linear Response Theory

The Casida equation can be derived by calculating the linear response of the density matrix or through an EOM approach. One may start with the EOM of the one-particle transition density matrix $P_I = |I\rangle\langle 0|$:

$$\left[\hat{H}, P_I\right] = \mathrm{i}\frac{\partial P_I}{\partial t} = \omega P_I, \tag{50}$$

where $|I\rangle$ and $|0\rangle$ are the Ith excited state and ground state, respectively, $\hat{H}$ is the Hamiltonian of the system, and ω is the excitation energy. Considering the idempotency property of density matrix, the transition density matrix can be expanded as

$$P_I = \sum_{i,a} \left(X_{ia} \hat{a}^{\dagger} \hat{i} + Y_{ia} \hat{i}^{\dagger} \hat{a} \right), \tag{51}$$

where X_{ia} and Y_{ia} are one-particle/one-hole (1p1h) excitation and de-excitation amplitudes, respectively, and *i, a* represent an occupied and virtual orbital, respectively. Substituting (51) into (50), after some algebraic manipulations, one can obtain the Casida equation:

$$\begin{pmatrix} \mathbf{A} & \mathbf{B} \\ \mathbf{B}^* & \mathbf{A}^* \end{pmatrix} \begin{pmatrix} \mathbf{X} \\ \mathbf{Y} \end{pmatrix} = \omega \begin{pmatrix} \mathbf{1} & \mathbf{0} \\ \mathbf{0} & -\mathbf{1} \end{pmatrix} \begin{pmatrix} \mathbf{X} \\ \mathbf{Y} \end{pmatrix}, \tag{52}$$

where

$$\begin{aligned} A_{ia\sigma,\, jb\tau} &= \delta_{ij}\delta_{ab}\delta_{\sigma\tau}(\varepsilon_{a\sigma} - \varepsilon_{i\tau}) + K_{ia\sigma,\, jb\tau}, \\ B_{ia\sigma,\, jb\tau} &= K_{ia\sigma, b j\tau}, \\ K_{ia\sigma,\, jb\tau} &= \left(i_\sigma a_\sigma \middle| j_\tau b_\tau \right) + \left(i_\sigma a_\sigma \middle| f_{xc} \middle| j_\tau b_\tau \right), \end{aligned} \tag{53}$$

and

$$\begin{aligned} \left(i_\sigma a_\sigma \middle| j_\tau b_\tau \right) &= \int\int \psi_{i\sigma}(\mathbf{r})^* \psi_{a\sigma}(\mathbf{r}) \frac{1}{|\mathbf{r} - \mathbf{r}'|} \psi_{j\tau}(\mathbf{r}')^* \psi_{b\tau}(\mathbf{r}') \mathrm{d}\mathbf{r}\mathrm{d}\mathbf{r}', \\ \left(i_\sigma a_\sigma \middle| f_{xc} \middle| j_\tau b_\tau \right) &= \int\int \psi_{i\sigma}(\mathbf{r})^* \psi_{a\sigma}(\mathbf{r}) \frac{\delta^2 E_{\mathrm{XC}}}{\delta\rho_\sigma(\mathbf{r})\delta\rho_\tau(\mathbf{r}')} \psi_{j\tau}(\mathbf{r}')^* \psi_{b\tau}(\mathbf{r}') \mathrm{d}\mathbf{r}\mathrm{d}\mathbf{r}'. \end{aligned} \tag{54}$$

Here *i, j* and *a, b* represent occupied and virtual orbitals, respectively, σ, τ are spin indices, ε is the orbital energy, and f_{xc} is the exchange-correlation kernel which is expressed as the second-order functional derivative of the exchange-correlation energy with respect to electron density (54). In (52), **X** and **Y** should be considered as column vectors. Alternatively, it is possible to derive these equations for the reduced single electron density matrix. This has been done in the CEO method [87–89] for both TDHF [89] rather than TDDFT [90, 91].

Because of its balance of accuracy and computational cost, and its robustness and black-box character, linear-response TDDFT has become the method of choice for computing excited states, including core excited states. We have also based our nonlinear X-ray spectroscopy simulation work on TDDFT [24, 69, 92, 93]. Unlike ΔSCF-DFT, linear-response TDDFT does not target a single excited state. Only ground state orbitals are necessary in the calculation, so that a manifold of excited states is obtained in one shot. However, linear-response TDDFT also has its limitations. Usually based on a single-referenced Kohn–Sham state, linear-response TDDFT cannot handle excited states calculations for a ground state with a heavy multiconfigurational character. Orbital relaxation for different excited states is missed. Approximate energy functionals do not have proper long-range asymptotic behavior, and thus linear-response TDDFT has difficulties in handling charge-transfer excited states [94] and Rydberg states. The same limitation applies to core excited states [14]. The long-range corrected density functionals are discussed in Sect. 4.1. In addition, within the adiabatic (frequency-independent) exchange-correlation kernels, linear-response TDDFT cannot properly describe double excitations [95]. This is a major obstacle for simulating nonlinear spectroscopy experiments, which directly access double or multiple excited states. Double excitations and frequency-dependent exchange-correlation kernels are discussed in Sect. 4.3.

3.2.2 Restricted Excitation Window TDDFT

Calculating core excited states directly using (52) is prohibitively expensive because there are numerous low energy excited states below the target high energy core excited state. Any bottom-up matrix eigenvalue numerical algorithm becomes very tedious. This difficulty can be circumvented by allowing electrons to move only between a certain set of relevant occupied and virtual orbitals. This is the basis for the restricted excitation window (REW) or restricted excitation channel approach. This method was proposed by Stener and co-workers [96], and followed by other authors [97–100]. One can select the orbitals in the restricted excitation window by their orbital indices or energies. In the first scheme all molecular orbitals (MO) are examined and then the relevant orbitals (e.g., the MOs dominated by the target oxygen 1s atomic orbitals) are selected out. Alternatively, an orbital energy or energy difference cutoff is used to filter out all relevant orbitals or transition orbital pairs. Orbital index selection is intuitive but becomes cumbersome if there are too many relevant orbitals. The orbital energy (energy difference) selection scheme is convenient for building a large REW. If there are multiple target atoms of the same type in the molecule, the target MOs would become degenerate or near-degenerate. The orbital index selection scheme can explore the contribution of a single target atom to the core excitation and the spectroscopy signal, whereas the orbital energy selection scheme can study hole-mixing effects. Another method with the same effect of building a REW is to shift the core excitation energy difference. This was proposed by Schmidt et al. [101] very recently and is very similar to Stener and co-workers' early implementation in the ADF package. After the REW is determined, trial excitation vectors are prepared in this REW and a Davidson-type iterative solver [102] is usually employed to find the relevant matrix eigenvalues and eigenvectors. REW-TDDFT has been implemented in standard quantum chemistry packages such as ADF [103], Q-Chem [104], ORCA [105], NWChem [106], and Gaussian [107].

Minimum inputs (relevant orbitals, number of excited states) are needed for running a REW-TDDFT calculation. It is almost black-box and robust and can handle all types of excited states with deep as well as shallow holes. It is a response method and avoids the state-specific SCF convergence problem. Hole-mixing can be observed, which is not possible with STEX or ΔSCF-DFT. Electron correlation can be considered in the exchange-correlation functional. Moreover, REW-TDDFT can easily calculate many core excited states. If unrelaxed CIS-type wave functions (Tamm–Dancoff approximation, TDA) are used to represent the excited states, the state-to-state transition dipoles in REW-TDDFT reduce to sums of transition dipoles between certain MOs because all MOs are mutually orthogonal. This drastically reduces the computational cost compared to (42).

In order to calculate nonlinear X-ray spectroscopy signals, we developed a computational approach based on REW-TDDFT implemented in the quantum chemistry package NWChem. In a series of publications [6, 69, 108], we had extended the conventional optical Raman spectroscopy techniques into the X-ray regime. One- and two-dimensional stimulated X-ray Raman spectroscopy (1D- and 2D-SXRS) signals of the small amino acid cysteine were simulated and compared to the conventional resonant inelastic X-ray scattering (RIXS) signals. Compared to RIXS, which is a frequency domain technique, multi-color time domain SXRS provide a better window to the electronic coupling dynamics in a molecule. We also calculate the X-ray four-wave mixing $\mathbf{k}_{\mathrm{I}} = -\mathbf{k}_1 + \mathbf{k}_2 + \mathbf{k}_3$ and $\mathbf{k}_{\mathrm{II}} = \mathbf{k}_1 - \mathbf{k}_2 + \mathbf{k}_3$ signals. To compare these with the SXRS signals, we took the time delay t_2 between $\mathbf{k}_2$ and $\mathbf{k}_3$ longer than the lifetimes (<10 fs) of the core excited states in this system, so that only the ground-state-bleach (GSB) terms in the signals survive. $\mathbf{k}_{\mathrm{I,II}}$ signals have three frequency variables Ω_j ($j = 1, 2, 3$), where Ω_1 and Ω_3 correspond to core excitations and Ω_2 corresponds to valence excitations. We can cut some slices of these 3D signals to interpret them. In Fig. 10 we show slices of the two-color $\mathbf{k}_{\mathrm{II}}$ (OOSS) signal with constant Ω_2 at different peaks in the two-color integrated two-pulse SXRS signal. These plots show the correlation between core excitations at different places in the molecule. We can find both the valence excitations at $\Omega_2 = 6.6$ and 8.9 eV are coupled to the S1s core excitation at $\Omega_3 = 2475.5$ eV, but they are coupled to different O1s core excitations at $\Omega_1 = 532.2$ and 536.1 eV, respectively. The valence excitation at $\Omega_2 = 11.4$ is coupled to S1s core excitation with higher energies. Moreover, the frequency dispersed two-pulse SXRS signals can give the same information about electron correlation as do projected photon echo signals [108], whereas the SXRS experiment is much simpler than the photon echo. However, photo echo experiments have more control variables and can reveal the correlation between core excitations directly (see Fig. 10), although SXRS can only infer them through valence excitations.

The same simulation approach was applied to porphyrin dimers. Multiporphyrin systems are good candidates for artificial photosynthesis or molecular electronics applications, so understanding the detailed excitation energy transfer (EET) mechanisms in these systems becomes very important. Simulated SXRS signals of various porphyrin heterodimer systems were obtained [92, 93] using REW-TDDFT. In Fig. 11 we show the time-domain 1D SXRS signals and the corresponding evolving electron and hole densities in the Zn and Ni porphyrin heterodimer (structure shown on the top of Fig. 11). We found an almost constant $\pi/2$ phase difference between the one-color Zn2p pump and Zn2p probe (Zn2p/Zn2p) signal and the two-color Zn2p pump and Ni2p probe (Zn2p/Ni2p) signal ((c) at bottom left in Fig. 11). Because the SXRS signal can be considered as an overlap between the time-dependent doorway wavepacket created by the pump pulse and the time-independent window wavepacket created by the probe pulse [92], this phase difference corresponds to a back-and-forth motion of the doorway wavepacket.

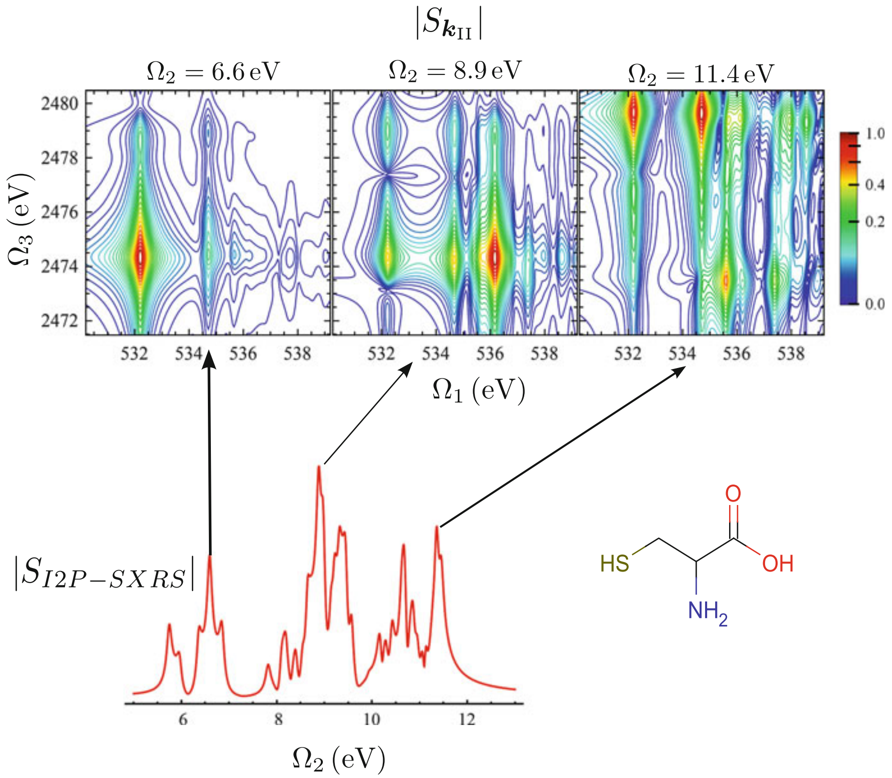

Fig. 10 Four-wave mixing and I2P-SXRS signals of cysteine (structure shown on the *bottom right*) from REW-TDDFT calculations. *Top*: constatnt-Ω_2 slices of the 3D $\mathbf{k}_{\mathrm{II}}$ signal $S_{\mathbf{k}_{\mathrm{II}}}$ (Ω_1, $\Omega_2 = 6.6$, 8.9, 11.4 eV, Ω_3) using an OOSS pulse sequence with *xxxx* polarization. *Bottom left*: the integrated two-pulse SXRS signal using an OS pulse sequence with *xx* polarization. Figure adapted from [108]

Correlation between the motion of the doorway wavepacket and the fluctuations of the SXRS signal profiles can be established. The time-domain signals provide a real-time image of EET in the system, which is not possible for time-resolved fluorescence anisotropy decay studies. SXRS could become a powerful tool in revealing EET mechanisms in molecular systems. Further geometrical and structural factors that control EET in a series of porphyrin heterodimer systems were studied in [93].

In another SXRS simulation study we investigated long-range electron transfer (ET) in the small redox protein azurin [109]. Borrowing the ET kinetic parameters from time-resolved infrared (IR) and optical measurements, time-resolved SXRS signals at the electron donor, hopping intermediate and electron acceptor were simulated with REW-TDDFT. We found that the SXRS signals depend sensitively on the local electronic structure changes around the excited atoms, and could serve as an excellent indicator for detecting electron transfer dynamics. The atomic

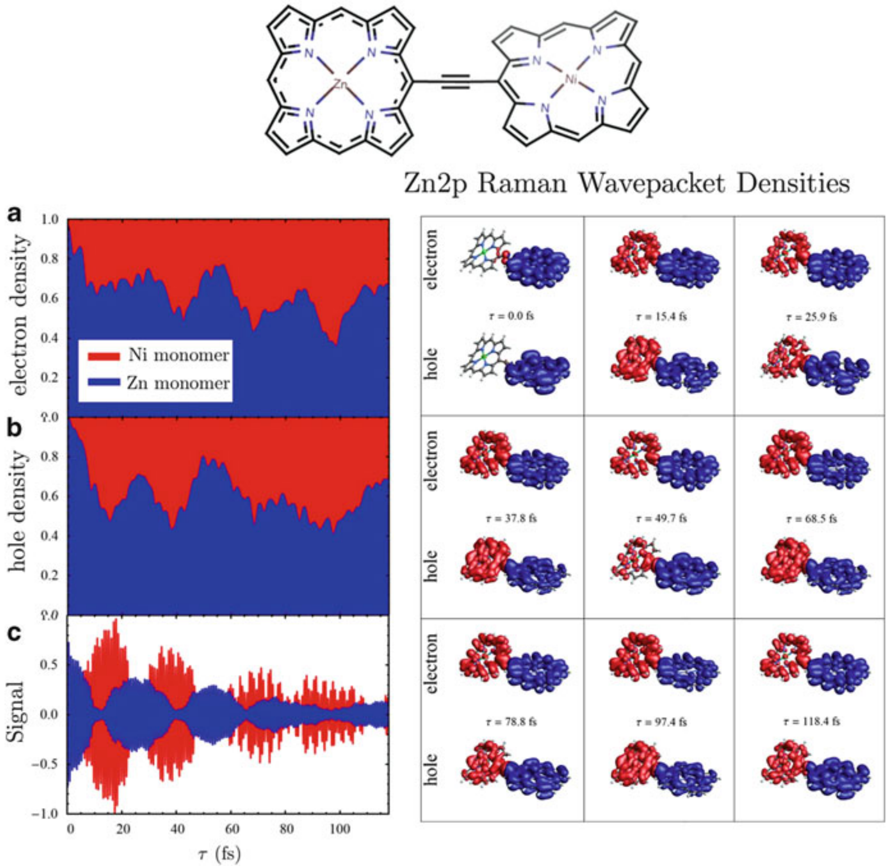

Fig. 11 Time-domain 1D SXRS signals that reveal excitation energy transfer in porphyrin heterodimers from REW-TDDFT calculations. *Top*: the molecular structure of the Zn-Ni porphyrin heterodimer studied. *Bottom left*: (**a**, **b**) Spatially integrated hole and electron densities on the Ni (*red*) and Zn monomer (*blue*). (**c**) The time-resolved integrated two-pulse SXRS signals of the porphyrin dimer between 0 and 120 fs. The single color Zn2p/Zn2p signal is in *blue* and the two-color Zn2p/Ni2p signal is in *red*. *Bottom right*: electron and hole densities of the Zn2p valence superposition state prepared by SXRS for various times after excitation. The isosurfaces are colored according to which monomer they reside on, *red* for Ni and *blue* for Zn. Figure adapted from [92]

pinpoint spatial accuracy also makes SXRS a convenient tool in studying different ET pathways. Such measurements are difficult for conventional IR or optical techniques. SXRS should complement linear transient X-ray absorption [110] in studying ultrafast ET molecular processes.

3.2.3 Perturbation Methods for High Order Responses

Nonlinear optical response properties can be obtained by going beyond the first order of perturbation in equations similar to (50). Response equation (Sternheimer equation) of wave functions instead of density matrix can also been considered [111]. Following the standard time-dependent perturbation theory, Orr and Ward derived the sum-over-state (SOS) expressions of the nonlinear optical polarizations four decades ago [112]. The SOS expressions are general and excited states from any level of theory could be used. Much TDDFT work has been done along these lines [91, 111, 113–121]. A weak time-dependent external electric field is introduced as a perturbation to the original Kohn–Sham system. Then the coupled-perturbed TDDFT equations, which are similar to the coupled-perturbed Kohn-Sham equations in DFT geometry optimization calculations, are solved at different orders of the perturbation and nonlinear response properties are evaluated by perturbed wave function or density matrix. Using the $2n+1$ rule [122], third order response properties can be obtained through the first perturbed wave function. These approaches can also be used to calculate the nonlinear response to X-ray pulses.

The complex polarization propagator (CPP) method for XANES simulation was proposed by Norman and coworkers [123–125]. They first parameterized the orbital rotation during time evolution, then started from an EOM of the state-transfer operators with external perturbations and a phenomenological damping term. With this damping term, decay of excited states can be considered in the now-complex response functions and resonance divergences are eliminated. With perturbation techniques, the EOM can be solved at different orders of perturbation and the corresponding response properties can be calculated. For the linear polarizability, one has

$$\alpha_{ij}(\omega) = -\mu_i^{[1]\dagger}\left[E^{[2]} - (\omega + \mathrm{i}\gamma)S^{[2]}\right]^{-1}\mu_j^{[1]}, \tag{55}$$

where $i, j = x, y, z$ are coordinate axis indices, $\mu_{i,j}^{[1]}$ is the electric-dipole property gradient along the coordinate axis $i, j,$ respectively, $E^{[2]}$ is the electronic Hessian, γ is the phenomenological damping parameter, and $S^{[2]}$ is the overlap matrix [125]. The CPP method is general and when DFT orbitals are used, it gives excellent XANES spectra of large molecules such as copper phthalocyanine [126]. A constant shift (usually it is a blue shift) is still needed to match the calculated XANES to experiment. The constant shift depends on the system and functional used, e.g., for the water molecule the shifts are 15.15 and 4.0 eV for the CAM-B3LYP and LB94 functional, respectively [125]. Nevertheless, third order electronic Hessian is needed to calculate second-order response, making the calculation quite involved.

Coupled-perturbed TDDFT results in SOS expressions of nonlinear response functions [127], which become increasingly more complex for higher order response. High order functional derivatives of the exchange-correlation energy functional are necessary [111, 121]. Because many excited states and orbitals, including virtual orbitals, are involved, high order perturbation methods are unsuitable for simulations of large systems because of their unfavorable computational scaling.

3.2.4 Real-Time Propagation Methods

In the frequency domain, each relevant excited state must be explicitly calculated when the SOS expressions of nonlinear X-ray spectroscopy signals are employed. The calculation becomes very expensive when many excited states contribute to the signals. In recent attosecond laser spectroscopy experiments [128–140], the orbital relaxation as well as the nonadiabatic dynamics with significant geometry changes involve many excited states. Real-time methods are then preferable.

In real-time time-dependent density functional theory (RT-TDDFT), rather than solving for eigenstates, the wave function or the one-electron reduced density matrix[1] is directly propagated in the time domain. Spectroscopic signals can be extracted from Fourier transform of time-dependent system properties such as the polarization of the molecule driven by the external electric field. The entire spectrum can be obtained at once and direct calculation of specific excited states is avoided.

The Liouville–von Neumann equation of motion of the reduced single electron density matrix $\boldsymbol{\sigma}(t)$ is [141]

$$\mathrm{i}\frac{\partial \boldsymbol{\sigma}(t)}{\partial t} = [\mathbf{F}(t), \boldsymbol{\sigma}(t)], \tag{56}$$

where $\mathbf{F}(t)$ is the Fock matrix in DFT. The time-dependent electric dipole moment $\mu(t)$, can be calculated by

$$\mu(t) = -\mathrm{Tr}[\boldsymbol{\mu}\boldsymbol{\sigma}(t)]. \tag{57}$$

Other time-dependent single electron molecular properties can be obtained in a similar way. The unitary time evolution operator $U(t_2, t_1)$ propagates the many-electron wave function $\psi(t_1)$ at time t_1 to the wave function $\psi(t_2)$ at time t_2:

$$\psi(t_2) = \hat{U}(t_2, t_1)\psi(t_1). \tag{58}$$

For the density matrix propagation, we have

---

[1] Throughout this chapter we mean one-electron reduced density matrix for density matrix unless explicitly explained with another meaning.

$$\boldsymbol{\sigma}(t+\Delta t) = \mathbf{U}(t+\Delta t, t)\boldsymbol{\sigma}(t)\mathbf{U}^{\dagger}(t+\Delta t, t), \tag{59}$$

where t is a time point and Δt is a time delay. Formally, the time evolution operator can be expanded in time-ordered products:

$$\begin{aligned}\mathbf{U}(t+\Delta t, t) &= \hat{T}\exp\left(-\mathrm{i}\int_{t}^{t+\Delta t}\hat{F}(\tau)\mathrm{d}\tau\right)\\ &= \sum_{n=0}^{\infty}\frac{(-\mathrm{i})^{n}}{n!}\int_{t}^{t+\Delta t}\mathrm{d}\tau_1\int_{t}^{t+\Delta t}\mathrm{d}\tau_2\cdots\int_{t}^{t+\Delta t}\mathrm{d}\tau_n\hat{T}\left\{\hat{F}(\tau_1)\hat{F}(\tau_2)\cdots\hat{F}(\tau_n)\right\},\end{aligned} \tag{60}$$

where $\hat{T}$ is the time-ordering operator [1] and $\hat{F}$ is the Fock operator.

There are excellent reviews on the numerical integrators in real-time propagation calculations [142, 143]. Here we only give a brief summary of the major methods.

Direct propagation of wavefunctions or density matrices using (58) and (59) requires evaluating the time-ordered exponential of the Fock operator. Generally the Fock operator is time-dependent, which complicates the problem. This time dependence can be handled by dividing the time interval (t, $t+\Delta t$) into small segments and considering the Fock operator fixed within each such segment (short-time approximation). Then the task is to evaluate the exponential of the time-independent Fock operator for short time intervals.

The most straightforward method to calculate the exponential of an operator is to use the Taylor expansion of the exponential function. Practically, a truncation at order four of this expansion works well [143, 144]. Alternatively, one can also choose the Chebychev polynomial to approximate the exponential function [142, 145–147]. The Chebychev polynomial is optimal for approximating functions in the range [−1, 1], but renormalization of the Fock operator is necessary.

Another popular approach to calculate the exponential of an operator is the Krylov subspace method, e.g., the Lanczos iteration method [148–151]. In these methods the operator is projected onto a subspace (Krylov subspace) generated by consecutively applying the operator on the target vector. Any function of the operator can be approximate within this subspace, whose dimension is much smaller than that of the original operator.

The Fock operator consists of the kinetic energy operator, which is diagonal in reciprocal space, and the potential energy operator, which is diagonal in real space. This leads to the split-operator approach to calculate the exponential of the Fock operator. The exponential of the Fock operator can be approximated as the product of exponentials of the kinetic and potential energy operators [152, 153], which can be calculated exactly. There are higher order extensions of this simple split-operator scheme [154].

For time-dependent Fock matrices, integrating (56) numerically is not easy because nonsymplectic integrators such as the common Runge–Kutta methods, are numerically unstable for large scale simulations. One way to avoid such numerical difficulties is by using the Magnus (cumulant) expansion [1, 141, 155, 156]. The Magnus expansion of $\mathbf{U}(t+\Delta t,\ t)$ is

$$\mathbf{U}(t+\Delta t,t)=\hat{T}\exp\left(-\mathrm{i}\int_{t}^{t+\Delta t}\mathbf{F}(\tau)\mathrm{d}\tau\right)=\mathrm{e}^{\boldsymbol{\Omega}_1+\boldsymbol{\Omega}_2+\cdots},\tag{61}$$

and

$$\boldsymbol{\Omega}_1(t+\Delta t,t)=-\mathrm{i}\int_{t}^{t+\Delta t}\mathbf{F}(\tau)\mathrm{d}\tau,\tag{62}$$

$$\boldsymbol{\Omega}_2(t+\Delta t,t)=-\frac{1}{2}\int_{t}^{t+\Delta t}\int_{t}^{\tau_1}[\mathbf{F}(\tau_1),\mathbf{F}(\tau_2)]\mathrm{d}\tau_2\mathrm{d}\tau_1.\tag{63}$$

The higher order $\boldsymbol{\Omega}$ terms can be expressed with nested commutators of $\mathbf{F}$ at different times [155]. If we truncate the exponential expansion at first order in (61) and use the midpoint value $\mathbf{F}(t+\Delta t/2)$ to represent all $\mathbf{F}$ values in the time interval $t,\ t+\Delta t$, we have

$$\mathbf{U}(t+\Delta t,t)=\mathrm{e}^{\boldsymbol{\Omega}_1},\tag{64}$$

$$\boldsymbol{\Omega}_1(t+\Delta t,t)=-\mathrm{i}\mathbf{F}(t+\Delta t/2)\Delta t.\tag{65}$$

Equation (59) then becomes

$$\boldsymbol{\sigma}(t+\Delta t)=\mathrm{e}^{-\mathrm{i}\mathbf{F}(t+\Delta t/2)\Delta t}\boldsymbol{\sigma}(t)\mathrm{e}^{\mathrm{i}\mathbf{F}(t+\Delta t/2)\Delta t}.\tag{66}$$

One problem with using (66) in direct propagation is that $\mathbf{F}(t+\Delta t/2)$ is unknown at time t. $\mathbf{F}(\mathrm{t}+\Delta t/2)$ should be estimated by linearly extrapolating the $\mathbf{F}$ values at previous times, or through some predictor-corrector technique [157]. However, the latter breaks the time evolution symmetry. Alternatively, we can say backward time propagation with the predictor-corrector cannot reproduce the original state of the system at early time. The modified midpoint unitary transform method (MMUT) [158, 159] maintains this time-reversibility. In this method, $\mathbf{U}(t+\Delta t,\ t-\Delta t)$ is constructed from the eigenvectors $\mathbf{C}(\mathbf{t})$ and the eigenvalues $\boldsymbol{\varepsilon}(t)$ of $\mathbf{F}(t)$ at the time midpoint:

$$\mathbf{U}(t+\Delta t,t-\Delta t)=\exp[\mathrm{i}\cdot 2\Delta t\mathbf{F}(t)]=\mathbf{C}(t)\exp[\mathrm{i}\cdot 2\Delta t\boldsymbol{\varepsilon}(t)]\mathbf{C}^{\dagger}(t).\tag{67}$$

The corresponding density matrix time propagation equation is

$$\boldsymbol{\sigma}(t+\Delta t)=\mathbf{U}(t+\Delta t,t-\Delta t)\boldsymbol{\sigma}(t-\Delta t)\mathbf{U}^{\dagger}(t+\Delta t,t-\Delta t).\tag{68}$$

For other popular integrators such as the one combined split-operator with the enforced time-reversal symmetry method, see [143]. Implementations of

RT-TDDFT/TDHF are available in standard quantum chemistry packages such as Gaussian [158, 160], NWChem [156], and Octopus [161].

RT-TDDFT has been used to calculate X-ray linear absorption spectroscopy [100, 162]. The time-dependent perturbed Fock matrix is

$$\mathbf{F}(t) = \mathbf{F}(0) - \mathbf{D} \cdot \mathbf{E}(t), \tag{69}$$

where **D** is the dipole matrix and $\mathbf{E}(t)$ is the time-dependent external electric field. An impulsive external electric field is used in the calculation:

$$\mathbf{E}(t) = \hat{r} \cdot k\delta(t), \tag{70}$$

where $\hat{r} = x, y, z$, k is the perturbation strength, and $\delta(t)$ is the δ function. The density matrix is then propagated under this perturbation and the time-dependent dipole moment is calculated through (57). The molecular polarizability is proportional to the Fourier transform of $\mu(t)$:

$$\alpha_{ij}(\omega) = \frac{\tilde{\mu}_{ij}(\omega)}{k}, \tag{71}$$

where $i, j = x, y, z$. The linear absorption spectrum can be obtained from the imaginary part of the molecular polarizability:

$$S(\omega) = \frac{4\pi\omega}{c} \cdot \mathrm{Im}\frac{\mathrm{Tr}[\boldsymbol{\alpha}(\omega)]}{3}, \tag{72}$$

where c is the speed of light.

An impulsive perturbation can excite electrons over a broad energy range (e.g., 1,000 eV). So real-time methods have advantages if a large energy range is requested and many excited states are involved in the signal. Real-time methods avoid the diagonalization of a large matrix, but the numerical problem switches to sampling the time interval properly in the Fourier transform. Signal post-processing techniques such as window function are often necessary to obtain sharp core excitation peaks [100].

Suppose the vectorial external electric field has multiple frequency components along different coordinate axes:

$$E_i(t) = \sum_{\omega} E_i^{\omega} \mathrm{e}^{-\mathrm{i}\omega t}, \tag{73}$$

where $i = x, y, z$ is the coordinate axis index and the summation runs over negative and positive frequency domains to keep the external electric field real. Expansion of the time-dependent dipole under this external field gives

$$\begin{aligned}\mu_i(t) = \quad & \mu_i^0 + \sum_{\omega} \alpha_{ij}(-\omega;\omega) E_j^{\omega} \mathrm{e}^{-\mathrm{i}\omega t} + \\ & \frac{1}{2}\sum_{\omega_1,\omega_2} \beta_{ijk}(-\omega_s;\omega_1,\omega_2) E_j^{\omega_1} E_k^{\omega_2} \mathrm{e}^{-\mathrm{i}\omega_s t} + \\ & \frac{1}{6}\sum_{\omega_1,\omega_2,\omega_3} \gamma_{ijkl}(-\omega_s;\omega_1,\omega_2,\omega_3) E_j^{\omega_1} E_k^{\omega_2} E_l^{\omega_3} \mathrm{e}^{-\mathrm{i}\omega_s t} + \cdots,\end{aligned} \tag{74}$$

where μ^0 is the permanent dipole; $i, j, k, l = x, y, z$ are coordinate axis indices; and ω_s is the sum of frequencies: for β, $\omega_s = \omega_1 + \omega_2$; and for γ, $\omega_s = \omega_1 + \omega_2 + \omega_3$. In (74), $\alpha_{ij}(-\omega;\ \omega)$ is the linear polarizability in (71); $\beta_{ijk}(-\omega_s;\ \omega_1,\ \omega_2)$ is the first order nonlinear hyperpolarizability, and $\gamma_{ijkl}(-\omega_s;\ \omega_1,\ \omega_2,\ \omega_3)$ is the second-order nonlinear hyperpolarizability. β controls the second-order optical processes such as the electro-optical Pockels effect and second-harmonic generation; whereas γ determines third order optical processes such as the electro-optical Kerr effect, intensity-dependent refractive index, and electric-field-induced second-harmonic and third-harmonic generation. With the full knowledge of these nonlinear dynamical hyperpolarizabilities, in principle one can calculate the nonlinear response of the system under any sequence of laser pulses with different central frequencies and time delays, so that the corresponding nonlinear spectroscopy signals can be simulated. Thus calculating such nonlinear hyperpolarizabilities becomes the major task for quantum chemists in nonlinear spectroscopy simulation studies.

RT-TDDFT has been used to calculate dynamical hyperpolarizabilities. Wang et al. [121] adopted the filter diagonalization method [163–165] to extract components at specific frequencies (e.g., double or triple the input frequency) of the time-dependent dipole moment as a result of solving the EOM of (56). A careful choice of the perturbation field strength was necessary. The strength can neither be too weak nor too strong because a too weak perturbation field results in negligible second and third order response, and a too strong perturbation field makes even higher order response dominant. Moreover, the perturbation should be turned on slowly to avoid nonadiabatic response. They also derived the EOM for the first and second-order response of the density matrix, but evaluating dynamical hyperpolarizabilities using these equations is more costly than using (56). Takimoto et al. [166] used a Gaussian enveloped quasimonochromatic perturbation to approach a δ distribution in the frequency domain in their RT-TDDFT simulation. With this choice, the response equation connecting hyperpolarizabilities and density matrix response at different orders can be easily reverted and dynamical hyperpolarizabilities are determined. Recently, Li and coworkers [167] applied the finite field (numerical differential) method to obtain the time-dependent dipoles at different orders through RT-TDDFT calculations. The components with specific frequencies were extracted by numerical fitting to sinusoidal waves with these frequencies. This scheme avoids Fourier transform which requires a long time simulation.

Two types of time bookkeeping protocols may be used in calculating nonlinear spectroscopy signals. The first is based on the wavefunction. The signals can then be represented by loop diagrams where the ket moves first forward and then backward to account for the bra [168]. The second protocol uses the density matrix and can be represented by ladder diagrams [1]. The first protocol does not maintain the bookkeeping of relative time ordering of bra and ket interactions and results in $n+1$ basic terms for the nth order response. The second protocol fully keeps track of time ordering. Both ket and bra move forward, yielding more 2^n terms [1, 23]. [2] Even though the Casida (or CEO) equations of motion represent the reduced single electron density matrix, this density matrix is simply used for parameterizing the many electron wavefunction given by a single Slater determinant. The response predicted by the equations of motion for the density matrix turns out to correspond to the many-electron wavefunction rather than the density matrix [86, 89].

RT-TDDFT should have many advantages in nonlinear X-ray spectroscopy simulation. Because it does not calculate individual states, it saves computing time when many excited states are involved, which is the case for ultrashort broadband X-ray pulse excitation. Direct propagation of the density matrix, only involves occupied orbitals, so the computational scaling of RT-TDDFT is much better than any SOS method [112], which involves a large number of virtual orbitals. There are already many linear scaling algorithms both in both time [169] and frequency domains [170] for RT-TDDFT in excited state calculations. Both methods rely on the diagonal dominance of single-electron density matrices or transition density matrices. The key issue is to calculate the highly nonlocal exchange components in the popular hybrid density functionals efficiently, which has only recently been addressed [171]. Unlike the perturbation method (to be discussed in the next section), high order functional derivatives are not necessary in RT-TDDFT calculations, so the well-behaved but complicated energy functionals, such as the orbital-dependent functionals or the optimized effective potential (OEP) functionals, can be readily used. In addition, RT-TDDFT has advantages for nonlinear response because the calculations are no more difficult than for linear response, whereas for the frequency domain methods such as SOS, they become increasingly more complex for higher order response. Nuclear motions can also be accounted for by Ehrenfest dynamics [159, 172]. RT-TDDFT offers a direct simulation of nonlinear spectroscopy experiments with short pulses. However, we still have some tradeoffs in using RT-TDDFT. Because individual excited states are not available in RT-TDDFT, it is hard to interpret the spectral features. So far, RT-TDDFT applications have been restricted to calculating standard dynamical hyperpolarizabilities. Simulations of the signals presented in Sect. 2 constitute challenges.

---

[2] Each electronic oscillator which parameterizes the evolution of a single-electron density matrix corresponds to a single electronic excited state appearing in the linear response regime. Nonlinear SOS response calculations are then reformulated as sum-over-oscillator expressions, where multiply excited oscillators appear in the higher order responses leading to 2^n terms. It is interesting that the expressions for the TDHF CEO [89] (or equivalently the Casida TDDFT [86]) response obtained from the equations of motion correspond to the wavefunction, not the density matrix.

3.3 MCSCF Method

The multiconfigurational self-consistent-field (MCSCF) method, particularly of the complete active space SCF (CASSCF) type, has become a practical tool for studying systems with near-degenerate states, e.g., molecules with open-shell character, conical intersections (CoIns), transition metal complexes, and bond breaking molecules (see [173] for a recent review). It describes static correlation in medium-sized molecules well with affordable computational cost, and serves as the basis for more accurate methods which consider the dynamical correlation better, such as MRPT, MRCI, or multireference coupled cluster (MRCC) methods. CASSCF [174–176], which allows full CI expansion in the pre-selected active orbital space, is the most common and successful MCSCF implementation. The concept was introduced in the 1970–1980s by Ruedenberg et al. [177–179] under the name full optimization reaction space (FORS) and it is now known as complete active space, as coined by Roos, Tayler, and Siegbahn [174]. The essential step is the choice of active orbitals. Starting orbitals include localized orbitals [180–183], natural orbitals [184, 185], or pair natural orbitals [186–188], and the corresponding guidance has been reviewed [189, 190]. As a variation to CASSCF, the restricted active space (RASSCF) method [191, 192] decomposes the active space into three subspaces (RAS1, RAS2, RAS3), which allows one to consider more orbitals. Full CI is only allowed in RAS2 while a maximum number of holes and electrons are enforced in RAS1 and RAS3, respectively. Many excellent reviews of the MCSCF method exist (see [173] and references therein), but these mainly focus on the ground and valence excited states. Below we discuss the calculation of core excited states.

3.3.1 Manipulation of the Core Hole

MCSCF core state calculations were first performed in the 1980s by Ågren et al. [193–196], who studied the state-specific low-lying single and double core hole (DCH) states of a series of small molecules, systematically investigated the influence of correlation and relaxation effects on energies, and computed the effective transition dipole moments (TDMs) between separately optimized MCSCF states. The method was rediscovered about 20 years later [197]. In recent years it was employed for work on DCH states and spectra of various small molecules by Tashiro et al. [198–201]. Odelius et al. [202] first employed the state-averaged RASSCF (SA-RASSCF) method [192] in conjunction with the state-interaction treatment of SO effects [203] for L-edge XANES and RIXS spectra of transition-metal-based complexes, and soon calculations were performed for various other similar systems [204–207]. Hua et al. applied it to study the O K-edge ASRS signals of furan conical intersections in the photo-induced ring-opening reaction [208].

Table 1 SCF and MCSCF core hole orbital relaxation energies (eV) for single and double core ionized states of formamide. Singlet energies are used although triplet energies are included in parenthesis if different. Rebuilt based on [196]

Core hole		SCF	MCSCF
Single	$O1s^{-1}$	0.90	0.87
	$N1s^{-1}$	0.88	0.86
	$C1s^{-1}$	0.85	0.83
One-site double	$O1s^{-2}$	−0.28	−0.38
	$N1s^{-2}$	−0.23	−0.35
	$C1s^{-2}$	−0.17	−0.34
Two-site double	$O1s^{-1}N1s^{-1}$	1.79	1.72 (1.73)
	$O1s^{-1}C1s^{-1}$	1.78 (1.76)	1.69
	$N1s^{-1}C1s^{-1}$	1.74	1.68 (1.67)

Core hole calculations require a RAS1 space for the core hole orbital with fixed occupation number. The RAS2 space (and RAS3 space, if necessary) is used for valence correlation. Optimization of the MCSCF wavefunction with core holes must avoid the variational collapse. A rigorous treatment of orbital relaxation can be realized by a two-step procedure [193, 196]. One first freezes the orbital with core hole (RAS1) and relaxes the rest; the frozen core orbital is relaxed in the second step. Different optimization algorithms may be used for the two steps, for example, combining the second-order norm-extended optimization (NEO) algorithm [209, 210] and a straight Newton–Raphson (NR) algorithm. The effect of the second step can be illustrated by the resulting energy change (i.e., the core orbital relaxation energy). Table 1 gives an example for single and double core hole ionization of formamide [196]. The core orbital relaxation energy is a few electronvolts. For a single core hole, it is almost 1 eV; for a one-site double core hole, it is even less; whereas for two-site double core hole, it reaches about 2 eV. This gives an estimate of the effect of freezing the core orbital.

The optimization in step two in practice is more difficult to implement, especially when a state-averaged MCSCF is used, because in this case the object function to optimize is more complicated. It is usually sufficient to skip step two. The underlying physics is that the core orbital is well separated in energy from the valence orbitals, so core orbital relaxation hardly influences the nature of the valence orbitals, but mainly leads to a few electronvolts red shift of transition energies. The calibration can be obtained by aligning the main peak in the calculated XANES spectrum to experiment (this also covers relativistic effects and basis set incompleteness). Because the relaxation energies are similar at the SCF and MCSCF levels (Table 1), one can also estimate the shift value at the simpler SCF level.

3.3.2 Verification of the Active Spaces

A practical way to perform the core hole calculations is to run a valence CASSCF calculation first. One chooses the most important orbitals (e.g., localized or natural orbitals around a breaking bond, 3d orbitals of an excited transition metal) which have flexible occupations in the active space. The converged wavefunction serves as the initial guess for the RASSCF calculation. The original active space is included in the RAS2 space, and the excited core orbital is placed in the RAS1 space. Overall, one extra orbital (the core orbital) and two additional electrons (two core electrons) are added to the active space for core hole calculations to achieve more consistency in valence and core excited states calculations. Including additional virtual orbitals in the RAS3 space can help get a broader energy range for easier comparison with experimental XANES spectra, especially when the ionic potential is relatively high. For example, while studying the metal $L_{2,3}$-edge spectra from the *n*p shell, the RAS2 space should be the 3d orbitals of the metal, and some ligand orbitals can be included in the RAS3 space to represent the ligand-to-metal or metal-to-ligand charge transfer effects [202].

Even though there are general guidelines for choosing the active space [189, 190], it is still necessary to verify by checking the convergence of energy and/or spectra with the active space size. Figure 12 gives an example for the “UV absorption” and “O1s XANES” spectra of a furan CoIn in the photo-induced ring-opening reaction, obtained from a non-adiabatic molecular dynamics trajectory [208]. Such spectra may not be directly observed (because the system is in a superposition of valence states instead of the ground electronic state), but serve as good tests for the active space. They also give an estimate of the accuracy of the calculated transition dipole moments (see next section) which are essential for simulation of the time-domain nonlinear X-ray signals. In Fig. 12a, 10-state-averaged CASSCF was used, and, as expected, a smaller active space expands a broader energy range. Increase of the active space introduces more states with smaller oscillator strengths, and 10 electrons in 10 orbitals (10, 10) is sufficient to obtain essentially converged UV spectra. The optimized valence state wavefunction serves as the initial guess for core hole calculations. In Fig. 12b, 50 states were calculated using SA-RASSCF. Because core states have a higher density of states than valence states, additional states are needed to get an energy range of several to 10 eV for spectral usage. The 10 valence orbitals (RAS2) plus 1 core orbital (RAS1) [labeled as “(12, 1/10/0)”. Twelve electrons include the 10 valence electrons and 2 electrons originally in the O1s orbital; numbers separated by slashes refer to the sizes of RAS1, RAS2, and RAS3] can give converged O1s XANES. Such active space settings are enough to obtain accurate and consistent electronic structure for both the valence and core-excited state manifolds. Note that here the convergence is much faster than the valence level. A test that includes 20 more orbitals in the RAS3 space “(6, 1/4/20)” shows that it can generate more states in the higher-energy region (534–540 eV) and modify the fine structure of spectra.

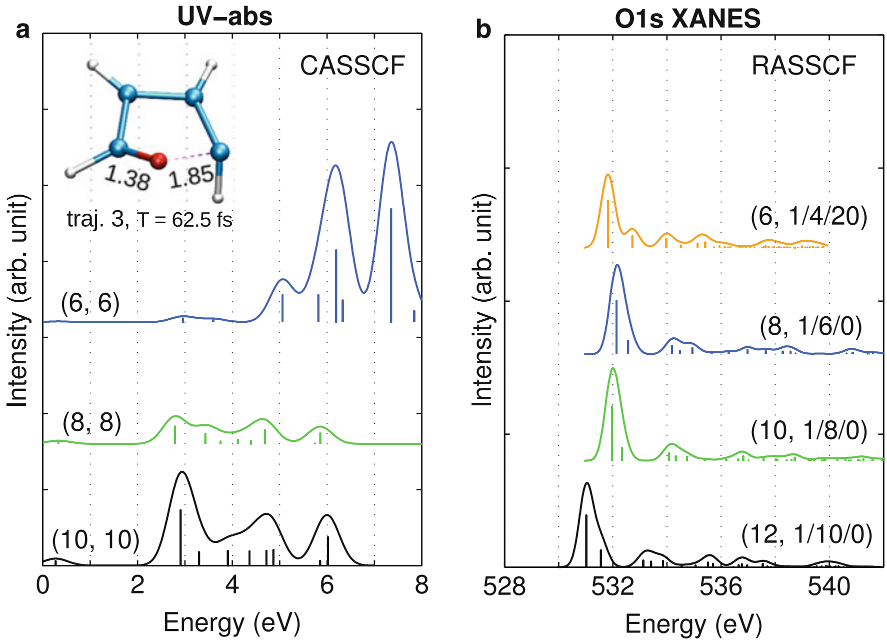

Fig. 12 Simulated (**a**) UV absorption and (**b**) O1s XANES spectra of a furan conical intersection (snapshot at $T = 62.5$ fs in trajectory 3 of the nonadiabatic MD simulation) at different active spaces by using the state-averaged CASSCF or RASSCF method. Active spaces are labeled by (n, m) in panel a or $(n, m_1/m_2/m_3)$ in panel b, where n, m are the number of electrons and orbitals in the active space, and m_1, m_2, and m_3 are the numbers of orbitals in the RAS1, RAS2, RAS3 spaces, respectively. All core hole energies have been uniformly shifted by −3.05 eV. *Inset* in a: geometry of the snapshot with C–O distances labeled in Å. Rebuilt based on [208]

3.3.3 Transition Dipole Moments Between Different Orbital Sets

Application of MCSCF to non-linear X-ray spectroscopy requires the computation of transition dipole moments between the valence, single-core, and double-core manifolds. This is more difficult than valence spectroscopy computations. In the latter case, the ground and the low-lying valence states can be generated in a single state-averaged MCSCF calculation using the same set of optimized orbitals, and the TDMs can be easily obtained by applying the Slater–Condon rule directly. The energies of states differ by one core hole are several tens to hundreds of electronvolts apart, and should be obtained in separate MCSCF calculations. The resulting orbitals are orthogonal within each set but non-orthogonal between different sets. MCSCF is an extension of the TDDFT/TDA or CIS method, so a similar simple solution can be applied. We denote the MCSCF wavefunctions of valence state m and core states e, respectively, as

$$\left|\Phi_m^{\mathrm{MCSCF}}\right\rangle = \sum_j \lambda_j^m \left|\phi_j^m\right\rangle, \tag{75}$$

$$\left|\Theta_e^{\mathrm{MCSCF}}\right\rangle = \sum_i \kappa_i^e \left|\theta_i^e\right\rangle, \tag{76}$$

where $|\phi_j^m\rangle$ and $|\theta_i^e\rangle$ are Slater determinants, and λ_j^m and κ_i^e are the CI coefficients. The corresponding transition dipole matrix is given by

$$\left\langle \Phi_m^{\mathrm{MCSCF}} | \hat{\boldsymbol{\mu}} \, | \Theta_e^{\mathrm{MCSCF}} \right\rangle = \sum_i \sum_j \left(\lambda_j^m\right)^* \kappa_i^e \left\langle \phi_j^m | \hat{\boldsymbol{\mu}} \, | \theta_i^e \right\rangle. \tag{77}$$

Because the MOs of the two manifolds are non-orthogonal, terms of $\left\langle \phi_j^m | \hat{\boldsymbol{\mu}} \, | \theta_i^e \right\rangle$ are calculated using the Löwdin rules [67, 211]. Because this method is based on the determinants, it has a lengthy expansion over configurations. The advantage is that it is easy for programming and parallelization. This algorithm was employed to compute the TDMs between the O1s core excited states and valence excited states of furan [208].

A more efficient approach is the CAS or RAS state interaction (CASSI/RASSI) method based on configuration state functions (CSFs) developed by Malmqvist and Roos [212, 213]. Because a many-electron wavefunction can be equivalently described in different sets of molecular orbitals, the orbitals are rotated (and the coefficients are changed correspondingly) to be biorthonormal. We can then simply use the Slater–Condon rule. Methods for including the spin-orbit (SO) coupling have been developed [203]. This algorithm was employed in early effective TDMs calculations between state-specific valence and core MCSCF states [195] and widely used in recent L-edge XANES and RIXS calculations [202, 204–207].

3.3.4 Example: ASRS Signals as a Probe of Conical Intersections in Furan

We use the furan ring-opening reaction as an example to illustrate the simulation of nonlinear time-domain X-ray signals at the MCSCF level. The ASRS signal provides a sensitive probe of the photo-induced reaction in the vicinity of a CoIn. CASSCF is employed to describe the near-degeneracy introduced by C–O bond-breaking. We first performed a non-adiabatic molecular dynamics simulation by using the trajectory surface hopping (TSH) method [214]; then representative snapshots are chosen for valence and O1s core-excited states calculations by using state-averaged CASSCF and RASSCF, respectively. TDMs were then determined and ASRS signals were calculated. Figure 13 displays the calculated ASRS signals of furan during the passage of a V_1/V_0 CoIn (V_0 and V_1 stand for the ground and lowest valence excited states, respectively) [208]. It is found that as time goes from 27.5 to 33.0 fs, the molecule gradually goes from V_1 to V_0 (Fig. 13b). The

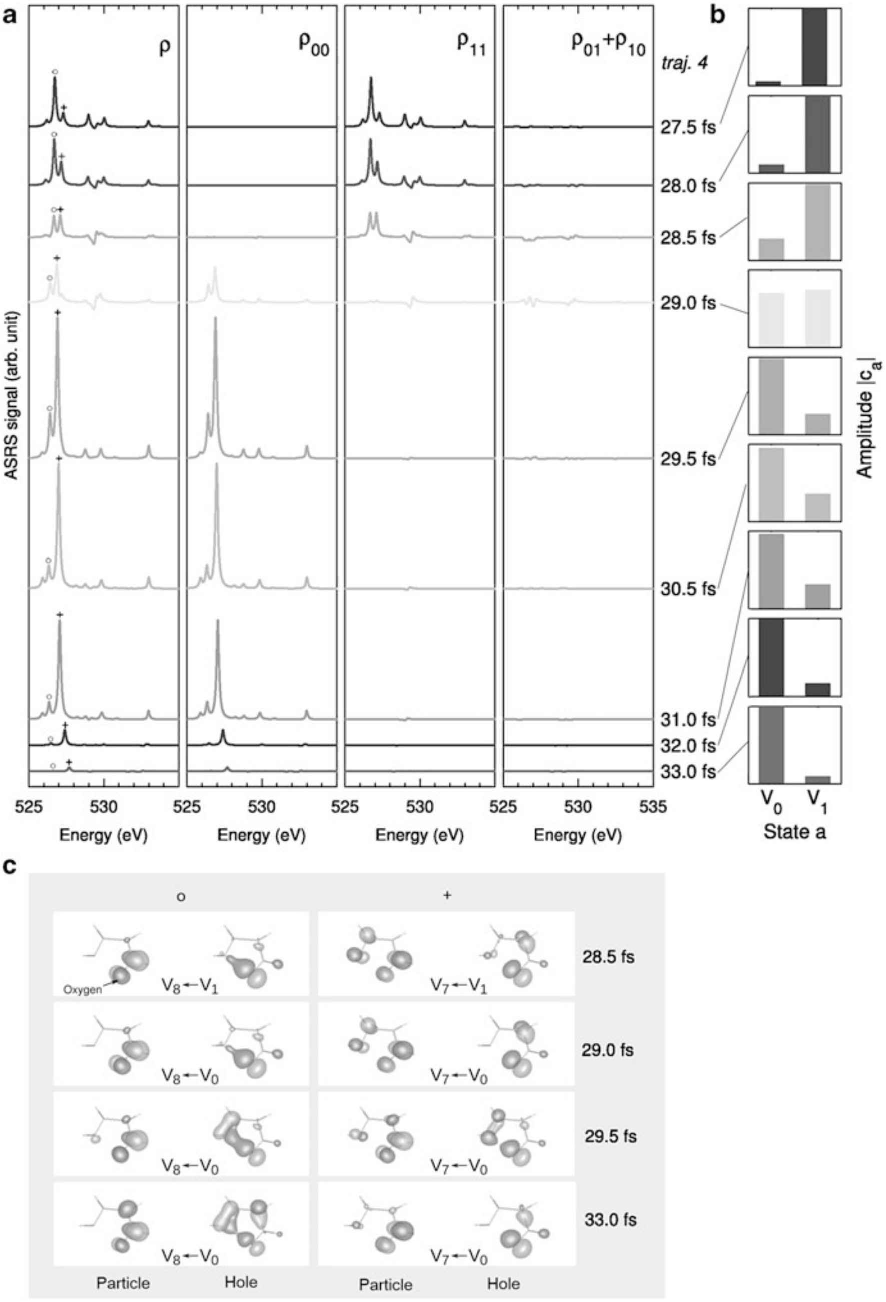

Fig. 13 (**a**) Simulated ASRS signals of for furan during the passage of V_1/V_0 conical intersection ($T = 27.5$–33.0 fs in MD trajectory 4) by using the MCSCF method. From *left to right*, total signals and contributions from ρ_{00} and ρ_{11} populations, and from $\rho_{01} + \rho_{10}$ coherence (0 and 1 refer to states V_0 and V_1). (**b**) Absolute amplitudes of the two constituting states. (**c**) NTOs [215–217] for the two main peaks in the ASRS signals (denoted by "o" and "+"). Dominant hole and particle orbitals are plotted with contour isovalue = 0.08. Rebuilt based on [208]

resulting signals are sensitive to the change in chemical and electronic structure (Fig. 13a, left). Moreover, the contributions from ρ_{00} and ρ_{11} populations and ρ_{01} and ρ_{10} coherences may be separated. Below 29.0 fs the signals mainly come from the V_1 state and after 29.0 fs from the V_0 state. At the transition point $T = 29.0$ fs both V_0 and V_1 populations have comparable contributions to the signals, and coherence terms have larger contributions than at any other time. We had further analyzed two major peaks in the total signals (denoted as "o" and "+", the former is always lower in energy) and found that they can be tracked by varying time-dependent strength: peak "o" is stronger before $T = 29.0$ fs, when peak "+" becomes stronger. Both peaks correspond to transitions from the oxygen p orbital to π^* transitions, as indicated by the dominant natural transition orbital (NTO) [215–217] pairs (Fig. 13c). As time increases, for peak "o" the hole orbital changes from localized on the C–O bond to delocalized. For peak "+", the particle orbital changes from delocalized to localized on the C–O bond.

3.4 Other Core Hole State Simulation Techniques

Unlike most of the practical implementations of DFT, which contain empirical parameters from numerical fitting to experimental data or results from higher level theories, the Green's function method based on many-body perturbation theory provides a systematic way to achieve higher accuracy. Quasiparticle orbital energies can be obtained by solving a set of coupled Hedin equations [218]. These orbital energies offer a much better estimation of the ionization potential and the electron affinity of the system than do Kohn–Sham orbital energies. In Hedin's equations, the one-particle Green's function is solved through a Dyson-like equation with a self-energy, which is complex and energy-dependent. Self-energy plays a similar role as does exchange-correlation energy in DFT. The most popular approximation of self-energy is the GW approximation, where the vertex operator is simplified as product of δ-function and self-energy becomes the product of single-particle Green's function (G) and the dynamically screened Coulomb interaction (W) [218, 219]. Moreover, particle-hole interaction, which is neglected in TDDFT, can be considered and another Dyson-like equation for the four-point polarization function (two-particle Green's function) can be derived [220]. This is the Bethe–Salpeter equation (BSE). GW/BSE equations have to be solved iteratively in a self-consistent way. DFT orbitals and their energies can be used as initial guesses, but the full self-consistent solutions are independent on the initial guesses [221]. BSE can be recast into a form similar to the Casida equation in linear response TDDFT (see (52)), but the kernel in BSE could be frequency-dependent [222–224], which offers a model for designing non-adiabatic exchange-correlation kernel in TDDFT. For a thorough comparison of GW/BSE and TDDFT, see

[219]. The GW/BSE approach has been successfully applied to XANES calculations of solids [225–231]. Until now, GW/BSE is still a theory of heavy solid state flavor. Adapting it to a molecular theory is currently in progress [232–234].

The many-body Green's function techniques with algebraic diagrammatic construction (ADC) [235] was also used to study core excited states [236] and the dynamics of core holes and particles [237, 238]. So far, most applications of the above many-body methods have been made to XANES, and their use to calculate core excited states is limited to small systems because of computational cost. Nonlinear X-ray spectroscopy simulation of large systems is an important future goal.

Other theoretical methods were designed primarily for metal L-edge calculations. These are more challenging than the ligand or metal K-edge calculations because of multiplet effects, spin-orbital coupling, and metal-to-ligand or ligand-to-metal charge transfer. Such transition metal-based systems have attracted broad interest because of the numerous applications in biology (e.g., metallic enzyme centers) and artificial light harvesting (e.g., dye-sensitized solar cells). Because the 2p → 3d transitions are dipole-allowed, the metal $L_{2,3}$-edge spectra can better reflect the valence electron structure of the metal 3d orbitals which are more essential to the chemistry. For metal K-edge spectra, the 1s → 3d transitions are dipole forbidden. These methods have mainly been applied to XANES and RIXS spectra. Nonlinear X-ray spectra require accurate transition dipole moments. To obtain these, both the valence and core-excited states must be treated with consistent accuracy.

Early theoretical efforts on transition metal L-edge X-ray spectra were based on semi-empirical methods developed by de Groot and coworkers [239, 240], namely the crystal field multiplet (CFM) and the charge transfer multiplet (CTM) models. These methods start with the SO-coupled multiplets of the excited metal atom and include the effect of ligands using ligand field theory (LFT). Adjustable parameters include the crystal field splitting and the charge transfer energy. In recent years, there are developments in *ab initio* theory including the *ab initio* CTM based on DFT-CI [241], *ab initio* multiplet ligand-field theory (MLFT) method with Wannier orbitals [242], and method employing the Russel–Saunders coupling [243]. These methods are usually computationally expensive and were employed for relatively small systems with high symmetry. Neese and co-workers [244, 245] proposed an efficient approach by combining DFT and the restricted-open-shell configuration interaction singles (DFT/ROCIS). It introduces global empirical parameters for the periodic table to scale the CI matrix and includes dynamic correlation and the SO coupling effects. Excellent agreement with experiment was obtained for most systems. Besides RASSCF, Odelius et al. [202] further tested the influence of dynamic correlations by using the multiconfigurational second-order perturbation theory (RASPT2) for a $[\mathrm{Ni^{II}(H_2O)_6}]^{2+}$ complex. TDDFT has also been tested for this topic. Although it is widely believed that TDDFT is only valid for transition metal-based systems with closed-shell (e.g., the low spin form of $\mathrm{Fe^{II}}$, $S = O$) but not to those open-shells (e.g., the high spin form of $\mathrm{Fe^{II}}$, $S = 2$), it is still necessary to examine its performance because of its high efficiency. It was found [246] that, for a SCO complex $[Fe^{II}(tren(py)_3)]^{2+}$, the TDDFT approach can predict the Fe L_3-edge XANES spectra of both the low-spin and high-spin complexes which agree well with experiment [247–249]. However, such agreement depends on the system. When the same procedure was applied to a variety of Fe^{II} and Fe^{III} complexes with different spin states, the accuracy did not always persist (Hua et al., submitted).

Other post-HF methods have been employed for simulating the K-edge XES, XAS, or RIXS spectra of very small molecules. The intentions are to examine the effect of electron correlation, to include the effect of shake-up/shake-off processes, and/or to consider the influence of bond breaking. Ågren and coworkers had reported early CI studies of XAS [250, 251] and XES [252, 253] spectra of CO and N_2. Recently, Neese et al. [254] studied the vibrationally-resolved RIXS spectra of CO_2 using the MRCI method. Coupled cluster (CC)-based methods have been developed for core state calculations, including single-reference equation-of-motion CC (EOM-CC) [255, 256], state-specific multireference CC (SS-MRCC) [257], and open-shell symmetry-adapted cluster configuration interaction (SAC-CI) methods [258, 259].

4 Other Computational Issues

4.1 *Density Functionals for Core Excitations*

Core excitation energies are often underestimated by TDDFT. It is often necessary to shift the TDDFT core excitation spectrum by tens of electronvolts for light atom excitations and hundreds of electronvolts for heavy atom core excitations to match experiment. The corresponding shifts for ΔSCF type methods are much smaller, with typical values < 2 eV [57] for light atom core excitations. Both ΔSCF and TDDFT have relativistic and basis set errors. The large differences between their shifts come from the self-interaction error of energy density functionals and the absence of orbital relaxation in TDDFT. A constant (even large) shift to a simulated linear X-ray absorption spectrum does not change the relative positions of spectroscopic features. This may not be the case for nonlinear X-ray spectroscopy spectra because core excitations may interact with each other, and those shifts cannot be considered as constants. Thus a proper choice of energy density functional is essential for a successful TDDFT simulation of nonlinear X-ray spectroscopy signals.

The failure of common generalized gradient approximation (GGA) or hybrid functionals to capture long-range charge transfer excited states was analyzed thoroughly [94], and is attributed to the self-interaction error in the functionals used. Surprisingly, a simple Perdew–Zunger self-interaction correction (SIC) scheme [260] applied to ΔSCF or TDDFT does not correct the core excitation energies in the right direction [261]. This SIC scheme has already been combined with the CPP method (explained in the previous section) to produce improved core excitation energies [262]. Core excitations share many similarities with long-range charge transfer excitations, because the transition orbitals involved in these excitations have negligible overlaps. This suggests that a similar strategy may be used for designing energy functionals for core excitation as is done for long-range charge transfer excitations. The range-separated functionals [263–277] are good choices. In these functionals, the long-range part of the exchange energy is evaluated using Hartree–Fock theory, and in the short-range DFT exchange is used. The $1/r_{12}$ operator is partitioned to two parts:

$$\frac{1}{r_{12}} = \frac{\mathrm{erf}(\mu r_{12})}{r_{12}} + \frac{1 - \mathrm{erf}(\mu r_{12})}{r_{12}}, \tag{78}$$

where erf(r) is the error function and μ is a parameter to control the separation of the long- and short-ranges. We had employed this type of long-range corrected functionals in SXRS simulations [92, 109].

To improve the performance of these long-range corrected functionals, Hartree–Fock exchange should be introduced because core orbitals are very localized. This can be done by adding a Gaussian correction term in the $1/r_{12}$ operator partition scheme:

$$\frac{1}{r_{12}} = \frac{\mathrm{erf}(\mu r_{12})}{r_{12}} - k\frac{2\mu}{\sqrt{\pi}}\mathrm{e}^{-\frac{\mu^2}{a}}r_{12}^2 + \frac{1 - \mathrm{erf}(\mu r_{12})}{r_{12}} + k\frac{2\mu}{\sqrt{\pi}}\mathrm{e}^{-\frac{\mu^2}{a}}r_{12}^2, \tag{79}$$

where k, a are additional parameters for introducing Hartree-Fock exchange in the short-range. The above scheme can be used to obtain the LCgau-core-BOP functional [278]. For light atoms, it can predict their core excitation energies with less than 1 eV errors.

Similarly, Besley and coworkers had proposed the following partition scheme [279]:

$$\begin{aligned}\frac{1}{r_{12}} = & \boxed{C_{\mathrm{SHF}}\frac{1 - \mathrm{erf}(\mu_{\mathrm{SR}} r_{12})}{r_{12}} + C_{\mathrm{LHF}}\frac{1 - \mathrm{erf}(\mu_{\mathrm{LR}} r_{12})}{r_{12}}} - \\ & \boxed{C_{\mathrm{SHF}}\frac{1 - \mathrm{erf}(\mu_{\mathrm{SR}} r_{12})}{r_{12}} + C_{\mathrm{LHF}}\frac{1 - \mathrm{erf}(\mu_{\mathrm{LR}} r_{12})}{r_{12}}} + \frac{1}{r_{12}},\end{aligned} \tag{80}$$

where the C_{SHF} and C_{LHF} parameters control the Hartree–Fock exchange contribution in the long- and short-range. In the above equation the terms in the first box are evaluated with Hartree–Fock exchange and the second with DFT exchange. The resulting SRC1 functional is

$$\begin{aligned} E_{\mathrm{xc}}^{\mathrm{SRC1}} &= \boxed{C_{\mathrm{SHF}}E_{\mathrm{x}}^{\mathrm{SR\text{-}HF}}(\mu_{\mathrm{SR}}) + C_{\mathrm{LHF}}E_{\mathrm{x}}^{\mathrm{LR\text{-}HF}}(\mu_{\mathrm{LR}})} - \\ &\boxed{C_{\mathrm{SHF}}E_{\mathrm{x}}^{\mathrm{SR\text{-}DFT}}(\mu_{\mathrm{SR}}) + C_{\mathrm{LHF}}E_{\mathrm{x}}^{\mathrm{LR\text{-}DFT}}(\mu_{\mathrm{LR}})} + E_{\mathrm{xc}}^{\mathrm{DFT}}. \end{aligned} \tag{81}$$

An alternative form of the short-range corrected functional (SRC2) is

$$\begin{aligned} E_{\mathrm{xc}}^{\mathrm{SRC1}} &= \boxed{C_{\mathrm{SHF}}E_{\mathrm{x}}^{\mathrm{SR\text{-}HF}}(\mu_{\mathrm{SR}}) + C_{\mathrm{LHF}}E_{\mathrm{x}}^{\mathrm{LR\text{-}HF}}(\mu_{\mathrm{LR}})} - \\ &\boxed{(1 - C_{\mathrm{SHF}})E_{\mathrm{x}}^{\mathrm{SR\text{-}DFT}}(\mu_{\mathrm{SR}}) + (1 - C_{\mathrm{LHF}})E_{\mathrm{x}}^{\mathrm{LR\text{-}DFT}}(\mu_{\mathrm{LR}})} + E_{\mathrm{c}}^{\mathrm{DFT}}. \end{aligned} \tag{82}$$

The two functionals coincide when $\mu_{\mathrm{SR}} = \mu_{\mathrm{LR}}$. Both functionals can predict light atom core excitation energies with sub-1 eV accuracy [279].

Instead of partitioning the Coulombic operator in real space, Nakai and coworkers had divided the electron density (orbitals) into the core and valence groups. They proposed to use hybrid functionals with large Hartree–Fock exchange components for core electrons and common hybrid functionals for valence electrons. In the total energy expression, the hybrid scheme varies in the core–core, core–valence, and valence–valence interaction terms. After numerical fitting of the hybrid parameters, the resulting core–valence-(CV) B3LYP functional [280] gives very good core excitation energies for light atoms (error less than 1 eV). In addition, this scheme can be extended to Rydberg states [281]. Despite their success in core excitation calculations, such orbital-specific functionals not only lead to a complicated TDDFT implementation, but also bring some conceptual difficulties such as the lack of a unique Fock operator.

In summary, exchange-correlation functionals specific for core excitations can be designed along the same lines for long-range charge transfer excitations. The key issue is that core excitation functionals cannot be too specific, because, in many nonlinear X-ray spectroscopy experiments, both core and valence excited states are involved and should be treated on the same footing. The core excitation functionals discussed above should be tested in future nonlinear X-ray spectroscopy simulations.

4.2 Expansion of the Polarizability in Electron–Hole Operators

In vibrational Raman spectroscopy the polarizability can be expanded perturbatively in the normal mode operators $\hat{Q}_i$ of the system,

$$\hat{\alpha}_v = \hat{\alpha}_{v0} + \sum_i \frac{\partial \hat{\alpha}_v}{\partial \hat{Q}_i}\hat{Q}_i + \sum_{ij} \frac{\partial^2 \hat{\alpha}_v}{\partial \hat{Q}_i \partial \hat{Q}_j}\hat{Q}_i\hat{Q}_j + \cdots, \tag{83}$$

where

$$\hat{Q}_i = \sqrt{\frac{\hbar}{2m_i\omega_i}}\left(\hat{a}_i^\dagger + \hat{a}_i\right). \tag{84}$$

Here α_{v0} is the polarizability at the equilibrium geometry, and $\hat{a}_i^\dagger$ ($\hat{a}_i$) is the ith phonon creation (annihilation) operator.

In analogy to this, the effective polarizability in electronic X-ray Raman scattering ((18) or (20)) can also be expanded as

$$\hat{\alpha}_p = \alpha_0^{(p)} + \sum_{i,j} K_{ij}^{(p)} \hat{c}_i^\dagger \hat{c}_j + \sum_{i,j,k,l} L_{ijkl}^{(p)} \hat{c}_i^\dagger \hat{c}_j \hat{c}_k^\dagger \hat{c}_l + \cdots, \tag{85}$$

where $\hat{c}_i^\dagger$ ($\hat{c}_i$) is the creation (annihilation) operator for an electron in the ith valence orbital and i, j, k, l are valence orbital indices. The super- and subscript ps indicate the pulse inducing the polarizability and appear on the right hand side as a superscript for typographical convenience. $\hat{\alpha}_0^{(p)}$ is the effective polarizability responsible for Rayleigh scattering. The electron–hole pairs created by $\hat{c}_i^\dagger \hat{c}_j$ play the same role in X-ray Raman scattering as do the vibrational normal modes $\hat{Q}_i$ in optical Raman scattering.

The direct use of the sum-over-state expression of the effective polarizability ((18) or (20)) would require calculation of large number of many-body states and the corresponding state-to-state transition dipoles, which is tedious for large systems. X-Ray Raman signals may be calculated alternatively by solving equations of motion for the reduced, single-electron density matrix in the valence space [87–89, 158]. The polarizability should then be expanded in valence electron creation and annihilation operators (see (85)) avoiding the eigenstate expansion. Core excitations can be included approximately in the calculation of the expansion coefficients, but then the X-ray response is calculated in the valence space. We can view the valence (occupied and unoccupied) orbitals as an open system that exchanges electrons with the core space. This is formally analogous to molecular junctions and the same methods can be applied to the X-ray signals [282–288].

In the following we show how to calculate the expansion coefficients of $\hat{\alpha}_p$, $K_{ij}^{(p)}$ and $L_{ijkls}^{(p)}$, starting with a model Hamiltonian. In solid state applications it is common to construct an electron-boson model Hamiltonian to represent all core and valence excitations [289–293]. Model Hamiltonians can be obtained semi-empirically by numerical fitting to experimental results, or from high level quantum chemistry calculations of model systems. The model Hamiltonian is written in terms of the creation and annihilation operators $\hat{c}_{i(\kappa)}^{(\dagger)}$ for single-particle valence (core) orbitals $\phi_{i(\kappa)}$ (where the anticommutation relations $\left\{\hat{c}_i^\dagger, \hat{c}_j\right\} = \delta_{ij}$ are satisfied). The following model Hamiltonian describes the valence and core orbitals and their interaction:

$$H = \sum_i \varepsilon_i \hat{c}_i^\dagger \hat{c} + \sum_{ijkl} U_{ijkl} \hat{c}_i^\dagger \hat{c}_j^\dagger \hat{c}_k \hat{c}_l + \sum_\kappa \varepsilon_\kappa \hat{c}_\kappa^\dagger \hat{c}_\kappa + \sum_{ij\kappa} U_{ij\kappa} \hat{c}_i^\dagger \hat{c}_j \hat{c}_\kappa \hat{c}_\kappa^\dagger, \tag{86}$$

where ε_i is the energy of the orbital ϕ_i and U_{ijkl} is a nonlinear-interaction matrix element. This could, for example, be the coulomb interaction

$$U_{ijkl} = \int d\mathbf{r} d\mathbf{r}' \phi_i(\mathbf{r}) \phi_j(\mathbf{r}') \frac{1}{\mathbf{r} - \mathbf{r}'} \phi_k(\mathbf{r}') \phi_l(\mathbf{r}). \tag{87}$$

We thus write the Hamiltonian of the valence electrons in the absence of core holes

$$\hat{H}_0 = \sum_i \varepsilon_i \hat{c}_i^\dagger \hat{c}_i + \sum_{ijkl} U_{ijkl} \hat{c}_i^\dagger \hat{c}_j^\dagger \hat{c}_k \hat{c}_l. \tag{88}$$

The transition dipole operator in the core-excitation regime is written

$$\begin{pmatrix} \hat{V} \\ \hat{V}^\dagger \end{pmatrix} = \sum_{i\kappa} \begin{pmatrix} \mu_{i\kappa}^* \hat{c}_\kappa^\dagger \hat{c}_i \\ \mu_{i\kappa} \hat{c}_i^\dagger \hat{c}_\kappa \end{pmatrix}, \tag{89}$$

where κ labels core orbitals. We may now treat the core-valence interaction term in (86) perturbatively to obtain an effective Hamiltonian for the valence electrons in the presence of a single core hole or by recalculating the orbitals of the model in the presence of the core hole potential. In the latter case we must start on the basis of 1-hole orbitals (denoted by ϕ_a, etc.), in which the valence Hamiltonian is

$$\hat{\tilde{H}}_0 = \sum_a \varepsilon_a \hat{c}_a^\dagger \hat{c}_a + \sum_{abcd} U_{abcd} \hat{c}_a^\dagger \hat{c}_b^\dagger \hat{c}_c \hat{c}_d, \tag{90}$$

and then transform to the original orbitals with the overlap matrix **T:**

$$\hat{c}_a^{(\dagger)} = \sum_i t_{ai}^{(*)} \hat{c}_i^{(\dagger)}. \tag{91}$$

This immediately permits us to rewrite $\tilde{H}_0$ on the basis of 0-hole orbitals ϕ_i:

$$\hat{\tilde{\hat{H}}}_0 = \sum_{ij} \tilde{\varepsilon}_{ij} \hat{c}_i^\dagger \hat{c}_j + \sum_{ijkl} \tilde{U}_{ijkl} \hat{c}_i^\dagger \hat{c}_j^\dagger \hat{c}_k \hat{c}_l, \tag{92}$$

where we have defined the auxiliary parameters

$$\tilde{\varepsilon}_{ij} \equiv \sum_a \varepsilon_a t_{ai}^* t_{aj} \quad \tilde{U}_{ijkl} \equiv \sum_{abcd} U_{abcd} t_{ai}^* t_{bj}^* t_{ck} t_{dl}\,. \tag{93}$$

These are the basic relations required to obtain an explicit second-quantized representation for the polarizability $\hat{\alpha}_p$. α has been expanded in creation/annihilation operators in (85). Although one may question the convergence of such a series in general, we can see that higher order terms are proportional to successively higher powers of the pulse duration and it is therefore useful in the limit of ultrashort pulses. To obtain explicit expressions for the coefficients (K_{ij}, etc.) in (85), we expand the exponentials in (25) order by order and adopt a consistent operator ordering. Although the ordering $\hat{c}^\dagger \hat{c} \hat{c}^\dagger \hat{c} \ldots$ is used here, normal ordering with all c to the right is also possible. Because the indices are unrestricted over valence orbitals (both occupied and virtual), there is not much reason to prefer one or the other for low-order expansion and many-electron systems (in particular, this holds because we are interested in a form for $\hat{\alpha}$ which is equally valid for arbitrary valence excited states and not simply polarizability of the ground state). This is important for nonlinear spectroscopies and monitoring of nonequilibrium processes. In expanding the exponentials in (85), various time factors are brought down as multiplicative constants. Integration over these factors with the field envelopes defines a set of auxiliary functions:

$$f_p^{(lmn)}(\Lambda) \equiv \int_{-\infty}^{\infty} d\tau \int_{-\infty}^{\tau} d\tau' \frac{\mathcal{E}_p^*(\tau)\mathcal{E}_p(\tau')}{l!m!n!} \left(\frac{\tau' - \tilde{\tau}_{pi}}{\mathrm{i}}\right)^l \left(\frac{\tau - \tau'}{\mathrm{i}}\right)^m \left(\frac{\tilde{\tau}_{pf} - \tau}{\mathrm{i}}\right)^n, \tag{94}$$

which encode all time dependence and depend on the pulse parameters (collectively denoted as Λ). This auxiliary function enters proportional to terms in (85) which result from lth order expansion in the first propagator, mth order in the second, and nth order in the third. Note that, because of the properties of the pulse and the definition of the $\tilde{\tau}$, the lower limits of integration may be truncated at $\tilde{\tau}_{pi}$ and the upper limit of the $d\tau$ integration may be truncated at $\tilde{\tau}_{pf}$. These auxiliary functions vanish in the limit of $t_p \rightarrow 0$ and, moreover, higher order auxiliary functions (resulting from higher-order terms in the exponential expansion) vanish progressively faster so that the ratio of successive functions also vanishes and the series converges for sufficiently short pulses (pulses shorter than the inverse of any relevant material energy scales). Further insight is gained by considering flat pulses, in which case $f_p^{(lmn)}$ is roughly proportional to a power of the pulse duration $(T_p)^N$ where $N = l + m + n$ (neglecting factors of i and factorials). Because this procedure naturally separates the parametric field dependence from the material operators, we can write the expansion coefficients (K_{ij}, etc.) generically without specifying a pulse envelope. To simplify these expressions, we define $\mu_{ij} \equiv \sum_\kappa \mu^*_{i\kappa}\mu_{j\kappa}$. A straightforward but lengthy calculation then yields the first few terms in (85):

$$\alpha_0^{(p)} = \sum_i \mu_{ii} + f_p^{(010)}(\Lambda)\sum_i \mu_{ii}\tilde{\varepsilon}_{ii}, \tag{95}$$

$$\begin{aligned} K_{ij}^{(p)} = -\mu_{ij} + \left(f_p^{(100)} + f_p^{(001)}\right)\left(\sum_l \mu_{ll}\right)\left(\varepsilon_i\delta_{ij} + \sum_l U_{illj}\right) \\ -f_p^{(010)}\left(\sum_k \left(\mu_{jk}\tilde{\varepsilon}_{ik} + \mu_{ki}\tilde{\varepsilon}_{kj}\right) + \sum_{kl}\mu_{kl}\tilde{U}_{kijl}\right) \end{aligned}, \tag{96}$$

$$L_{ijkl}^{(p)} = -\sum_m \left\{f_p^{(001)}\mu_{ij}U_{kmml} + f_p^{(010)}\left(\mu_{jm}\tilde{U}_{iklm} + \mu_{mk}\tilde{U}_{mijl}\right) + f_p^{(100)}\mu_{lk}U_{immj}\right\}, \tag{97}$$

where, in the first line, we have explicitly notated the dependence on the pulse parameters via the auxiliary function f (omitting this dependence in further expressions for brevity). Note that the above is an expansion up to first order roughly in the product $T_p\varepsilon$ where ε is the material energy scale and higher order expansions generate higher order terms in this quantity which contribute to every coefficient in (85). Because the order of the expansion is determined by the sum $l+m+n$, expanding to second-order adds terms proportional to $f_p^{(101)}$,$f_p^{(110)}$,$f_p^{(011)}$,$f_p^{(200)}$ etc.

4.3 Double Excitations and the X-Ray Double-Quantum-Coherence Signal

Double core excitations or double excitations with a core hole and a valence hole are directly probed by nonlinear X-ray four-wave mixing spectroscopy (e.g., photo echo [48] and double-quantum-coherence [24]) and multidimensional SXRS [108] experiments. Calculating double excitations is of essential importance in nonlinear X-ray spectroscopy simulation. Double core states studied in X-ray two-photon photoelectron spectroscopy can be considered as doubly core excited states of the system with two electrons removed. These double core states are more sensitive to the chemical environment and carry more pronounced electronic many-body effects compared to singly core excited states [201, 294–297]. Strong double excitations (shake-up) features can be found even in linear XANES signals [298].

A doubly excited state can be phenomenologically defined as an excited state with energy close to the sum of two single excitation energies. This definition may be misleading. First, near-degeneracy in energy does not mean the excited states share the same character, and, second, there exists double excitations lower in energy than any single excitation [299]. A proper definition for doubly excited states in quantum chemistry relies on a single Slater determinant reference state. If an excited state can be well described by a multiple Slater determinant expansion based on this reference, and the CI coefficients of the double excitation configurations are dominant, we call it a doubly excited state. According to this definition, different reference states may lead to different double-excitation character [300, 301].

Double excitation remains one of the challenges in DFT and TDDFT [301]. Maitra et al. showed that a frequency-dependent exchange-correlation kernel, which is not available in the common implementation of adiabatic TDDFT, is essential for accessing double excitations [95]. In contrast to early expectations [302], quadratic response theory in adiabatic TDDFT only gives double excitation frequencies as sums of two single excitation frequencies [91, 301, 303]. Adiabatic TDDFT implicitly assumes that the double excited state wave functions are products of single excited state wave functions. This has been shown in [303]. These trivial double excitations behave as harmonic oscillators and result in vanishing double-quantum-coherence signals [24]. Originally dressed TDDFT was proposed to remedy this double excitation issue, but information about the relevant double excitation a priori hinders its practical application. Frequency-dependent exchange-correlation kernels based on the Bethe–Salpeter equation were proposed [224, 304–306], but they have only been tested in simple models or small molecular systems because of complexity. The matrix elements of unknown exchange-correlation kernel can also be extracted from the branching ratio of the experimental $L_{2,3}$-edge X-Ray absorption spectra of 3d transition metals [307]. Spin-flip TDDFT (SF-TDDFT) may access some doubly excited states through a triplet reference state [307–312]. Very recently, the constricted variational DFT (CV-DFT) [313–315] was developed to address double excitations [316]. Implementation and testing of this method is under way. We have also combined the ΔSCF method with REW-TDDFT to calculate doubly core excited state and apply it in X-ray double-quantum-coherence (XDQC) signal simulation [24]. The main difficulty with this approach is the unbalanced treatment of the two core holes: one core hole was obtained with ΔSCF and the other with REW-TDDFT. Althgough the two core holes are not symmetric, different calculation order (either ΔSCF first or REW-TDDFT first) would lead to different simulation results [24]. Other high level *ab initio* methods, such as CASSCF/CASPT2 [317], coupled cluster (CC) [318], MRCI [319, 320], symmetry-adapted cluster configuration interaction (SAC-CI) [321], algebraic diagrammatic construction (ADC) [299, 322, 323], and multireference Møller–Plesset perturbation theory (MRMP) [324, 325], can accurately capture double excitations, but their use is limited to small systems because of high computational cost.

The DQC signal probes doubly excited states and strongly depends on the coupling between single excitations. In the infrared regime, DQC signals detect the couplings between vibrational modes, which determine their anharmonicities [326]. In the optical regime, DQC signals were used to reveal quantitative information about electron–electron interactions, many-body wave functions, and electron correlation in excitons [327]. The X-ray variant of this technique (XDQC) is sensitive to correlation and exciton scattering in doubly core excited states, making it an attractive experimental test for electronic structure theories of strongly

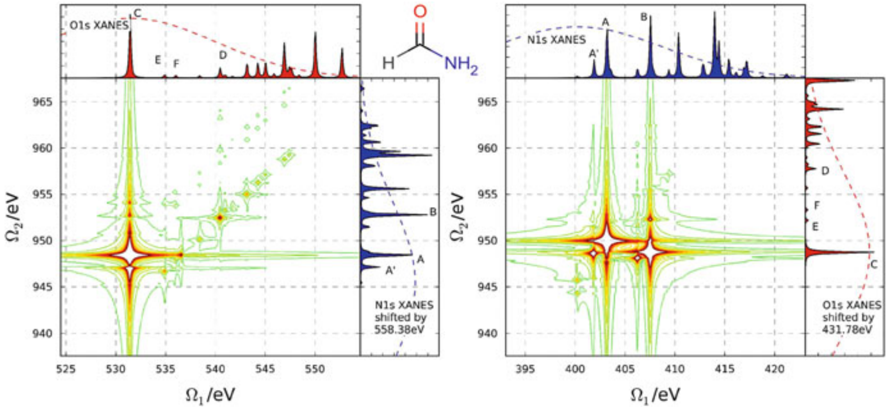

Fig. 14 Comparison of the absolute values of the ONNO (*left*) and NONO (*right*) S_{XDQC} ($t_3 = 5$ fs, Ω_2, Ω_1) signals of formamide (structure shown on the *top*) from calculations combined ΔSCF with REW-TDDFT. XANES spectra are shown in the *marginals*. Figure adapted from [24]

correlated systems [328]. XDQC signals exist only when single core excitations interact with each other and doubly core-excited states are not simply an outer product of two singly core-excited states. XDQC signals vanish for noninteracting single core excitations.

We have simulated the XDQC signals of formamide at the N and O K-edges [24]. In Fig. 14 we show the 2-D projections (we set the last time delay to 5 fs) of the XDQC signals for different pulse orders (ONNO and NONO). The Ω_1 axis represents the N1s or O1s single excitation energies and the Ω_2 axis represents the N and O1s double excitation energies. The intensity of the 2-D XDQC signal at the position (Ω_1, Ω_2) represents the correlation between the single excitation at Ω_1 and the double excitation at Ω_2. The (shifted) XANES spectra are also placed in the marginals to help the signal analysis. In the plot of the ONNO (O excitation first, and then N excitation; see the left column of Fig. 14) signal we can find features scattered along several diagonal straight lines, which indicates almost uniform interaction between the O1s and N1s single excitations, so that the double excitations are almost sums of the single excitations with constant shifts. This can also be confirmed by comparing the energy differences of spectroscopic features in the XANES and XDQC spectra. Take peak A and A′ in the N1s XANES spectrum (right marginal of the ONNO signal) for an example. The energy difference between these two peaks is 1.29 eV in XANES and 1.34 eV in the ONNO spectrum, which are very close to each other. This means the first O1s excitation shifts all N1s excitations in almost the same way, so the energy differences between peaks would not change too much. The same linear pattern is not observed in the NONO signal (the right column of Fig. 14). This tells us the second O1s excitations are affected very differently from each other by the first N1s excitations. From the ONNO signal we can also find that peak B in the N1s XANES only correlates weakly with peak C in the O1s XANES when the O1s electron is excited first, whereas if the N1s electron is excited first, the N1s excitation which corresponds to peak B heavily affects the following O1s excitation which corresponds to peak C (a strong feature connecting peak B and C in the NONO spectrum). By comparing XDQC signals of different pulse orders, we can understand the subtle many-body correlations between core excitations. Generally, X-ray four-wave mixing signals including the XDQC signals can measure double core excited states directly, thus providing new experimental tests for the accuracy of the electronic structure methods and offering a way to visualize projections of the complicated many-electron wave functions [25, 26].

4.4 Ionization, Photoelectron Signals and Resonances

X-Ray photons with energies higher than the ionization threshold can excite the system to a metastable resonance state, and then this resonance decays to a cationic species and a leaving electron. In spectroscopy, either the cationic species or the leaving electron can be detected, both providing us with windows into the electronic structure of the parent neutral system.

In addition to excitation, molecular ionization is another way to trigger impulsively rich electronic and nuclear dynamics such as geometry relaxation, molecular dissociation [329], charge migration [330–334], and radiation emission [335]. Ionization has advantages over excitation in pumping the system because there is no selection rule to restrict which ionization is allowed, and there is usually a lower number of energetically accessible cationic states compared to the large number of high energy exited neutral states in excitation experiments. Moreover, after ionization, we have the freedom to detect the cationic states or the ejected electron, which can provide more information about the parent neutral species. X-Ray ionization and fragmentation have been used to probe transient molecular structures during a photoinduced chemical reaction process [336]. Recently we studied the cationic states of the amino acid glycine prepared by a sudden N1s core ionization produced by an attosecond X-ray pulse [337]. The created superposition of cationic states is probed by 2D transient X-ray absorption (TXAS) and 3D ASRS. Our simulated ASRS results reveal the complex coupling of the valence and core excited states of the cation.

X-Ray photoelectron spectroscopy (XPS) [338] is a powerful technique for probing the chemical compositions and electronic states of molecular systems and materials. By measuring the kinetic energy of the ejected photoelectrons, the electronic energy levels of the ionized species can be determined. The photoelectrons also carry momenta. Additional information about the initial and final electronic wavefunctions can be obtained by measuring photoelectron angular distributions (PAD) [339–341]. TRPES [342, 343] is also used to monitor the electronic structure changes during a chemical reaction.

The total TRPES signal $\mathrm{S}_{\mathrm{TRPES}}\ (E_k, t)$ can be expressed as a sum of the probabilities of transitions from the neutral electronic state I to the cationic electronic state F and free electron state $\eta\left(P_{I\to F\eta}(E_k, t)\right)$:

$$S_{\mathrm{TRPES}}(E_k, t) = \sum_{I, F, \eta(E_k)} P_{I\to F\eta}(t), \tag{98}$$

where E_k is the kinetic energy of the ejected electron, and t is the observation time. For the probability of a single transition, we have

$$P_{I\to F\eta}(t) \propto \left|\boldsymbol{E}_{\mathrm{probe}} \cdot \left\langle \psi_{\mathrm{F}}\psi_{\eta}\right|\hat{\boldsymbol{\mu}}\left|\psi_{\mathrm{I}}\right\rangle\right|^2 \delta(\hbar\omega - E_k(\eta) - \Delta E_{\mathrm{IF}}), \tag{99}$$

where $\boldsymbol{E}_{\mathrm{probe}}$ and ω are the polarization vector and frequency of the probe light field, respectively, ψ_I, ψ_F, and ψ_η are the wavefunction of the neutral state I, the cationic state F, and the free electron state η, respectively, and $\Delta E_{\mathrm{IF}} = E_{\mathrm{F}} - E_{\mathrm{I}}$ is the ionization energy corresponding to the neutral state I and cationic state F. Here we employ the sudden ionization approximation [344, 345], in which the ionization process is very fast and the leaving electron does not interact with the cation, so the final state function can be written as a product of ψ_F and ψ_η. We can also assume that ψ_η is orthogonal with ψ_I, so (99) can be recast as

$$P_{I\to F\eta}(t) \propto \left|\left\langle \psi_{\eta}\right|\boldsymbol{E}_{\mathrm{probe}} \cdot \hat{\boldsymbol{\mu}}\left|\psi_{\mathrm{IF}}^{\mathrm{D}}\right\rangle\right|^2 \delta(\hbar\omega - E_k(\eta) - \Delta E_{\mathrm{IF}}). \tag{100}$$

Here we introduce a one-electron quantity called the Dyson orbital $\psi_{\mathrm{IF}}^{\mathrm{D}}$, defined as the generalized overlap amplitudes between the neutral state I and the cationic state F [345]:

$$\psi_{\mathrm{IF}}^{\mathrm{D}}(\mathbf{r}_N) = \sqrt{N}\int \psi_{\mathrm{F}}^{*}(\mathbf{r}_1, \mathbf{r}_2, \ldots, \mathbf{r}_{N-1})\psi_{\mathrm{I}}(\mathbf{r}_1, \mathbf{r}_2, \ldots, \mathbf{r}_N)\mathrm{d}\mathbf{r}_1\mathrm{d}\mathbf{r}_2\ldots\mathrm{d}\mathbf{r}_{N-1}, \tag{101}$$

where N is the number of electrons in the system. If the polarization of the probe field and the angular distribution of the photoelectron is ignored, (100) can be simplified as [346, 347]

$$P_{I\to F\eta}(t) \propto \left|\psi_{\mathrm{IF}}^{\mathrm{D}}\right|^2 \bar{\mu}_\eta^2 \delta(\hbar\omega - E_k(\eta) - \Delta E_{\mathrm{IF}}), \tag{102}$$

where $\bar{\mu}_\eta$ is an appropriate average value for the transition dipole matrix element between the Dyson orbital $\psi_{\mathrm{IF}}^{\mathrm{D}}$ and free electron state ψ_η. If all free electron states η with a kinetic energy E_k are summed over in (100), we have

$$P_{I\to F}(E_k, t) \propto \left|\psi_{\mathrm{IF}}^{\mathrm{D}}\right|^2 \left[\bar{\mu}_\eta(E_k)\right]^2 \rho(E_k)\delta(\hbar\omega - E_k - \Delta E_{\mathrm{IF}}), \tag{103}$$

where $\bar{\mu}_\eta(E_k)$ represents an average transition dipole matrix element corresponding to a kinetic energy E_k, and $\rho(E_k)$ is the density of the free electron state at the kinetic energy E_k. Photoelectron experiments tell us that usually in the low kinetic energy region, $\left[\bar{\mu}_\eta(E_k)\right]^2\rho(E_k) \approx \text{const.}$ [348], so (103) can be further simplified as

$$P_{I\to F}(E_k,t) \propto \left|\psi_{\mathrm{IF}}^{\mathrm{D}}\right|^2 \delta(\hbar\omega - E_k - \Delta E_{\mathrm{IF}}), \tag{104}$$

and the total photoelectron signal is

$$S_{\mathrm{TRPES}}(E_k,t) = \sum_{I,F} w_{\mathrm{IF}} P_{I\to F}(E_k,t), \tag{105}$$

where w_{IF} is some weighting factor because different $P_{I\to F}(E_k,t)$ has different prefactors in (104). In a simplified treatment we can set all w_{IF}s to be equal [349], or treat them as adjustable parameters [347]. Accurate determination of those weighting factors requires complicated electron-molecule scattering calculations [350], which is beyond the scope of this chapter. Recently, we extended 2D TRPES technique (see (105)) to multidimension by adding more pump pulses before the probe ionization pulse [351]. The TRPES of thioflavin T in its photoisomerization has also been studied with *ab initio* molecular dynamics (AIMD) and TDDFT simulations [349].

The Dyson orbital defined in (101) can be considered as the diagonal element of the one-electron reduced transition density matrix between the neutral and the cationic states. Dyson orbitals are generally not normalized. Their norms reflect the one-electron character of the ionization process. In the simplest case when the neutral and cationic states are well described by Hartree–Fock orbitals and the Koopmans theorem applies, the Dyson orbitals reduce to the canonical Hartree–Fock orbitals and their norms are one. Dyson orbitals are solutions of an effective single-particle equation with ionization energies as their eigenvalues [352–354]. Dyson orbitals are widely used in calculating Compton profiles [355, 356] and electron momentum spectra [357], and interpreting orbital imaging experiments [358–360]. Krylov and coworkers [346] describe an implementation of Dyson orbital calculation at the coupled cluster singles and doubles (CCSD) or EOM-CCSD level of theory.

X-Ray photons often bring the molecule into a superexcited state (excitation above the ionization threshold, or resonance). These resonances are usually short-lived with strong coupling with the continuum leading to the final ionization or dissociation of the system. Generally, resonances can be divided into shape resonance and Feshbach type [361, 362]. Resonances are ubiquitous in radiation damage studies of biomolecules [363], molecular electronic device design [364], attosecond pulse generation [365], and X-ray ionization [13].

Resonances may not be captured by conventional quantum chemistry methods because of their unbound nature and lack of variational principle. To compute these unbound states with finite lifetimes, one must use a non-Hermitian Hamiltonian [366]. One approach for calculating resonance is the complex absorbing potential

(CAP) method [367, 368]. In the method, a complex potential is added to the exterior region of the metastable system to absorb the scattering electron and makes the wave function square-integrable, i.e.,

$$\hat{H}_\eta = \hat{H} - \mathrm{i}\eta W, \tag{106}$$

where $\hat{H}$ is the original molecular Hermitian Hamiltonian, W is a box potential which only exists in the exterior region of the system, and η is the parameter to control the strength of this absorbing potential. Ideally, the complex energy of the resonance can be calculated by letting $\eta \to 0^+$, whereas in practical calculations with finite basis sets, one has to find the optimal η to stabilize the complex energy, i.e., the trajectory calculation [367]. The CAP method was extensively used to calculate resonances [369, 370] and was recently combined with DFT [371]. The major problem of this method is that there are at least two parameters (strength and box size) of the CAP to be determined. In some systems the trajectory calculations cannot give certain results [371].

An alternative for resonance is the complex scaling method [372–375]. Other than adding an arbitrary potential to the original Hamiltonian, one transforms the Hamiltonian with a complex coordinate rotation:

$$\mathbf{r}' \to \mathbf{r}\mathrm{e}^{\mathrm{i}\theta}. \tag{107}$$

Here θ is the rotation angle. As in the CAP method, trajectory calculations are necessary to find an optimal θ value. However, because this is the only parameter to be determined, the degree of uncertainty is greatly reduced compared to the CAP calculations. A DFT combined with the complexed scaling method has been developed for resonances [376–379] and has been used to study Stark ionization of atoms and molecules [380]. The trajectory calculation becomes tedious when the system is large. Moreover, there are still some fundamental questions needs to be answered in extending DFT to resonance. For example, the complex version of the v-representability problem.

Quantum chemistry method development for resonance is still in its infancy. Most applications so far are for resonance energy and lifetime calculations of model or very small atomic and molecular systems. Recently, a non-Hermitian RT-TDDFT study of near and above ionization excitations of small molecules was reported [381]. In this study an absorption boundary condition was used to emulate the continuum. This scheme has a potential to be used in the future for X-ray ionization and photoelectron spectroscopy simulations.

4.5 *Vibronic Coupling*

In the Frank–Condon (FC) region, nuclear motion acts as a bath for electronic transitions. Including this effect introduces high-resolution fine structure to the recorded spectra. Theoretical simulations are usually under the Born–Oppenheimer (BO) and the harmonic oscillator approximations, which are usually good in the FC region. The potential energy surfaces (PESs) of the ground and excited states are well separated. The simplest approach to account for vibronic coupling is the linear coupling model (LCM). It assumes the mode-k PES of excited state has the same curvature as that of the ground state but only shifted by a displacement. This approach is efficient and can be applied to medium and large molecules. It has been well illustrated in various linear and nonlinear X-ray spectroscopy calculations including the XPS, XANES, RIXS, and SXRS spectra (see, e.g., [246, 382–388]). A more rigorous method is to include the Duschinsky rotation and/or the non-Condon effects. For time-domain nonlinear spectroscopy, the nuclear and electronic coordinates are mixed together. The response function can be evaluated via the cumulant expansion [1] till truncated order. The vibrationally resolved SXRS spectra were studied by Hua et al. [387] combining the LCM and cumulant expansion till the second-order. With the inclusion of vibronic coupling, a faster decay in the time domain signals, and new splitting and shoulder structures in the frequency-domain were observed.

5 Conclusions and Perspectives

In this chapter we have surveyed some typical nonlinear X-ray spectroscopy signals and the quantum chemistry methods used for their simulation. Because of their balance in accuracy and computational cost, DFT/TDDFT methods are commonly used in excited state calculations. With the fast development of new exchange-correlation functionals and linear scaling algorithms, these methods provide a most valuable quantum chemistry tool for nonlinear X-ray spectroscopy simulation. DFT/TDDFT often provides an adequate zero order electronic structure at reasonable cost, which paves the way for the application of high level methods. DFT/TDDFT-based semiempirical methods such as density functional tight binding (DFTB) [389–392] or time-dependent density functional tight binding (TDDFTB) [393, 394], and their linear scaling forms [395] have been shown useful in spectroscopy simulations of large systems.

DFT/TDDFT works well in many cases but fails for double excitations, long-range charge transfer excitations, and conical intersections. Much effort has been made to address these difficulties by designing more elaborate functionals and schemes. We believe that rather than putting the burden on the functionals, it makes more sense to use DFT/TDDFT results as fast zero-order inputs to high level wave-function approaches and many-body techniques. The recent developments of *ab initio* [396, 397] and many-body perturbation theory [398–401] follow this route. The density matrix renormalization group (DMRG) method should allow one to calculate core or doubly excited state properties with large active spaces [402]. In addition, high-level methods for handling correlation-driven hole delocalization dynamics are still restricted to small systems [403]. Ehrenfest dynamics simulations for most of the systems, which can include nuclear motion, are still formidably expensive [404]. Highly efficient real-time propagation algorithms for large systems are needed to meet the demands of upcoming nonlinear X-ray spectroscopy measurements.

Acknowledgements This work was supported by the U.S. Department of Energy, Office of Science, Basic Energy Sciences under Award #DE-FG02-04ER15571. Yu Zhang and Weijie Hua acknowledge a postdoctoral fellowship by the Department of Energy grant. We also gratefully acknowledge the support of the National Science Foundation (Grant CHE-1361516), and the National Institutes of Health (Grant GM-59230). Helpful comments from Dr. Sergei Tretiak, Dr. Niri Govind and Prof. Kieron Burke are greatly appreciated.

References

1. Mukamel S (1995) Principles of nonlinear optical spectroscopy. Oxford University Press, New York
2. Zewail AH (2000) J Phys Chem A 104(24):5660
3. Krausz F, Ivanov M (2009) Rev Mod Phys 81(1):163
4. Cho M (2008) Chem Rev 108(4):1331
5. Kim H, Cho M (2013) Chem Rev 113(8):5817
6. Mukamel S, Healion D, Zhang Y, Biggs JD (2013) Annu Rev Phys Chem 64:101
7. Beye M, Schreck S, Sorgenfrei F, Trabant C, Pontius N, Schüßler-Langeheine C, Wurth W, Föhlisch A (2013) Nature 501:191
8. Lutman A, Coffee R, Ding Y, Huang Z, Krzywinski J, Maxwell T, Messerschmidt M, Nuhn HD (2013) Phys Rev Lett 110(13):134801
9. Weninger C, Purvis M, Ryan D, London RA, Bozek JD, Bostedt C, Graf A, Brown G, Rocca JJ, Rohringer N (2013) Phys Rev Lett 111(23):233902
10. Marcus G, Penn G, Zholents A (2014) Phys Rev Lett 113(2):024801
11. Bennett K, Biggs JD, Zhang Y, Dorfman KE, Mukamel S (2014) J Chem Phys 140(20):204311
12. Biggs JD, Bennett K, Zhang Y, Mukamel S (2014) J Phys B At Mol Opt Phys 47(12):124037
13. Carravetta V, Ågren H (2011) In: Barone V (ed) Computational strategies for spectroscopy: from small molecules to nano systems. Wiley, Hoboken, pp 137–205
14. Besley NA, Asmuruf FA (2010) Phys Chem Chem Phys 12:12024
15. Milne C, Penfold T, Chergui M (2014) Coord Chem Rev 277–278:44
16. Salam A (2010) Molecular quantum electrodynamics: long-range intermolecular interactions. Wiley, Hoboken, NJ
17. Dorfman KE, Mukamel S (2012) Phys Rev A 86(1):013810
18. Dorfman KE, Bennett K, Zhang Y, Mukamel S (2013) Phys Rev A 87(5):053826
19. Stöhr J (1992) NEXAFS spectroscopy. Springer, Berlin Heidelberg New York
20. De Groot F, Kotani A (2008) Core level spectroscopy of solids. CRC, Boca Raton
21. Bressler C, Chergui M (2004) Chem Rev 104(4):1781

22. Abramavicius D, Palmieri B, Voronine DV, Sanda F, Mukamel S (2009) Chem Rev 109(6): 2350
23. Mukamel S, Rahav S (2010) In: Berman P, Arimondo E, Lin C (eds) Advances in atomic, molecular, and optical physics, vol 59. Elsevier, Amsterdam, pp 223–263
24. Zhang Y, Healion D, Biggs JD, Mukamel S (2013) J Chem Phys 138(14):144301
25. Mukamel S, Oszwaldowski R, Yang L (2007) J Chem Phys 127(22):221105
26. Li Z, Abramavicius D, Mukamel S (2008) J Am Chem Soc 130(11):3509
27. Weiner AM, Silvestri SD, Ippen EP (1985) J Opt Soc Am B 2(4):654
28. Tanaka S, Mukamel S (2002) Phys Rev Lett 89(4):043001
29. Biggs JD, Zhang Y, Healion D, Mukamel S (2012) J Chem Phys 136(17):174117
30. Dorfman KE, Fingerhut BP, Mukamel S (2013) J Chem Phys 139(12):124113
31. Dorfman KE, Fingerhut BP, Mukamel S (2013) Phys Chem Chem Phys 15(29):12348
32. Fingerhut BP, Dorfman KE, Mukamel S (2014) J Chem Theory Comput 10(3):1172
33. Kossakowski A (1972) Rep Math Phys 3(4):247
34. Lindblad G (1976) Commun Math Phys 48(2):119
35. Ando H, Fingerhut BP, Dorfman KE, Biggs JD, Mukamel S (2014) J Am Chem Soc 136(42): 14801
36. Brixner T, Stiopkin IV, Fleming GR (2004) Opt Lett 29(8):884
37. Scheurer C, Mukamel S (2001) J Chem Phys 115(11):4989
38. Tian P, Keusters D, Suzaki Y, Warren WS (2003) Science 300(5625):1553
39. Turner DL (2007) Encyclopedia of magnetic resonance. Wiley, New York
40. Ernst RR, Bodenhausen G, Wokaun A (1990) Principles of nuclear magnetic resonance in one and two dimensions. Oxford University Press, New York
41. Stolow A, Bragg AE, Neumark DM (2004) Chem Rev 104(4):1719
42. Seel M, Domcke W (1991) J Chem Phys 95(11):7806
43. McFarland B, Farrell J, Miyabe S, Tarantelli F, Aguilar A, Berrah N, Bostedt C, Bozek J, Bucksbaum P, Castagna J, Coffee RN, Cryan JP, Fang L, Feifel R, Gaffney KJ, Glownia JM, Martinez TJ, Mucke M, Murphy B, Natan A, Osipov T, Petrović VS, Schorb S, Schultz T, Spector LS, Swiggers M, Tenney I, Wang S, White JL, White W, Gühr M (2014) Nat Commun 5:4235
44. Bennett K, Kowalewski M, Mukamel S (2014) Faraday Discuss. doi:10.1039/C4FD00178H
45. Hua W, Gao B, Luo Y (2012) Prog Chem 24(06):964
46. Nozières P, De Dominicis CT (1969) Phys Rev 178:1097
47. Schwarz WHE, Buenker RJ (1976) Chem Phys 13:153
48. Schweigert IV, Mukamel S (2007) Phys Rev Lett 99:163001
49. Schweigert IV, Mukamel S (2007) Phys Rev A 76:012504
50. Schweigert IV, Mukamel S (2008) J Chem Phys 128:184307
51. Schweigert IV, Mukamel S (2008) Phys Rev A 78:052509
52. Healion DM, Schweigert IV, Mukamel S (2008) J Phys Chem A 112:11449
53. Slater JC (1972) Adv Quantum Chem 6:1
54. Slater JC, Johnsson KH (1972) Phys Rev B 5:844
55. Stener A, Lisini M, Decleva P (1995) Chem Phys 191:141
56. Triguero L, Pettersson LGM, Ågren H (1998) Phys Rev B 58:8097
57. Brena B, Siegbahn PE, Ågren H (2012) J Am Chem Soc 134(41):17157
58. Hunt WJ, Goddard WA III (1969) Chem Phys Lett 3:414
59. Ågren H, Carravetta V, Vahtras O, Pettersson LGM (1994) Chem Phys Lett 222:75
60. Ågren H, Carravetta V, Vahtras O, Pettersson LGM (1997) Theor Chem Acc 97:14
61. Prendergast D, Galli G (2006) Phys Rev Lett 96:215502
62. Gilbert ATB, Besley NA, Gill PMW (2008) J Phys Chem A 112:13164
63. Sleeman DH (1968) Theor Chim Acta 11(2):135
64. Saunders V, Hillier I (1973) Int J Quantum Chem 7(4):699
65. Guest M, Saunders V (1974) Mol Phys 28(3):819
66. Ågren H, Carravetta V, Pettersson LG, Vahtras O (1996) Phys Rev B 53(23):16074

67. Löwdin PO (1955) Phys Rev 97:1474
68. Healion D, Wang H, Mukamel S (2011) J Chem Phys 134(12):124101
69. Zhang Y, Biggs JD, Healion D, Govind N, Mukamel S (2012) J Chem Phys 137:194306
70. Wiberg KB, Hadad CM, LePage TJ, Breneman CM, Frisch MJ (1992) J Phys Chem 96(2):671
71. Slater JC, Wood JH (1970) Int J Quantum Chem 5(S4):3
72. Ziegler T, Rauk A, Baerends EJ (1977) Theor Chim Acta 43(3):261
73. Levy M, Perdew J (1985) Phys Rev A 32(4):2010
74. Levy M, Nagy Á (1999) Phys Rev Lett 83(21):4361
75. Q-Chem Version 4.2 User's Manual (2014) Q-Chem, Inc.
76. GAMESS Documentation, Input Description, P56, Department of Chemistry, Iowa State University, May 2013 www.msg.ameslab.gov/gamess/GAMESS_Manual/input.pdf, accessed on 3/27/2015
77. Liu J, Zhang Y, Liu W (2014) J Chem Theory Comput 10(6):2436
78. Kowalczyk T, Yost SR, Voorhis TV (2011) J Chem Phys 134(5):054128
79. Hanson-Heine MWD, George MW, Besley NA (2013) J Chem Phys 138(6):064101
80. Gaudoin R, Burke K (2004) Phys Rev Lett 93(17):173001
81. Baruah T, Olguin M, Zope RR (2012) J Chem Phys 137(8):084316
82. Yang K, Peverati R, Truhlar DG, Valero R (2011) J Chem Phys 135(4):044118
83. Gavnholt J, Olsen T, Engelund M (2008) J Schiøtz Phys Rev B 78(7)
84. Thouless DJ (1972) The quantum mechanics of many-body systems. Academic, New York
85. Runge E, Gross EK (1984) Phys Rev Lett 52(12):997
86. Casida ME (1995) In: Chong DP (ed) Recent advances in density functional methods, part I, chap. V. World Scientific, Singapore, pp 155–192
87. Tretiak S, Chernyak V, Mukamel S (1996) Chem Phys Lett 259(1):55
88. Tretiak S, Chernyak V, Mukamel S (1997) J Am Chem Soc 119(47):11408
89. Tretiak S, Mukamel S (2002) Chem Rev 102:3171
90. Berman O, Mukamel S (2003) Phys Rev A 67(4):042503
91. Tretiak S, Chernyak V (2003) J Chem Phys 119(17):8809
92. Biggs JD, Zhang Y, Healion D, Mukamel S (2013) Proc Natl Acad Sci 110(39):15597
93. Zhang Y, Biggs JD, Mukamel S (2014) J Mod Opt 61(7):558
94. Dreuw A, Head-Gordon M (2004) J Am Chem Soc 126(12):4007
95. Maitra NT, Zhang F, Cave RJ, Burke K (2004) J Chem Phys 120:5932
96. Stener M, Fronzoni G, de Simone M (2003) Chem Phys Lett 373:115
97. Besley NA, Noble A (2007) J Phys Chem C 111:3333
98. DeBeer-George S, Petrenko T, Neese F (2008) Inorg Chim Acta 361:965
99. Liang W, Fischer SA, Frisch MJ, Li X (2011) J Chem Theory Comput 7(11):3540
100. Lopata K, Kuiken BEV, Khalil M, Govind N (2012) J Chem Theory Comput 8:3284
101. Schmidt N, Fink R, Hieringer W (2010) J Chem Phys 133:054703
102. Davidson ER (1975) J Comput Phys 17:84
103. ADF2013, SCM, Theoretical chemistry. Vrije Universiteit, Amsterdam, The Netherlands. http://www.scm.com
104. Shao Y, Gan Z, Epifanovsky E, Gilbert AT, Wormit M, Kussmann J, Lange AW, Behn A, Deng J, Feng X et al. (2014) Mol Phys 113(2):184
105. Neese F (2011) Wiley Interdiscip Rev Comput Mol Sci 2(1):73
106. Valiev M, Bylaska E, Govind N, Kowalski K, Straatsma T, van Dam H, Wang D, Nieplocha J, Apra E, Windus T, de Jong W (2010) Comput Phys Commun 181:1477
107. Frisch MJ, Trucks GW, Schlegel HB, Scuseria GE, Robb MA, Cheeseman JR, Scalmani G, Barone V, Mennucci B, Petersson GA, Nakatsuji H, Caricato M, Li X, Hratchian HP, Izmaylov AF, Bloino J, Zheng G, Sonnenberg JL, Hada M, Ehara M, Toyota K, Fukuda R, Hasegawa J, Ishida M, Nakajima T, Honda Y, Kitao O, Nakai H, Vreven T, Montgomery JJA, Peralta JE, Ogliaro F, Bearpark M, Heyd JJ, Brothers E, Kudin KN, Staroverov VN, Kobayashi R, Normand J, Raghavachari K, Rendell A, Burant JC, Iyengar SS, Tomasi J,

Cossi M, Rega N, Millam JM, Klene M, Knox JE, Cross JB, Bakken V, Adamo C, Jaramillo J, Gomperts R, Stratmann RE, Yazyev O, Austin AJ, Cammi R, Pomelli C, Ochterski JW, Martin RL, Morokuma K, Zakrzewski VG, Voth GA, Salvador P, Dannenberg JJ, Dapprich S, Daniels AD, Farkas Ö, Foresman JB, Ortiz JV, Cioslowski J, Fox DJ (2009) Gaussian 09. Gaussian Inc, Wallingford CT
108. Biggs JD, Zhang Y, Healion D, Mukamel S (2013) J Chem Phys 138(14):144303
109. Zhang Y, Biggs JD, Govind N, Mukamel S (2014) J Phys Chem Lett 5:3656
110. Chen LX, Zhang X (2013) J Phys Chem Lett 4(22):4000
111. Andrade X, Botti S, Marques MAL, Rubio A (2007) J Chem Phys 126(18):184106
112. Orr B, Ward J (1971) Mol Phys 20(3):513
113. van Gisbergen SJA, Snijders JG, Baerends EJ (1998) J Chem Phys 109(24):10644
114. Larsen H, Jørgensen P, Olsen J, Helgaker T (2000) J Chem Phys 113(20):8908
115. Iwata JI, Yabana K, Bertsch GF (2001) J Chem Phys 115(19):8773
116. Furche F (2001) J Chem Phys 114(14):5982
117. Hait Heinze H, Della Sala F, Gorling A (2002) J Chem Phys 116(22):9624
118. Salek P, Vahtras O, Helgaker T, Ågren H (2002) J Chem Phys 117(21):9630
119. Ye A, Autschbach J (2006) J Chem Phys 125(23):234101
120. Ye A, Patchkovskii S, Autschbach J (2007) J Chem Phys 127(7):074104
121. Wang F, Yam CY, Chen G (2007) J Chem Phys 126(24):244102
122. Shavitt I, Bartlett RJ (2009) Many-body methods in chemistry and physics: MBPT and coupled-cluster theory. Cambridge University Press, Cambridge
123. Norman P, Bishop DM, Jensen HJA, Oddershede J (2001) J Chem Phys 115(22):10323
124. Norman P, Bishop DM, Jensen HJA, Oddershede J (2005) J Chem Phys 123(19):194103
125. Ekström U, Norman P, Carravetta V, Ågren H (2006) Phys Rev Lett 97(14)
126. Linares M, Stafström S, Rinkevicius Z, Ågren H, Norman P (2011) J Phys Chem B 115(18):5096
127. Norman P, Ruud K (2006) In: Leszczynski J (ed) Challenges and advances in computational chemistry and physics, vol 1. Springer, Dordrecht, pp 1–49
128. Bertrand JB, Wörner HJ, Bandulet HC, Bisson É, Spanner M, Kieffer JC, Villeneuve DM, Corkum PB (2011) Phys Rev Lett 106(2):023001
129. Niikura H, Wörner HJ, Villeneuve DM, Corkum PB (2011) Phys Rev Lett 107(9):093004
130. Wörner HJ, Bertrand JB, Fabre B, Higuet J, Ruf H, Dubrouil A, Patchkovskii S, Spanner M, Mairesse Y, Blanchet V, Mével E, Constant E, Corkum PB, Villeneuve DM (2011) Science 334(6053):208
131. Ranitovic P, Hogle CW, Riviere P, Palacios A, Tong XM, Toshima N, Gonzalez-Castrillo A, Martin L, Martin F, Murnane MM et al (2014) Proc Natl Acad Sci 111(3):912
132. Bergues B, Kübel M, Johnson NG, Fischer B, Camus N, Betsch KJ, Herrwerth O, Senftleben A, Sayler AM, Rathje T et al (2012) Nat Commun 3:813
133. Neppl S, Ernstorfer R, Bothschafter EM, Cavalieri AL, Menzel D, Barth JV, Krausz F, Kienberger R, Feulner P (2012) Phys Rev Lett 109(8):087401
134. Krausz F, Stockman MI (2014) Nat Photonics 8(3):205
135. Mikosch J, Boguslavskiy A, Wilkinson I, Spanner M, Patchkovskii S, Stolow A (2013) Phys Rev Lett 110(2):023004
136. Leone SR, McCurdy CW, Burgdörfer J, Cederbaum LS, Chang Z, Dudovich N, Feist J, Greene CH, Ivanov M, Kienberger R et al (2014) Nat Photonics 8(3):162
137. Frumker E, Kajumba N, Bertrand JB, Wörner HJ, Hebeisen CT, Hockett P, Spanner M, Patchkovskii S, Paulus GG, Villeneuve DM et al (2012) Phys Rev Lett 109(23):233904
138. Ivanov M, Smirnova O (2011) Phys Rev Lett 107(21):213605
139. Shafir D, Soifer H, Bruner BD, Dagan M, Mairesse Y, Patchkovskii S, Ivanov MY, Smirnova O, Dudovich N (2012) Nature 485(7398):343
140. Mairesse Y, Higuet J, Dudovich N, Shafir D, Fabre B, Mével E, Constant E, Patchkovskii S, Walters Z, Ivanov MY et al (2010) Phys Rev Lett 104(21):213601
141. Jakowski J, Morokuma K (2009) J Chem Phys 130(22):224106
142. Kosloff R (1988) J Phys Chem 92(8):2087

143. Castro A, Marques MAL, Rubio A (2004) J Chem Phys 121(8):3425
144. Yabana K, Bertsch G (1996) Phys Rev B 54(7):4484
145. Tal-Ezer H, Kosloff R (1984) J Chem Phys 81(9):3967
146. Chen R, Guo H (1999) Comput Phys Commun 119(1):19
147. Baer R, Gould R (2001) J Chem Phys 114(8):3385
148. Lanczos C (1950) J Res Natl Bur Stand 45:225
149. Park TJ, Light JC (1986) J Chem Phys 85(10):5870
150. Saad Y (2011) Numerical methods for large eigenvalue problems. SIAM, Philadelphia
151. Hochbruck M, Lubich C (1997) SIAM J Numer Anal 34(5):1911
152. Feit M, Fleck J, Steiger A (1982) J Comput Phys 47(3):412
153. Feit MD (1983) J Chem Phys 78(1):301
154. Sugino O, Miyamoto Y (1999) Phys Rev B 59(4):2579
155. Blanes S, Casas F, Oteo J, Ros J (2009) Phys Rep 470(5–6):151
156. Lopata K, Govind N (2011) J Chem Theory Comput 7(5):1344
157. Cheng CL, Evans JS, Van Voorhis T (2006) Phys Rev B 74(15)
158. Li X, Smith SM, Markevitch AN, Romanov DA, Levis RJ, Schlegel HB (2005) Phys Chem Chem Phys 7(2):233
159. Isborn CM, Li X, Tully JC (2007) J Chem Phys 126(13):134307
160. Liang W, Chapman CT, Li X (2011) J Chem Phys 134(18):184102
161. Andrade X, Alberdi-Rodriguez J, Strubbe DA, Oliveira MJT, Nogueira F, Castro A, Muguerza J, Arruabarrena A, Louie SG, Aspuru-Guzik A, Rubio A, Marques MAL (2012) J Phys Condens Matter 24(23):233202
162. Akama T, Imamura Y, Nakai H (2010) Chem Lett 39(4):407
163. Wall MR, Neuhauser D (1995) J Chem Phys 102(20):8011
164. Mandelshtam VA, Taylor HS (1997) J Chem Phys 106(12):5085
165. Pang JW, Dieckmann T, Feigon J, Neuhauser D (1998) J Chem Phys 108(20):8360
166. Takimoto Y, Vila FD, Rehr JJ (2007) J Chem Phys 127(15):154114
167. Ding F, Van Kuiken BE, Eichinger BE, Li X (2013) J Chem Phys 138(6):064104
168. Biggs JD, Voll JA, Mukamel S (2012) Phil Trans R Soc A 370(1972):3709
169. Yam C, Zhang Q, Wang F, Chen G (2012) Chem Soc Rev 41(10):3821
170. Challacombe M (2014) Computation 2(1):1
171. Challacombe M, Bock N (2014) J Chem Phys 140(11):111101
172. Li X, Tully JC, Schlegel HB, Frisch MJ (2005) J Chem Phys 123(8):084106
173. Szalay PG, Müller T, Gidofalvi G, Lischka H, Shepard R (2012) Chem Rev 112:108
174. Roos BO, Taylor PR, Siegbahn PEM (1980) Chem Phys 48:157
175. Siegbahn PEM, Heiberg A, Roos BO, Levy B (1980) Phys Scr 21:323
176. Siegbahn PEM, Almlöf J, Heiberg A, Roos BO (1981) J Chem Phys 74:2384
177. Ruedenberg K, Sundberg KR (1976) In: Calais JL, Goscinski O, Linderberg J, Öhrn Y (eds) Quantum science. Plenum, New York, pp 505–515
178. Ruedenberg K, Schmidt MW, Gilbert MM, Elbert ST (1982) Chem Phys 71:41
179. Ruedenberg K, Schmidt MW, Gilbert MM (1982) Chem Phys 71:51
180. Pipek J, Mezey PG (1989) J Chem Phys 90:4916
181. Boys SF (1960) Rev Mod Phys 32:296
182. Edmiston C, Ruedenberg K (1963) Rev Mod Phys 35:457
183. Aquilante F, Pedersen TB, de Merás AS, Koch H (2006) J Chem Phys 125:174101
184. Pulay P, Hamilton TP (1988) J Chem Phys 88:4926
185. Bofill JM, Pulay P (1989) J Chem Phys 90:3637
186. Kutzelnigg W (1963) Theor Chim Acta 1:327
187. Ahlrichs R, Driessler F (1975) Theor Chim Acta 36:275
188. Taylor PR (1981) J Chem Phys 74:1256
189. Veryazov V, Malmqvist PÅ, Roos BO (2011) Int J Quantum Chem 111:3329
190. Schmidt MW, Gordon MS (1998) Annu Rev Phys Chem 49:233
191. Olsen J, Roos BO, Jørgensen P, Jensen HJA (1988) J Chem Phys 89:2185

192. Malmqvist PÅ, Rendell A, Roos BO (1990) J Phys Chem 94:5477
193. Jensen HJA, Jørgensen P, Ågren H (1987) J Chem Phys 87:451
194. Ågren H, Jensen HJÅ (1987) Chem Phys Lett 137:431
195. Ågren H, Flores-Riveros A, Jensen HJÅ (1989) Phys Scr 40:745
196. Ågren H, Jensen HJÅ (1993) Chem Phys 172:45
197. Rocha AB (2011) J Chem Phys 134:024107
198. Tashiro M, Ehara M, Fukuzawa H, Ueda K, Buth C, Kryzhevoi NV, Cederbaum LS (2010) J Chem Phys 132:184302-1
199. Eland JHD, Tashiro M, Linusson P, Ehara M, Ueda K, Feifel R (2010) Phys Rev Lett 105: 213005
200. Takahashi O, Tashiro M, Ehara M, Yamasaki K, Ueda K (2011) Chem Phys 384:28
201. Tashiro M, Ueda K, Ehara M (2012) Chem Phys Lett 521:45
202. Josefsson I, Kunnus K, Schreck S, Föhlisch A, de Groot F, Wernet P, Odelius M (2012) J Phys Chem Lett 3:3565
203. Malmqvist PA, Roos BO, Schimmelpfennig B (2002) Chem Phys Lett 357:230
204. Wernet P, Kunnus K, Schreck S, Quevedo W, Kurian R, Techert S, de Groot FMF, Odelius M, Föhlisch A (2012) J Phys Chem Lett 3:3448
205. Suljoti E, Garcia-Diez R, Bokarev SI, Lange KM, Schoch R, Dierker B, Dantz M, Yamamoto K, Engel N, Atak K, Kühn O, Bauer M, Rubensson JE, Aziz EF (2013) Angew Chem Int Ed 52:9841
206. Bokarev SI, Dantz M, Suljoti E, Kühn O, Aziz EF (2013) Phys Rev Lett 111:083002
207. Atak K, Bokarev SI, Gotz M, Golnak R, Lange KM, Engel N, Dantz M, Suljoti E, Kühn O, Aziz EF (2013) J Phys Chem B 117:12613
208. Hua W, Oesterling S, Biggs JD, Zhang Y, Ando H, de Vivie-Riedle R, Fingerhut BP, Mukamel S (submitted)
209. Jensen HJÅ, Jørgensen P (1984) J Chem Phys 80(3):1204
210. Jensen HJÅ, Ågren H (1984) Chem Phys Lett 110:140
211. Cook DB (2005) Handbook of computational quantum chemistry. Dover, Mineola, New York
212. Malmqvist PÅ (1986) Int J Quantum Chem 30:479
213. Malmqvist PÅ, Roos BO (1989) Chem Phys Lett 155:189
214. Tully JC (1990) J Chem Phys 93:1061
215. Martin R (2003) J Chem Phys 118:4775
216. Mayer I (2007) Chem Phys Lett 443:420
217. Malmqvist PÅ, Veryazov V (2012) Mol Phys 110:2455
218. Hedin L (1965) Phys Rev 139(3A):A796
219. Onida G, Rubio A (2002) Rev Mod Phys 74(2):601
220. Salpeter E, Bethe H (1951) Phys Rev 84(6):1232
221. Caruso F, Rinke P, Ren X, Scheffler M, Rubio A (2012) Phys Rev B 86(8):081102(R)
222. Myöhanen P, Stan A, Stefanucci G, van Leeuwen R (2008) Europhys Lett 84(6):67001
223. Säkkinen N, Manninen M, van Leeuwen R (2012) New J Phys 14(1):013032
224. Zhang D, Steinmann SN, Yang W (2013) J Chem Phys 139(15):154109
225. Shirley EL (1998) Phys Rev Lett 80:794
226. Soininen JA, Shirley EL (2001) Phys Rev B 54:165112
227. Shirley EL (2004) J Electron Spectrosc Relat Phenom 136(1):77
228. Rehr JJ, Kas JJ, Prange MP, Sorini AP, Takimoto Y, Vila F (2009) C R Phys 10(6):548
229. Olovsson W, Tanaka I, Puschnig P, Ambrosch-Draxl C (2009) J Phys Condens Matter 21 (10):104205
230. Vinson J, Rehr J, Kas J, Shirley E (2011) Phys Rev B 83(11):115106
231. Vinson J, Rehr J (2012) Phys Rev B 86(19):195135
232. Baumeier B, Andrienko D, Ma Y, Rohlfing M (2012) J Chem Theory Comput 8(3):997
233. Baumeier B, Andrienko D, Rohlfing M (2012) J Chem Theory Comput 8(8):2790
234. van Setten MJ, Weigend F, Evers F (2013) J Chem Theory Comput 9(1):232

235. Schirmer J, Trofimov AB, Stelter G (1998) J Chem Phys 109:4734
236. Wenzel J, Wormit M, Dreuw A (2014) J Comput Chem 35(26):1900
237. Kuleff AI, Cederbaum LS (2007) Phys Rev Lett 98:083201
238. Dutoi AD, Cederbaum LS, Wormit M, Starcke JH, Dreuw A (2010) J Chem Phys 132:144302
239. de Groot FMF, Fuggle JC, Thole BT, Sawatzky GA (1990) Phys Rev B 42:5459
240. Stavitski E, de Groot FM (2010) Micron 41:687
241. Ikeno H, Mizoguchi T, Tanaka I (2011) Phys Rev B 83:155107-1
242. Haverkort MW, Zwierzycki M, Andersen OK (2012) Phys Rev B 85:165113
243. Bagus PS, Freund H, Kuhlenbeck H, Ilton ES (2008) Chem Phys Lett 455:331
244. Moemelt M, Maganas D, DeBeer S, Neese F (2013) J Chem Phys 138:204101
245. Maganas D, Roemelt M, Weyhermüller T, Blume R, Hävecker M, Knop-Gericke A, DeBeer S, Schlögl R, Neese F (2014) Phys Chem Chem Phys 16(1):264
246. Hua W, Tian G, Fronzoni G, Li X, Stener M, Luo Y (2013) J Phys Chem A 117:14075
247. Huse N, Kim TK, Jamula L, McCusker JK, de Groot FMF, Schoenlein RW (2010) J Am Chem Soc 132:6809
248. Huse N, Cho H, Hong K, Jamula L, de Groot FMF, Kim TK, McCusker JK, Schoenlein RW (2011) J Phys Chem Lett 2:880
249. Cho H, Strader ML, Hong K, Jamula L, Gullikson EM, Kim TK, de Groot FMF, McCusker JK, Schoenlein RW, Huse N (2012) Faraday Discuss 157:463
250. Arneberg R, Ågren H, Müller J, Manne R (1982) Chem Phys Lett 91:362
251. Ågren H, Arneberg R (1984) Phys Scr 30:55
252. Ågren H, Arneberg R (1983) Phys Scr 28:80
253. Ågren H, Arneberg R, Müller J, Manne R (1984) Chem Phys 83:53
254. Maganas D, Kristiansen P, Duda LC, Knop-Gericke A, DeBeer S, Schlögl R, Neese F (2014) J Phys Chem C 118:20163
255. Nooijen M, Bartlett RJ (1995) J Chem Phys 102(17):6735
256. Besley NA (2012) Chem Phys 542:42
257. Brabec J, Bhaskaran-Nair K, Govind N, Pittner J, Kowalski K (2012) J Chem Phys 137(17):171101
258. Kuramoto K, Ehara M, Nakatsuji H (2005) J Chem Phys 122(1):014304
259. Ohtsuka Y, Nakatsuji H (2006) J Chem Phys 124(5):054110
260. Perdew JP (1981) Phys Rev B 23(10):5048
261. Imamura Y, Nakai H (2006) Int J Quantum Chem 107(1):23
262. Tu G, Rinkevicius Z, Vahtras O, Ågren H, Ekström U, Norman P, Carravetta V (2007) Phys Rev A 76(2):022506
263. Tawada Y, Tsuneda T, Yanagisawa S, Yanai T, Hirao K (2004) J Chem Phys 120(18):8425
264. Yanai T, Tew DP, Handy NC (2004) Chem Phys Lett 393(1–3):51
265. Peach MJG, Cohen AJ, Tozer DJ (2006) Phys Chem Chem Phys 8(39):4543
266. Chai JD, Head-Gordon M (2008) J Chem Phys 128(8):084106
267. Chai JD, Head-Gordon M (2008) Chem Phys Lett 467(1–3):176
268. Rohrdanz MA, Martins KM, Herbert JM (2009) J Chem Phys 130(5):054112
269. Toulouse J, Zhu W, Ángyán JG, Savin A (2010) Phys Rev A 82(3)
270. Irelan RM, Henderson TM, Scuseria GE (2011) J Chem Phys 135(9):094105
271. Song JW, Peng D, Hirao K (2011) J Comput Chem 32(15):3269
272. Hermet J, Cortona P, Adamo C (2012) Chem Phys Lett 519–520:145
273. Refaely-Abramson S, Sharifzadeh S, Govind N, Autschbach J, Neaton JB, Baer R, Kronik L (2012) Phys Rev Lett 109(22)
274. Seth M, Ziegler T (2012) J Chem Theory Comput 8(3):901
275. Modrzejewski M, Chałasński G, Szczęńiak MM (2014) J Chem Theory Comput 10(10):4297
276. Mardirossian N, Head-Gordon M (2014) Phys Chem Chem Phys 16(21):9904
277. Tsuneda T, Hirao K (2014) Wiley Interdiscip Rev Comput Mol Sci 4(4):375
278. Song JW, Watson MA, Nakata A, Hirao K (2008) J Chem Phys 129(18):184113
279. Besley NA, Peach MJG, Tozer DJ (2009) Phys Chem Chem Phys 11(44):10350

280. Nakata A, Imamura Y, Otsuka T, Nakai H (2006) J Chem Phys 124(9):094105
281. Nakata A, Imamura Y, Nakai H (2006) J Chem Phys 125(6):064109
282. Nitzan A, Ratner MA (2003) Science 300(5624):1384
283. Galperin M, Ratner MA, Nitzan A, Troisi A (2008) Science 319(5866):1056
284. Niehaus TA, Chen G (2012) In: Zeng J, Zhang RQ, Treutlein HR (eds) Quantum simulations of materials and biological systems. Springer, Dordrecht, Netherlands, pp 17–32
285. Xie H, Jiang F, Tian H, Zheng X, Kwok Y, Chen S, Yam C, Yan Y, Chen G (2012) J Chem Phys 137(4):044113
286. Zhang Y, Chen S, Chen G (2013) Phys Rev B 87(8):085110
287. Zhang Y, Yam CY, Chen G (2013) J Chem Phys 138(16):164121
288. Kwok Y, Zhang Y, Chen G (2013) Front Phys 9(6):698
289. Lundqvist BI (1967) Phys kondens Materie 6(3):193
290. Langreth D (1970) Phys Rev B 1(2):471
291. Overhauser A (1971) Phys Rev B 3(6):1888
292. Hedin L (1999) J Phys Condens Matter 11(42):R489
293. Mukamel S (2005) Phys Rev B 72(23):235110
294. Santra R, Kryzhevoi NV, Cederbaum LS (2009) Phys Rev Lett 103:013002
295. Ueda K, Takahashi O (2012) J Electron Spectrosc Relat Phenom 185(8–9):301
296. Kryzhevoi NV, Santra R, Cederbaum LS (2011) J Chem Phys 135:084302
297. Salén P, van der Meulen P, Schmidt HT, Thomas RD, Larsson M, Feifel R, Piancastelli MN, Fang L, Murphy B, Osipov T, Berrah N, Kukk E, Ueda K, Bozek JD, Bostedt C, Wada S, Richter R, Feyer V, Prince KC (2012) Phys Rev Lett 108(15):153003
298. Otero E, Kosugi N, Urguhart SG (2009) J Chem Phys 131:114313
299. Starcke JH, Wormit M, Schirmer J, Dreuw A (2006) Chem Phys 329:39
300. Casida M, Ipatov A, Cordova F (2006) In: Marques MA, Ullrich CA, Nogueira F, Rubio A, Burke K, Gross EKU (eds) Time-dependent density functional theory, chap. 16, vol 706, Lecture notes in physics. Spinger, Berlin Heidelberg, pp 243–257
301. Elliott P, Goldson S, Canahui C, Maitra NT (2011) Chem Phys 391:110
302. Gross EKU, Dobson JF, Petersilka M (1996) In: Nalewajski RF (ed) *Density-functional theory II, topics in current chemistry*, vol 181. Spinger, Berlin, pp 81–172
303. Tretiak S, Chernyak V, Mukamel S (1998) Int J Quantum Chem 70:711
304. Casida ME (2005) J Chem Phys 122:054111
305. Romaniello P, Sangalli D, Berger JA, Sottile F, Molinari LG, Reining L, Onida G (2009) J Chem Phys 130:044108
306. Sangalli D, Romaniello P, Onida G, Marini A (2011) J Chem Phys 134:034115
307. Scherz A, Gross EKU, Appel H, Sorg C, Baberschke K, Wende H, Burke K (2005) Phys Rev Lett 95(25):253006
308. Krylov AI (2001) Chem Phys Lett 338:375
309. Krylov AI (2001) Chem Phys Lett 350:522
310. Krylov AI, Sherrill CD (2002) J Chem Phys 116:3194
311. Slipchenko LV, Krylov AI (2002) J Chem Phys 117:3694
312. Shao Y, Head-Gordon M, Krylov AI (2003) J Chem Phys 118:4807
313. Wang F, Ziegler T (2004) J Chem Phys 121:12191
314. Ziegler T, Seth M, Krykunov M, Autschbach J, Wang F (2009) J Chem Phys 130(15):154102
315. Cullen J, Krykunov M, Ziegler T (2011) Chem Phys 391(1):11
316. Ziegler T, Krykunov M, Cullen J (2012) J Chem Phys 136(12):124107
317. Seidu I, Krykunov M, Ziegler T (2013) Mol Phys 112(5–6):661
318. Angeli C, Pastore M (2011) J Chem Phys 134:184302
319. Lehtonen O, Sundholm D, Send R, Johansson MP (2009) J Chem Phys 131:024301
320. Marian CM, Gilka N (2008) J Chem Theory Comput 4:1501
321. Schmidt M, Tavan P (2012) J Chem Phys 136:124309
322. Mikhailov IA, Tafur S, Masunov AE (2008) Phys Rev A 77:012510
323. Starcke JH, Wormit M, Dreuw A (2009) J Chem Phys 131:144311

324. Knippenberg S, Starcke JH, Wormit M, Dreuw A (2010) Mol Phys 108:2801
325. Nakayama K, Nakano H, Hirao K (1998) Int J Quantum Chem 66:157
326. Kurashige Y, Nakano H, Nakao Y, Hirao K (2004) Chem Phys Lett 400:425
327. Zhuang W, Abramavicius D, Mukamel S (2005) Proc Natl Acad Sci 102(21):7443
328. Kim J, Mukamel S, Scholes GD (2009) Acc Chem Res 42(9):1375
329. Fausti D, Tobey RI, Dean N, Kaiser S, Dienst A, Hoffmann MC, Pyon S, Takayama T, Takagi H, Cavalleri A (2011) Science 331:189
330. Schinke R (1993) Photodissociation dynamics: spectroscopy and fragmentation of small polyatomic molecules. Cambridge University Press, Cambridge
331. Weinkauf R, Schanen P, Metsala A, Schlag EW, Bürgle M, Kessler H (1996) J Phys Chem 100(47):18567
332. Cederbaum L, Zobeley J (1999) Chem Phys Lett 307(3–4):205
333. Breidbach J, Cederbaum LS (2005) Phys Rev Lett 94(3):033901
334. Remacle F, Levine RD (2006) Proc Natl Acad Sci U S A 103(18):6793
335. Breidbach J, Cederbaum LS (2007) J Chem Phys 126(3):034101
336. Kuleff AI, Cederbaum LS (2011) Phys Rev Lett 106(5):053001
337. Petrović VS, Siano M, White JL, Berrah N, Bostedt C, Bozek JD, Broege D, Chalfin M, Coffee RN, Cryan J, Fang L, Farrell JP, Frasinski LJ, Glownia JM, Guhr M, Hoener M, Holland DMP, Kim J, Marangos JP, Martinez T, McFarland BK, Minns RS, Miyabe S, Schorb S, Sension RJ, Spector LS, Squibb R, Tao H, Underwood JG, Bucks-baum PH (2012) Phys Rev Lett 108(25):253006
338. Zhang Y, Biggs JD, Hua W, Mukamel S, Dorfman KE (2014) Phys Chem Chem Phys 16: 24323
339. van der Heide P (2012) X-Ray photoelectron spectroscopy. Wiley, Hoboken, NJ
340. Wang K, McKoy V (1995) Annu Rev Phys Chem 46(1):275
341. Reid KL (2003) Annu Rev Phys Chem 54(1):397
342. Sanov A (2014) Annu Rev Phys Chem 65(1):341
343. Wu G, Hockett P, Stolow A (2011) Phys Chem Chem Phys 13(41):18447
344. Suzuki T (2012) Int Rev Phys Chem 31(2):265
345. Pickup B, Goscinski O (1973) Mol Phys 26(4):1013
346. Pickup BT (1977) Chem Phys 19(2):193
347. Melania Oana C, Krylov AI (2007) J Chem Phys 127(23):234106
348. Thompson AL, Martínez TJ (2011) Faraday Discuss 150:293
349. Rabalais JW (1977) Principles of ultraviolet photoelectron spectroscopy. Wiley, New York
350. Ren H, Fingerhut BP, Mukamel S (2013) J Phys Chem A 117(29):6096
351. Lucchese R, Raseev G, McKoy V (1982) Phys Rev A 25(5):2572
352. Rahav S, Mukamel S (2010) Phys Rev A 81(6):063810
353. Cederbaum LS, Domcke W (1977) Adv Chem Phys 36:205
354. Ortiz J (1999) Adv Quantum Chem 35:33
355. Linderberg J, Öhrn Y (2004) Propagators in quantum chemistry, 2nd edn. Wiley, Hoboken
356. Kaplan I, Barbiellini B, Bansil A (2003) Phys Rev B 68(23):235104
357. Barbiellini B, Bansil A (2004) J Phys Chem Solids 65(12):2031
358. Miao YR, Ning CG, Liu K, Deng JK (2011) J Chem Phys 134(20):204304
359. Murray R, Spanner M, Patchkovskii S, Ivanov MY (2011) Phys Rev Lett 106(17):173001
360. Saliéres P, Maquet A, Haessler S, Caillat J, Taïeb R (2012) Rep Prog Phys 75(6):062401
361. Mignolet B, Kus T, Remacle F (2013) In: Grill L, Joachim C (eds) Imaging and manipulating molecular orbitals. Springer, Berlin, pp 41–54
362. Schulz G (1973) Rev Mod Phys 45(3):378
363. Simons J (1984) In: Truhlar DG (ed) Resonances in electron-molecule scattering van der Waals complexes, and reactive chemical dynamics. American Chemical Society, Washington, DC, pp 3–16
364. Sanche L (2009) Nature 461(7262):358
365. Goyer F, Ernzerhof M, Zhuang M (2007) J Chem Phys 126(14):144104

366. Strelkov V (2010) Phys Rev Lett 104(12):123901
367. Moiseyev N (2011) Non-Hermitian quantum mechanics. Cambridge University Press, Cambridge
368. Riss U, Meyer HD (1993) J Phys B At Mol Opt Phys 26(23):4503
369. Muga JG, Palao J, Navarro B, Egusquiza I (2004) Phys Rep 395(6):357
370. Santra R, Cederbaum LS (2002) Phys Rep 368(1):1
371. Santra R, Cederbaum LS (2002) J Chem Phys 117(12):5511
372. Zhou Y, Ernzerhof M (2012) J Phys Chem Lett 3(14):1916
373. Aguilar J, Combes JM (1971) Commun Math Phys 22(4):269
374. Balslev E, Combes JM (1971) Commun Math Phys 22(4):280
375. Simon B (1979) Phys Lett A 71(2):211
376. Moiseyev N (1998) Phys Rep 302(5):212
377. Wasserman A, Moiseyev N (2007) Phys Rev Lett 98(9):093003
378. Whitenack DL, Wasserman A (2009) J Phys Chem Lett 1(1):407
379. Whitenack DL, Wasserman A (2011) Phys Rev Lett 107(16):163002
380. Whitenack DL, Wasserman A (2012) J Chem Phys 136(16):164106
381. Larsen AH, De Giovannini U, Whitenack DL, Wasserman A, Rubio A (2013) J Phys Chem Lett 4(16):2734
382. Lopata K, Govind N (2013) J Chem Theory Comput 9(11):4939
383. Hergenhahn U (2004) J Phys B At Mol Opt Phys 37:R89
384. Minkov I, Gel'Mukhanov F, Friedlein R, Osikowicz W, Suess C, Öhrwall G, Sorensen SL, Braun S, Murdey R, Salaneck WR, Ågren H (2004) J Chem Phys 121:5733
385. Minkov I, Gel'mukhanov F, Ågren H, Friedlein R, Suess C, Salaneck WR (2005) J Phys Chem A 109:1330
386. Svensson S (2005) J Phys B At Mol Opt Phys 38:S821
387. Gel'mukhanov F, Ågen H (1999) Phys Rep 312:87
388. Hua W, Biggs JD, Zhang Y, Healion D, Ren H, Mukamel S (2013) J Chem Theory Comput 9:5479
389. Fronzoni G, Baseggio O, Stener M, Hua W, Tian G, Luo Y, Apicella B, Alfé M, de Simone M, Kivimäki A, Coreno M (2014) J Chem Phys 141:044313
390. Porezag D, Frauenheim T, Köhler T, Seifert G, Kaschner R (1995) Phys Rev B 51(19):12947
391. Seifert G, Porezag D, Frauenheim T (1996) Int J Quantum Chem 58(2):185
392. Elstner M, Porezag D, Jungnickel G, Elsner J, Haugk M, Frauenheim T, Suhai S, Seifert G (1998) Phys Rev B 58(11):7260
393. Zheng G, Lundberg M, Jakowski J, Vreven T, Frisch MJ, Morokuma K (2009) Int J Quantum Chem 109(9):1841
394. Niehaus T, Suhai S, Della Sala F, Lugli P, Elstner M, Seifert G, Frauenheim T (2001) Phys Rev B 63(8):085108
395. Trani F, Scalmani G, Zheng G, Carnimeo I, Frisch MJ, Barone V (2011) J Chem Theory Comput 7(10):3304
396. Wang F, Yam C, Chen G, Wang X, Fan K, Niehaus T, Frauenheim T (2007) Phys Rev B 76 (4):045114
397. Thom AJ, Head-Gordon M (2009) J Chem Phys 131(12):124113
398. Sundstrom EJ, Head-Gordon M (2014) J Chem Phys 140(11):114103
399. van Aggelen H, Yang Y, Yang W (2013) Phys Rev A 88(3):030501
400. Yang Y, van Aggelen H, Steinmann SN, Peng D, Yang W (2013) J Chem Phys 139 (17):174110
401. Peng D, Steinmann SN, van Aggelen H, Yang W (2013) J Chem Phys 139(10):104112
402. Scuseria GE, Henderson TM, Bulik IW (2013) J Chem Phys 139(10):104113
403. Chan GKL, Sharma S (2011) Annu Rev Phys Chem 62(1):465
404. Kuleff AI, Cederbaum LS (2014) J Phys B At Mol Opt Phys 47(12):124002
405. Ding F, Chapman CT, Liang W, Li X (2012) J Chem Phys 137(22):22A512